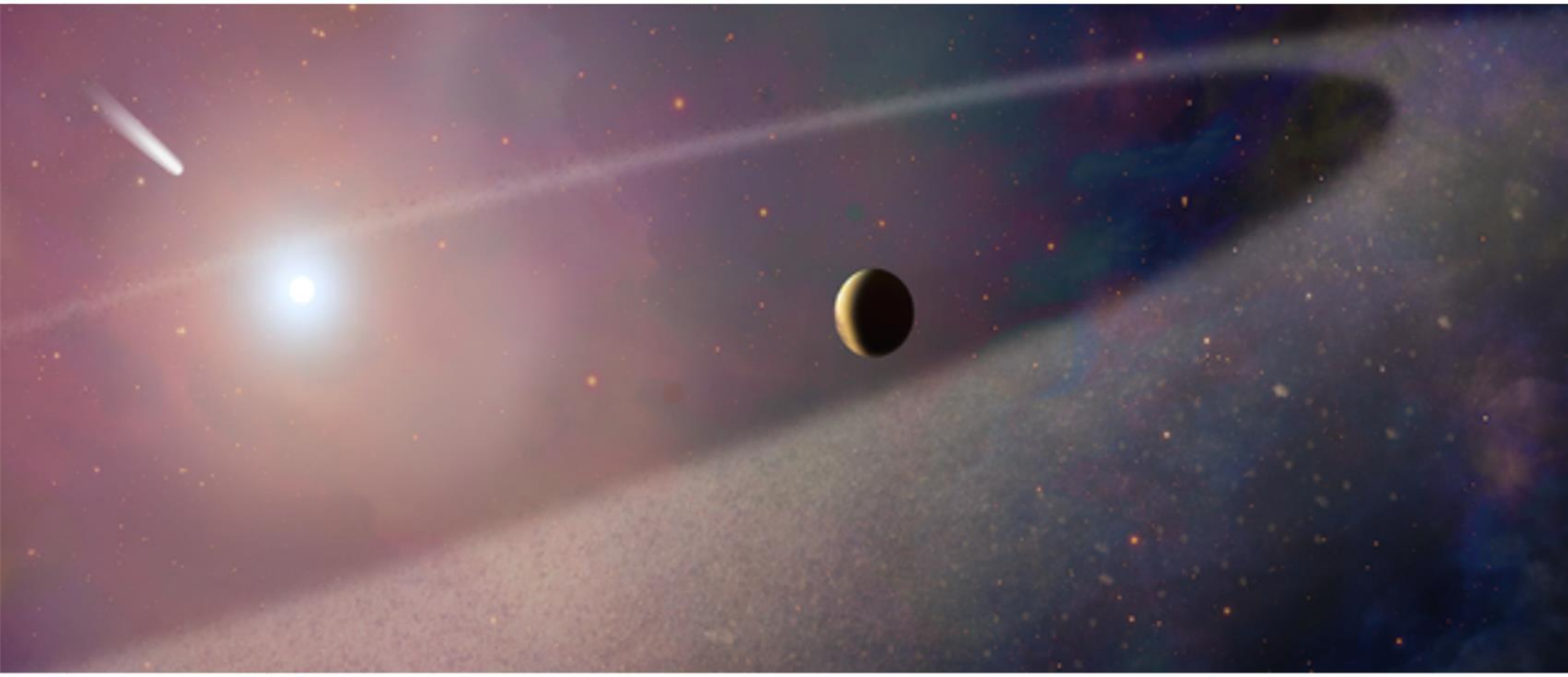

# White Dwarf Pollution

## A STUDY OF ABUNDANCES IN THE CIRCUMSTELLAR MEDIUM

Alice Isabel Lopes Pais de Castro

Master in Astrophysics and Space Instrumentation
September, 2017

· U C ·

COVER SOURCE: https://media.stsci.edu/uploads/story/display_image/1169/low_STSCI-H-p1709a-k1340x520.png


# White Dwarf Pollution

## a study of abundances in the circumstellar medium

Master Thesis in Astrophysics and Space Instrumentation

Alice I. L. Pais de Castro

Supervisors

Dr. Cristina Oliveira – Space Telescope Science Institute

Dr. João Fernandes – University of Coimbra

September 2017

À minha Mãe, ao meu Pai e à minha Margarida

## Agradecimentos

Primeiro de tudo, gostava especialmente de agradecer à minha orientadora, Doutora Cristina Oliveira, pelo seu incansável apoio e dedicação, pelas horas de discussão e questões incessantes e pela graciosa paciência com que sempre me ouviu e respondeu, sem a qual este trabalho não teria visto a luz do dia. Foi um privilégio poder trabalhar e aprender tanto com uma profissional e um ser humano tão sábio e generoso.

Gostava também de agradecer ao Professor João Fernandes, pela sua contante disponibilidade e atenção em responder a todas as minhas questões.

Não me esqueço ainda de todos os colegas e Professores que encontrei e com os quais fiz este percurso universitário, que sem duvida tornaram esta experiencia mais enriquecedora e me trouxeram até aqui. E de todos os amigos, cujas palavras de apoio e conforto, me fizeram rir e tornam esta jornada menos sofrível.

E finalmente, à minha família, à minha Mãe, ao meu Pai e à minha Irmã, o triunvirato pilar da minha vida e a minha maior força de motivação. Estou profundamente grata pelo apoio incessante, que verdadeiramente me permitiu viver como eremita durante a elaboração desta tese, pelos momentos de descontração, pelos sorrisos e palavras encorajamento. É uma bênção e uma honra ter-vos na minha vida.

# Abstract

In this thesis, our main goal was to study the spectrum of polluted white dwarfs, which have present in their photosphere metals in unexpected abundances. Accretion from planetary remnants and asteroids has been proposed as a mechanism to pollute these white dwarfs with metals. For this purpose, 4 DA white dwarfs were selected as targets (WD 0455-282, WD 1611-084, WD 0232+035 and WD2111+498) that showed potentially interstellar (ISM) and circumstellar features, and their spectrum analyzed in the FUV (far ultraviolet) spectral region using data obtain from Far Ultraviolet Spectroscopic Explorer (FUSE) and the Space Telescope Imaging Spectrograph (STIS), onboard the Hubble Space Telescope. Using the apparent optical depth technique we determined column densities for all interstellar species identified in the 4 white dwarfs and evaluated saturation by comparing column densities derived from transitions of different strengths. Nevertheless, in some cases it was impossible to obtain definite values because the lines were either saturated or blended, choosing instead to declare a lower limit. Also, by carefully examining the STIS spectra of WD2111+498 we detected flux variations in certain spectral regions, taking place on the timescale of a few days, that had not previously been identified. We compared our results with the available literature and discussed the results accordingly.

# Resumo

Nesta tese, o nosso principal objetivo era estudar o espectro de anãs brancas poluídas, ou seja, que têm presente na sua fotosfera metais em abundancias inesperadas. Acreção de vestígios planetários e asteroides foi proposto como um mecanismo responsável pela poluição destas anãs brancas com metais. Com este fim em vista, 4 anãs brancas foram selecionadas como alvos (WD 0455-282, WD 1611-084, WD 0232+035 e WD 2111+498) que mostravam a possibilidade de terem a presença de atributos do meio interestelar (ISM) e circumestelar, tendo sido os seus espectros analisados na região FUV (far ultraviolet) usando dados obtidos do Far Ultraviolet Spectroscopic Explorer (FUSE) e do Space Telescope Imaging Spectrograph (STIS), abordo do Hubble Space Telescope. Usando a técnica da aparente profundidade ótica determinamos densidades de colunas para todas as espécies interestelares identificadas nas 4 anãs brancas e avaliamos saturação através da comparação de densidades de coluna derivadas de transições com diferentes forças. No entanto, em alguns casos foi impossível obter valores definitivos porque as linhas de absorção estavam saturadas ou misturadas, escolhendo em vez disso declarar um limite inferior. Além disso, através da observação cuidadosa do espectro STIS do alvo WD 2111+498, detetamos uma variação no fluxo da estrela em certas regiões espectrais, que acontecem numa escala de tempo de apenas alguns dias, cuja existência não tinha sido previamente identificada. Comparamos assim os nossos resultados com a literatura e discutimo-los apropriadamente.

# Table of Contents

# Chapter 1: White Dwarf Pollution

The study of exoplanets is an area of astrophysics that has been evolving at a very fast pace over the last few years and has attracted a lot of interest not only from the scientific community but also from the public in general. Current methods of study of exoplanets such as direct imaging and transit observations allow us to detect the presence of extrasolar planets, under certain conditions, and obtain information about them, such as their dimensions and atmospheric abundances. All of this work has made real the concept of solar systems different from our own, which was not thought to be possible. Consequently, all these new data push us to question about the origin of our own solar system and its peculiar formation conditions.

On the other hand, there has been a relatively new area of exoplanet and solar system study, that aims to understand the "contents" of the extrasolar planets (planetesimal chemistry) by studying the debris disks of white dwarf stars and answer questions such as: what is the composition of exoplanets and planetesimals?, is it familiar or exotic?, and do they experience differentiation like Solar System planets?

This type of research has been made possible by the realization that many dwarfs are metal polluted, and that pollution cannot be explained by current white dwarf models unless there is a continuous source of material that is accreting, particularly for cool white dwarfs ($T_{eff} < 25{,}000$ K). Circumstellar material has also been detected in the spectra of many white dwarfs. One of the possible explanations is that this material comes from debris disks which are the remnants of planetary systems and this has opened a new exciting possibility to learn more about these planetary systems by studying white dwarfs. In other words, these debris disks are thought to be the remnants of former planets, destroyed during the expansion phases of the parent star, and asteroids of the former solar system. This research has also the advantage of allowing us a window into the future of our own solar system and an opportunity to study what might happen after our Sun has reached its white dwarf stage as well.

What this chapter aims to do is, first, introduce stellar formation and evolution of sun like stars to properly explain how white dwarfs come to be and why there are different types. Secondly, an introduction will be made on the topics relevant to understanding this research: white dwarf pollution, different debris disk models that hint different origins for its matter, timeframe issues between disk formation vs white dwarf cooling timescales, the dynamics of white dwarf pollution and other topics.

## 1.1. Stellar evolution

### 1.1.1. What is a star, what sustains it and the stellar classification system

A star is defined as a stellar/astronomical body that radiates due to an internal energy source, usually nuclear energy generated by chain fusion reactions in its core, and possesses gravity to the extent that it demonstrates spherical symmetry (or spheroidal if rotation effects or the star's magnetic field exert extra asymmetrical forces). [15]

However, the most crucial characteristic when studying a star is its mass, since the mass is what will, in turn, define properties of the star. In fact, in the universe there have been found stars as massive as 150 times the mass of our Sun (150 $M_\odot$) or as small as 75 Jupiter planets combined. The limits to a star's size seem to be due to two reasons: ability to remain stable and ability to develop nuclear fusion. When these properties cease to exist, a star will then begin its demise. Moreover, there are two ways a star may end resulting from changes in both composition and structure: either a star stops being stable and breaks apart, which results in the scattering of its matter; or the fuel necessary to power its internal nuclear core ends and the star gradually cools off and eventually becomes extinct, no longer radiating any energy and invisible to any observer – a dead star. In most cases, nonetheless, stars reach the final stage in their evolution in a combination of these two ways. [15]

To study stars, astronomers can infer a star's characteristics by analyzing 2 observable properties: luminosity ($L$) and effective temperature ($T_{eff}$). The correlation between these led to the creation of a diagram that plots a star's spectral type or surface temperature versus its luminosity, the Hertzsprung–Russell diagram (or for short H-R diagram). This was the first time an attempt at testing stellar evolution was made and the results of such graphic, regardless of the sample chosen, conclude that there are fixed combinations of values of $L$ and $T_{eff}$ allowed and 3 general categories of stars: the "main sequence stars", to which belong most of the observed stars (approximately 90%) and our Sun, the "giant stars" composed by giant and super giant stars, which can be as large as 10 times our Sun to having the radius of our Solar System, and finally the "white dwarf stars", the spectral class of the smaller and colder stars. [15]

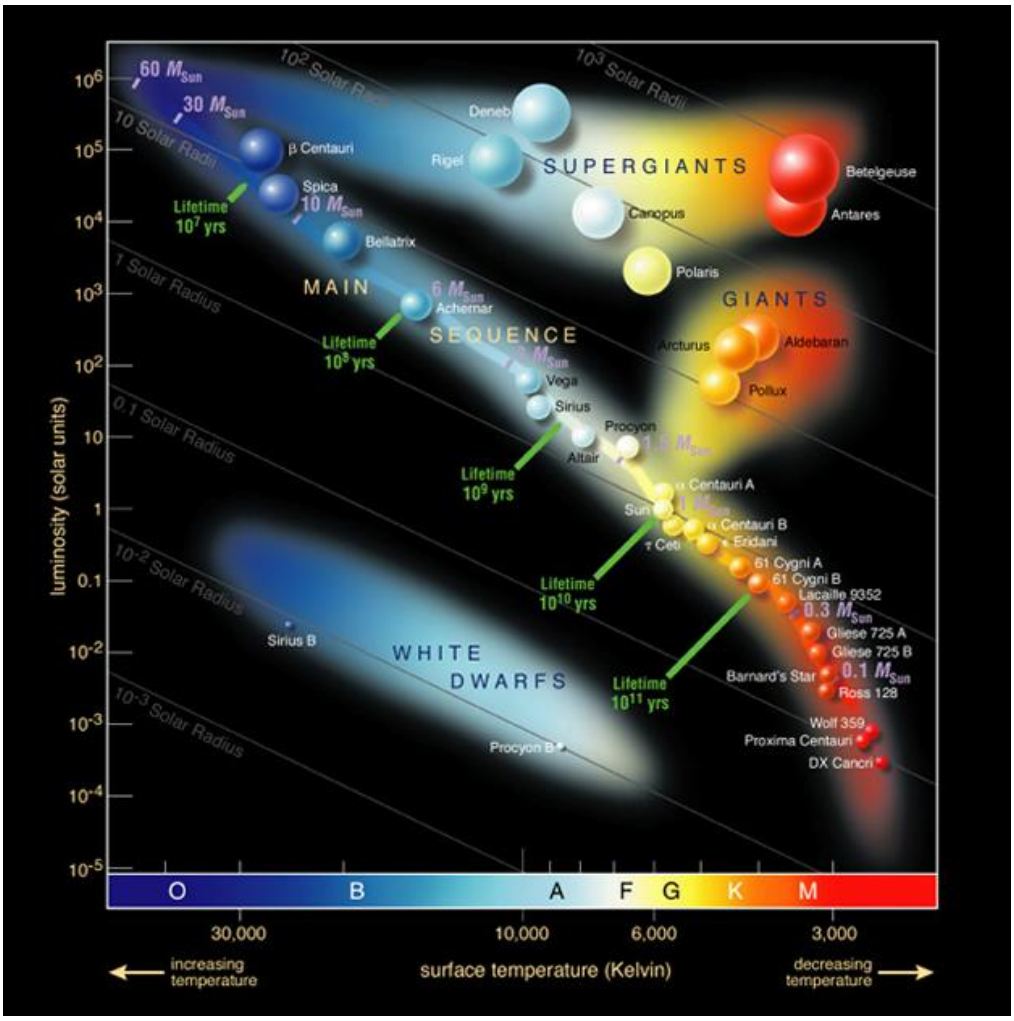


Figure 1.1: Hertzsprung–Russell diagram of notable stars of the Milky Way galaxy – luminosity increases down up and temperature increases from left to right

SOURCE FIGURE 1.1: https://www.eso.org/public/images/eso0728c/

One particularity of the H-R diagram is that, in the main sequence, the brighter the star, the larger its radius and surface temperature. Eventually, this diagram gave way to a new classification system, in usage today, named "The Morgan-Keenan Spectral Classification System" that introduced new types of stars (hypergiants, bright giants, and new types of dwarf stars) and a stricter categorization based on the effective surface temperature of the star. [17]

| Star Class | Temperature (Kelvin) | Color | Solar Masses | Solar Luminosity |
|---|---|---|---|---|
| Class O | ≥ 30,000 K | Blue | ≥ 16 M⊙ | ≥ 30,000 L⊙ |
| Class B | 10,000–30,000 K | Bluish White | 2.1–16 M⊙ | 25–30,000 L⊙ |
| Class A | 7,500–10,000 K | White | 1.4–2.1 M⊙ | 5–25 L⊙ |
| Class F | 6,000–7,500 K | Yellowish White | 1.04–1.4 M⊙ | 1.5–5 L⊙ |
| Class G | 5,200–6,000 K | Yellow | 0.8–1.04 M⊙ | 0.6–1.5 L⊙ |
| Class K | 3,700–5,200 K | Orange | 0.45–0.8 M⊙ | 0.08–0.6 L⊙ |
| Class M | 2,400–3,700 K | Red | 0.08–0.45 M⊙ | ≤ 0.08 L⊙ |

Figure 1.2: Stellar classification according to the "**Morgan–Keenan Spectral Classification System**"

However, for this chapter, a broader division of stars will be used, since stars from different classes can still meet the same end and this will be based mainly on its mass: very low mass stars – with less than 1/3 $M_\odot$ (solar mass), low to medium stars - between 1/3 and 10 $M_\odot$) and high mass stars (with more than 10 $M_\odot$). An interesting perspective on star evolution is the fact that the difference between high mass stars and low mass stars' lifetimes is so enormous that while a star like our Sun might live for 10 billion years ($10^{10}$ yr), a super massive star may only live for approximately 3 to 4 million years (3.-4 $10^6$ yr). As an example, it would be the same as having, in the same cluster, a new born Sun-like star that would be just entering the main sequence, while a high mass star born at the same time would have already formed, gone through all its evolution stages and "died".

In this thesis, we'll be paying attention to the case of the low to medium mass stars since it is in this group that white dwarfs will be formed.

SOURCE FIGURE 1.2: http://astronomyisawesome.com/universe/types-of-stars-in-astronomy/

### 1.1.2. The importance of mass as the defining factor of a star's properties and stellar evolution of a Sun-like star

Since stars produce energy in their cores by fusing hydrogen (H) into helium (He), and the rate at which this process occurs will depend on the pressure being generated in its core due to its mass, the value of its size is then directly correlated with its surface temperature and, consequently, its life span. To put it in other words, the harder the H is "compressed" inside the star, the faster the fusion takes place, and therefore, stars with bigger masses burn more brightly but also run out fuel faster and have, thus, shorter lives spans.

The lower mass star we are more familiar with is our sun, which is currently 4.6 billion years into its 10 billion years' life span. During their lifetime, low mass stars like the Sun proceed to fuse H in their cores and create as a sub product He that keeps accumulating since, at this stage, it cannot be used as fuel since the right pressure condition still has not been reached. This will result in an incremental rise in core density and pressure, and consequently, temperature. Eventually, the slow and gradual rising of the temperature of the core spreads throughout all the other layers resulting in a steady increase of brightness. For example, our Sun is now 40% brighter than when it was born. However, this fusion process stops once the star runs out of H.

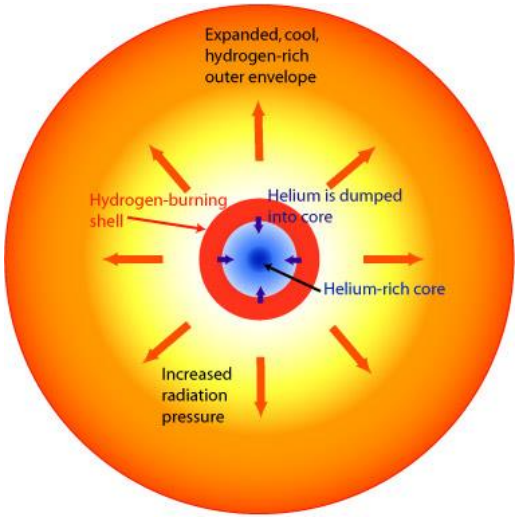


Figure 1.3: Diagram of a Red Giant and its hydrogen burning shell

For the new phase to begin – He fusion – a certain temperature value is required and that takes some time to reach since the star is no longer producing energy. What happens is that the star, albeit fusionless, is still experiencing compression which increases its temperature and, eventually, the necessary temperature value will be reached outside of the core, resulting in the beginning of He fusion through all outer layers including the shell. In other words, what happens is the conversion of gravitational potential energy into thermal energy.

SOURCE FIGURE 1.3:
ttp://www.atnf.csiro.au/outreach/education/senior/astrophysics/stellarevolution_postmain.html#postmainhb

This rise in the temperature of the shell, which is basically a gas, will make it univariably expand along with all the outer layers of the star, entering what is known as "the red giant" phase, where the star can double its original size. This red subgiant will emit more energy but will also be cooler at the same time since surface area has increased, and thus the energy per surface area unit has in fact decreased.

On the other hand, the core is still contracting and heating up as the expansion process continues. This will make the star into a true red giant that may be 10 to 150 times bigger than its original size. As an example, in the case of our Sun, it would correspond to an expansion of 0.1 AU (15 Gm) to 2 AU (299 Gm) and an increase of luminosity to 2000 times higher than the present day.

An interesting effect that happens during the red giant phase is that, due to the massive expansion, the gravity of the surface decreases so much that radiation pressure will overwhelm it, causing the star to lose material as if it were blasted all around it and up to 1/3 of its original mass. This radiation pressure results from the pressure that electromagnetic radiation exerts onto what it encounters on its path. In other words, this is a momentum transfer between photons and the objects they interact with, either by absorption and/or reflection and is dependent on the temperature of the surface.

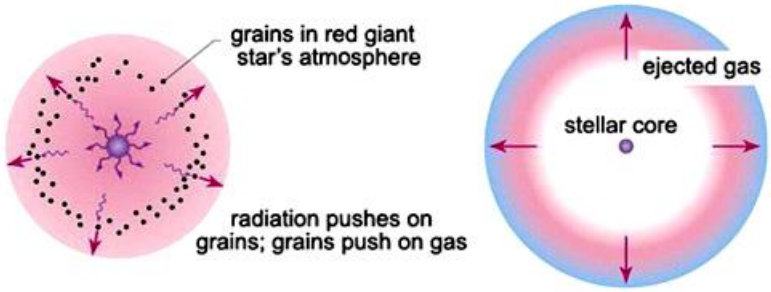


Figure 1.4: Diagram showing the effect of radiation pressure in a red giant and how it affects the mass distribution in the star

It is at this point that the conditions for He fusion in the core are met: He is then converted to carbon which results, not only in the production of a large amount of energy, but some neon and oxygen as well. Now in the core, carbon is being accumulated as He was before. However, contrary to the earlier stage, the core will instead reabsorb most of the energy it produces and expand. Since less energy will be reaching the outer layers, they end up contracting which makes the surface temperature hotter again and turning the star orange. The star has now become 10 times bigger and emits 20-50 times more energy than when the red giant phase began.

SOURCE FIGURE 1.4: http://www.cefns.nau.edu/geology/naml/Meteorite/Images/RadiationPressure.jpg

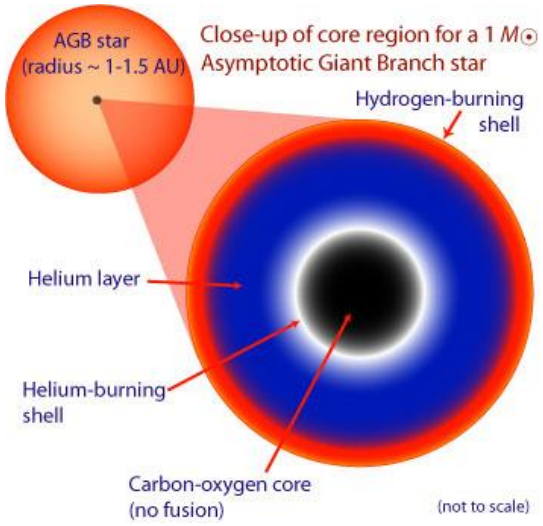


Figure 1.5: Diagram of a AGB star and the processes occurring on each layer

Nevertheless, since carbon has been accumulating steadily, the core will eventually start to contract again and heat up, similarly to what happened during the earlier "red giant phase". The star is now called an AGB star named after the section "Asymptotic Giant Branch" in the H-R diagram where evolved cool and luminous stars can be found. The new process of expansion this time will result in a bigger and brighter red giant, which also means a lot more material is lost: approximately 50% of its remaining mass.

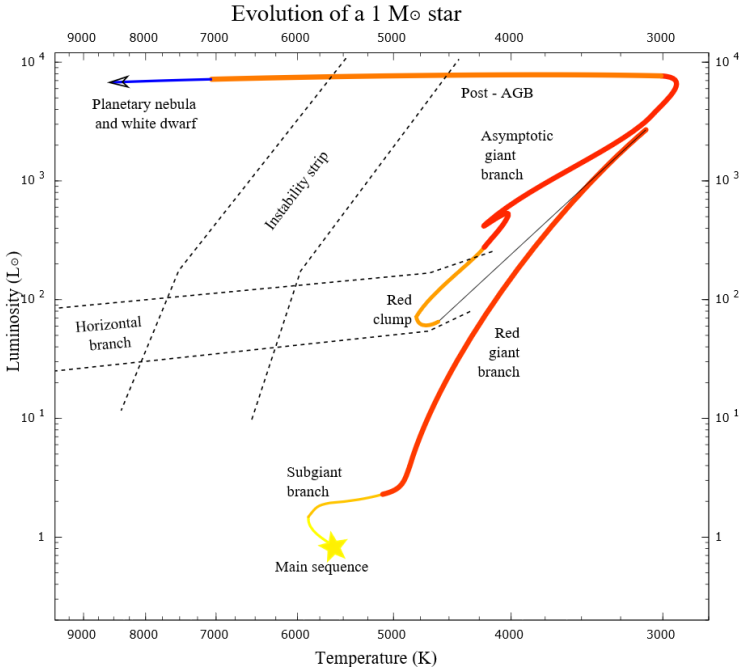


Figure 1.6: H-R diagram of a Sun-like star (1 M⊙ where the different sequences are highlighted in different colors

SOURCE FIGURE 1.5:
http://www.atnf.csiro.au/outreach/education/senior/astrophysics/stellarevolution_postmain.html#postmainhb

SOURCE FIGURE 1.6: //en.wikipedia.org/wiki/Asymptotic_giant_branch#/media/File:Evolutionary_track_1m.svg

Nonetheless, since He fusion is a much more unstable process there will be an increase in stellar activity such as flares (ejection of energy and X rays in all directions at the speed of light) or mass eruption (CME: coronal mass ejection – cloud of magnetized particles that may take up to 3 days to reach Earth, for the case of our Sum) due to peaks in energy production. On its final stage, there will be no more He to fuse and carbon will have accumulated to the point of making most of the star. Despite this, due to its size the star cannot generate enough pressure, and with it, the necessary raise in temperature to start carbon fusion.

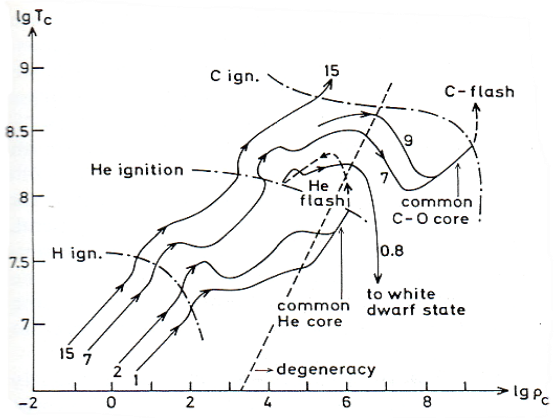


Figure 1.7: Evolution of central temperature (K) with the density (g $cm^{-3}$) of stars ranging from 0.8 $M_\odot$ to 15 $M_\odot$

In the end, almost only the core of the star will remain, making it Earth sized. The ejected matter will have formed a gas cloud around the star called a planetary nebula, which may take thousands of years to dissipate. This star is now called a white dwarf and since it cannot produce energy it will cool off until it becomes a dead star. Nevertheless, it should be noted that not all white dwarfs form a planetary nebula. [15] [18] [19]

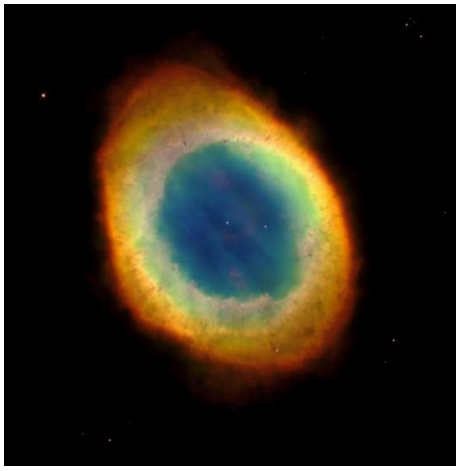

Figure 1.8: Image of the Ring Nebula from Hubble Space Telescope

SOURCE FIGURE 1.7: [19] / SOURCE FIGURE 1.8: https://www.e-education.psu.edu/astro801/content/l6_p4.html

## 1.2. White dwarfs

In this section, we will be focusing in white dwarfs since it this type of star that enables the study of planetesimal remains using spectroscopy as proposed in the abstract.

### 1.2.1. White Dwarf composition, degenerate matter, and electron degeneracy pressure

White dwarfs are one of the possible final evolutionary states for a star and it is estimated that it may be the case for over 97% of the stars in our galaxy. [16] In fact, there is a lot to be said about the internal structure of white dwarfs and their evolution, and dynamics.

This type of star is made of carbon with traces of elements such neon and oxygen and mainly of electrons. This is precisely why it also called a degenerate star since these electrons were stripped from their parent nuclei, atoms of H and C, forming a degenerate gas or electron-degenerate matter.

This component is then vital to define all the star's properties, namely, density and luminosity and explain how it comes to be. Since there is no fusion present what keeps the former core and now white dwarf star from collapsing is something called electron degeneracy pressure. This force results, not from the electric repulsion that same charge particles experience, but from "The Pauli Exclusion Principle", meaning that no two fermions (particles with the 1/2 spin like the electron) may have the same quantum number, or in other words, two electrons cannot occupy the same identical state. Another way to explain this pressure is that, as the star contracts, since the lowest energy levels are all occupied, electrons must fill higher and higher energy levels which generates pressure.

Interestingly, this pressure does not depend on the temperature since degenerate gas, albeit being very close to a perfect conductor of heat, does not follow normal gas laws (it does not expand when heated). In fact, thermal heat is being stored by the ions from which the degenerate electrons originate since degenerate matter has no considerable heat capacity. Pressure will then depend instead on the density and kinetic energy of these degenerate electrons, which are travelling to speeds close to that of light and do not interact much with ordinary matter. As a matter of fact, when this type of gas is compressed, it takes the characteristics similar those of a solid/metal: when mass (per volume unit) increases, it increases the gravitational pull between particles and, consequently, the pressure will also increase since the particles have less space to move and thus the object will become smaller. [15] [18]

### 1.2.2. Chandrasekhar limit

The existence of this balancing "force" is bound to the criteria that the stellar body must be less than 1.44 solar masses for electron degeneracy to be able to counter gravitational pull and ensure that a very cold object still has enough pressure to maintain a state of hydrostatic equilibrium (when outward thermal pressure from below and the weight of the material above pressing inward are balanced, meaning gas/plasma is at rest). This limit of maximum mass for a white dwarf has the name of Chandrasekhar Limit ($M_{Ch}$) and states that beyond this value, electron degeneracy will fail and the star will collapse. [18] [20]

Actually, the relation between the mass and the radius of a white dwarf, a spherically symmetrical star of a given composition, can be derived by considering the laws of conservation of energy, momentum and mass as well as the law of transfer of energy in the presence of a gradient of temperature. In order to do this and also determine the Chandrasekhar mass limit, we can find a simple solution of the structure equations by assuming a scenario for zero-temperature stars and by representing them by their extreme limits: the center and the surface.

By making these assumptions only two equations will be needed: the mass conservation (equation 1.1) and the hydrostatic equilibrium (equation 1.2):

$$\frac{dm}{dr} = 4\pi r^2 \rho \quad (1.1)\,, \qquad \frac{dP}{dr} = -\frac{Gm\rho}{r^2} \quad (1.2)$$

Here ρ is density, G is the gravitational constant, r the radial variable and m the mass inside a sphere of radius r.

Considering the boundary conditions: $m(0)=0$ (center) and $P(0)=R$ (surface), and knowing the equation of state P is dependent on ρ and $\mu_e$ (chemical composition), the equation system is completed.

However, instead of solving the equations above and reformulating the system into a second-order differential equation, we can opt for a simpler dimensional analysis that will still allow us to understand the mass-radius relation without having to solve the equations.

From the equations 1.1 and 1.2 it can be derived the general relations for the pressure and density in the center of the star:

$$P_c \propto \frac{GM^2}{R^4} \quad (1.3), \qquad \rho_c \propto \frac{M}{R^3} \quad (1.4)$$

By assuming a low-density model ($x<<1$ , $\rho<<\rho_0\mu_e$) and a non-relativistic solution for the equation of state (1.5):

$$P = \frac{8P_0}{5\rho_0^{5/3}}\left(\frac{\rho}{\mu_e}\right)^{5/3} = \frac{3^{2/3}h^2}{8^{2/3}5\pi^{2/3}mH^{5/3}}\left(\frac{\rho}{\mu_e}\right)^{5/3} \quad (1.5)$$

We can combine equations 1.5 with 1.3 and 1.4 to obtain:

$$P_c \propto \frac{P_0}{(\rho_0 \mu_e)^{5/3}} \frac{M^{5/3}}{R^5} \quad (1.6)$$

For the gas of the star to be at rest, the gravitational pressure (expressed by the equations 1.3 and 1.4) must be in equilibrium with the electron pressure (1.6), which is enabled by adjusting the radius of the star and, in turn, gives us the mass-radius relation:

$$R \propto \frac{P_0}{G(\rho_0 \mu_e)^{5/3}} M^{-1/3} \quad (1.7)$$

It should be notes, nonetheless, that the constants that were neglected above were dimensionless and do not interfere with the conclusion that we can derive from the relation 1.7: the radius of a white dwarf decreases with the increase of mass (when the stars have low density).

In contrast, when we consider stars with higher central densities, which is the highly relativistic case, the electron pressure is described as:

$$P_c \propto \frac{P_0}{(\rho_0 \mu_e)^{4/3}} \frac{M^{4/3}}{R^4} \quad (1.8)$$

For this case both pressures will depend on the radius and the equilibrium condition will only be valid for a specific mass value, the Chandrasekhar mass:

$$M_{ch} \propto \frac{\left(\frac{P_0}{G}\right)^{3/2}}{(\rho_0 \mu_e)^2} \propto \frac{(hc)^{3/2}}{G^{3/2} H^2 \mu_e^2}, \quad (1.9)$$

The relation above no longer depends on R and one could assume hydrostatic equilibrium is possible at any R value. This is, however, unrealistic since it assumes that $\rho$ is infinite and $R$=0.

In fact, the proper interpretation is that the gravitational and electron degeneracy pressure balance is only possible when the mass of the star is equal to $M_{ch}$. If the value of the mass is superior to $M_{ch}$ , the star collapses under gravitational pressure. On the other hand, if the mass is inferior to $M_{ch}$ , electron degeneracy pressure wins and the star expands until equilibrium is reached at a finite radius value.

[The reasoning developed from page 19 until here was based on the chapter 3 from the source [39]]

In conclusion, from the results presented above, we can conclude that the higher the mass of the white dwarf the smaller its radius will be. When a relativistic approximation is considered, we obtain a limiting value for the mass of the white dwarf, the Chandrasekhar Limit ($M_{limit} = M_{Ch} = 1.44\ M_\odot$) above. [14]

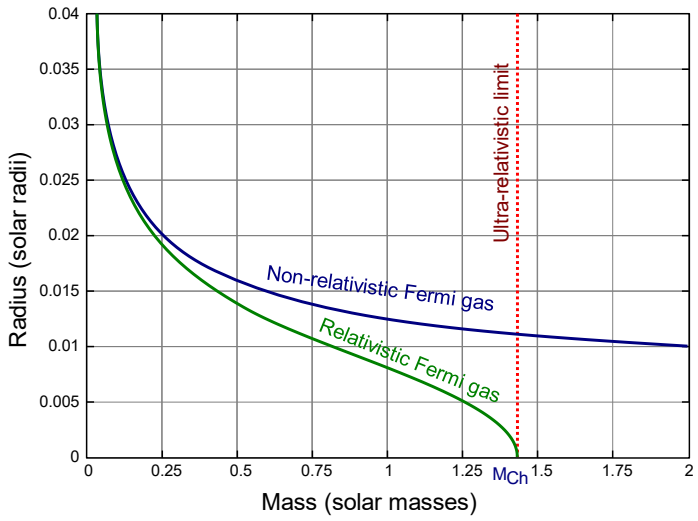


Figure 1.9: Relation between mass and radius for a modeled white dwarf (where $M_{Ch}$ represents the Chandrasekhar limit mass)

The graphic above shows how the mass of the white dwarf varies for both non-relativistic (blue) and relativistic (green) models. Even if both curves represent a degenerate gas in hydrostatic equilibrium, the relativistic approximation is more exact and close to what is expected to happen.

There are cases of white dwarfs whose mass comes close to this limit, mainly from accreting material from a companion star, they may end up exploding into nova or supernova, depending on the characteristics of the star. [15] [18]

SOURCE Figure 1.9: https://en.wikipedia.org/wiki/White_dwarf#Metal-rich_white_dwarfs

### 1.2.3. White dwarf structure

As it was established before, the structure of white dwarfs is dependent on two different phenomena: the electron degeneracy pressure that counters the gravitational pull, and the inner thermal energy stored by ions left from the creation of the degenerate gas. In a concise form, a white dwarf can then be described as "a homogenous, isothermal gas, with negligible radiation pressure and no nuclear reactions" [2]. Nevertheless, despite being comprised of mostly electron-degenerate matter, the white dwarf is not a pure homogenous object. In fact, its density decreases with the increase of the distance to its core, tending to zero near the surface, where a thin layer of gas will in fact behave like an ideal gas instead of a degenerate one.

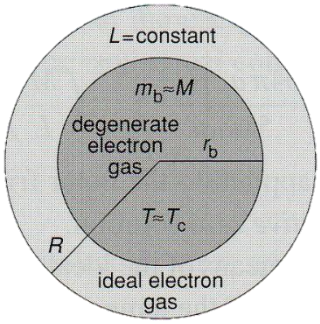


Figure 1.10: Diagram of the configuration of a cooling white dwarf where $T_c$ is central temperature, $R$ the total radius of the star, $r_b$ the radius of the degenerate gas portion of the star, $M$ the mass of the star and $L$ it's luminosity

Along with the density, the temperature also decreases and a state of radiative equilibrium is assumed on this layer. Thus, it is the temperature gradient that determines the star's luminosity. In order to simplify the system, we can make a few assumptions that will allow us to determine the relation between the pressure and temperature of the white dwarf:

1. Instant transition from the degenerate gas to the ideal gas
2. At the transition border, the value of the pressure for the degenerate gas and for the ideal gas is the same
3. The temperature throughout the core is constant and equal the temperature of its center:

   *T(r<rb) = Tc, rb* = radius of the core

4. Luminosity is constant beyond the transition border: *L(r>rb)* = const
5. The mass of the outer layer: m(r>rb)≈M.

SOURCE Figure 1.10: [15]

We this we can finally write the equations for the outer layer:

- From the hydrostatic-equilibrium equation ($m = M$): $\frac{dP}{dr} = -\rho \frac{GM}{r^2}$ (1.10)
- From the radiative-transfer energy equation ($F = L$): $\frac{dT}{dr} - \frac{3}{4ac}\frac{\kappa\rho}{T^3}\frac{L}{4\pi r^2}$ (1.11)

  where $\rho$ represents density of the gas, $\kappa$ opacity of the gas, and a is the radiation constant ($a = 4\sigma/c$).

And from Kramers opacity law,

$$\kappa_{ff} = \frac{\kappa_{ff,0}}{\mu_e}\langle\frac{Z^2}{A}\rangle \rho T^{-7/2} \approx \frac{1}{2}\,\kappa_{ff,0}\,(1+X)\,\langle\frac{Z^2}{A}\rangle \rho T^{-7/2}$$

assuming a power-law dependence on temperature and density, we arrive at the expression for

- $\kappa = \kappa_0 \rho T^{-7/2} = \frac{\kappa_0 \mu}{R} P T^{-9/2}$ (1.12)

  Where $\kappa_o$ represents the photospheric opacity or Planck mean opacity, $\sigma$ is the Stephen-Boltzmann constant, $R$ is the star's radius and $\mu$ is the degree of the gas' ionization.

By substituting equation 1.12 into equation 1.11, we can then divide equation 1.10 by the new equation 1.11 and, finally obtain the relation for a white dwarf's pressure in function of its temperature:

- $P\,dP = \frac{16\pi acRG}{3\kappa_0 \mu}\frac{M}{L} T^{15/2}\,dT$ (1.13)

Now, by integrating from the surface ($P$=$T$=0) to the core, we can obtain a relation that expresses the variation in pressure in function of the temperature and is called the radiative zero solution, which can only be applied to the star's photosphere.

- $P(T) = \left(\frac{64\pi acRG}{51\mu\kappa_0}\right)^{1/2}\left(\frac{M}{L}\right)^{1/2} T^{17/4}$ (1.14)

If we revert pressure to density, this time we can obtain a white dwarf's density in function of its temperature:

- $\rho(T) = \left(\frac{64\pi acRG}{51\mu\kappa_0}\right)^{1/2}\left(\frac{M}{L}\right)^{1/2} T^{13/4}$ (1.15)

Furthermore, we can also obtain the relation between a white dwarf's surface luminosity and core temperature from equation 1.15 and matching the equations for the degenerate-electron pressure ($P_{e,deg} = K_1'\left(\frac{\rho}{\mu_e}\right)^{5/3}$) with ideal-electron pressure ($P_e = \frac{R}{\mu_e}\rho T$):

- $\frac{L}{M} = \frac{64\pi acG K_1'^3 \mu}{51 R^4 \kappa_0 \mu_e^2} T_c^{7/2}$ (1.16), where $K_1'$=$10^7 m^4 kg^{-2/3} s^{-2}$ and $\mu_e$ is the average molecular weight per electron.

[The reasoning developed from page 22 until here was based on the chapter 9 from the source [15]]

To sum up, this complex force system creates and maintains an incredibly stellar object with even more incredible characteristics:

- → Size: 0.8-2% $R_\odot$ (for comparison the Earth is 0.9% $R_\odot$)
- → Mass: 0.17-1.33 $M_\odot$ (majority at 0.5-0.7 $M_\odot$)
- → Gravity ~ $10^5$ times stronger than Earth's
- → It is extremely dense: a cup filled with this matter would weight about 1 ton ($10^{4-7}$ g/c$^3$)
- → It is extremely hot, having a core temperature of $10^7$ K
- → Has high internal thermal conductivity, which keeps the interior of the star at a uniform temperature.
- → Emits abundantly in higher energies such as UV and X-Ray (when young $T_{eff}$>30 000 K)

[1] [22]

### 1.2.3. White dwarf cooling period

It could be wrongly perceived that such a hot star without an inner reactor would quickly cool off. In reality, since the star has such a small surface, very little heat can escape at a time, which makes the star not only luminous but also leads to its surface temperature being around 8 000 to 40 000 K. As a matter of fact, the opacity of most of the white dwarf is very low due to being made of almost totally of degenerate matter. This happens because for the photon to be able to be absorbed it is necessary that the target electron has a matching quantum state available. Since most of the low states are already occupied, the star's heat capacity is thus quite low. It is expected, nonetheless, that as the star cools down its color will become redder and its luminosity fainter. [16] [20]

This can be confirmed by determining the relation between the white dwarf's luminosity and its core temperature. By taking into account that the white dwarfs' energy source is thermal energy accumulated in the ions of its core, the energy emission rate can be calculated:

- Inner thermal energy: $U_I = \frac{3}{2}\frac{R}{\mu_I} M T_c$ (1.17)
- Energy emission rate: $L = -\frac{dU_I}{dt} = -\frac{3}{2}\frac{R}{\mu_I} M \frac{dT_c}{dt} = -\frac{3}{7}\frac{R}{\mu_I} M \frac{T_c}{L}\frac{dL}{dt}$ (1.18)

Using the equation 1.16 mentioned earlier and applying it to equation 1.18, we obtain: $-\frac{dL}{dt} \propto M T_c^6$ , which leads us to the conclusion that the rate of variation of the luminosity decreases exponentially with the core temperate of the star. This also allows us to make another conclusion: a lower mass white dwarf will evolve a lot more slowly than a higher mass one because it will cool off less quickly.

To be able to calculate the time that a white dwarf would take for its core temperature to diminish from an initial value *Tc'* to a lower *Tc* (or to have its luminosity decrease to *L'*) can be obtained by integrating the equation VI:

- $\tau_{cool} = 0.6\frac{R}{\mu_I} M \left(\frac{T_c}{L} - \frac{T_c'}{L'}\right)$ (1.19)

If $T_c' \gg T_c$ , then according to equation 1.16 the time necessary for the white dwarf to cool to a lower temperature $T_c$ is:

$$\left(\frac{T_c'}{L'} \ll \frac{T_c}{L}\right) \rightarrow \ \tau_{cool} \approx 2.5 \times 10^6 \left(\frac{M/M_\odot}{L/L_\odot}\right)^{5/7} yr \quad (1.20)$$

The total cooling period will, therefore, last tens to hundreds of billions of years, and since the universe is younger, all existent white dwarfs (in single-star systems) still have not degenerated into black dwarfs, which explains why none has been detected.

[The reasoning developed on this page was based on the chapter 9.8 from the source [15]]

As an interesting note, the oldest and faintest white dwarf was discovered orbiting a pulsar and is estimated to be 11 billion years old (same age as our Galaxy) and having a temperature of about 3000 K (2700ºC). [23]

Finally, it is also interesting to point that most white dwarfs spend the greatest part of their lifespans at lower temperature rather than at higher temperatures. This happens because once it reaches very low temperature the gas stops being ideal and Coulomb interactions take over. Consequently, the cooling rate stops following the equation 2.18 and will end up accelerating considerably. In reality, what happens is that the original ion gas composed by electrons and nuclei (plasma) starts to crystalize into a periodic lattice. There have been some stars suspected of being partially or even totally crystalized white dwarfs, being popularly called "white dwarfs made of diamond". [15] [23]

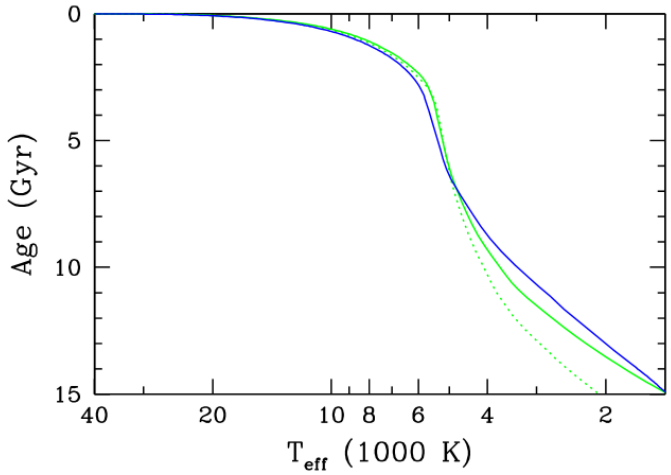


Figure 1.11: Cooling age of white dwarfs in function of their effective temperature - the green line represents a white dwarf of 0.6 M with an H layer and different core compositions: pure C core (dotted) vs C/O=1 core (solid) – the blue line represents white dwarfs without the surface H layer.

An example of the evolution of the temperature of white dwarfs with age can be seen in the figure above, where the effective temperature of a white dwarf decreases as the star ages. At the beginning the very young white dwarf loses its thermal energy mainly by emitting neutrinos. The cooling starts to slow down considerably at about 8000 K. At this point, the cooling rate depends on how much energy is accumulated in the core and the efficiency of radiation transport though the opaque outer layers, especially in the envelope where it is the slowest, and then through the interstellar medium. In fact, it is the star's outer layers' opacity to radiation that keeps the white dwarf from cooling rapidly since degenerate matter is an excellent heat conductor. The heat will be dispersed due to radiative diffusion and there is the formation of convective zones that transport heat more effectively from deeper layer to the surface. As the stars gets cooler the deeper the convective zones extend until eventually they reach the core.

From the previous figure, we can also conclude that for lower temperatures, the cooling rate will depend on the composition of the star's core (pure C core – dotted green will cool faster than O and C core – green line) and its atmosphere: since He is more transparent to radiation than H, a star without H in its atmosphere will cool faster. (H layer star - blue line vs non-H-layer star-green line). [24]

SOURCE Figure 1.11: http://whitedwarf.org/theses/kowalski.pdf

### 1.2.4. Types of white dwarfs: spectral classification and spectral evolution

As discussed in a previous section, in the last phase of evolution, AGB stars loose more than half of their mass because of irregular energy production, resulting from thermal pulses generated by alternating fusion of H or He in thin shells. The moment that will mark the end of the AGB star is when it finally scatters the rest of its envelope and this takes place at random during a pulse. Therefore, it could occur either during H fusion or He fusion. If it happens during the first (H fusion), the star will have a fine layer of hydrogen, a remnant of the dissipated outer layers. However, if it happens during the very short lived He fusion, that takes place on the inner He shell before the H layer, all that will be left after the explosion will most likely be a pure He coating.

Thus, the vestige of this process will be a white dwarf pertaining to one of the categories: the most common – one that exhibits H lines; or one which has He lines instead and no trace of H.

There is one extra type of white dwarfs that result from the stellar evolution of extremely low mass stars (0,7 $M_{\odot}$<M<1 $M_{\odot}$). The defining characteristic of these stars lies in their inability to reach He fusion due to their diminutive mass, becoming red giants and skipping the He fusion phase along with the AGB and planetary nebula phases. The resulting white dwarf will be mainly a helium core of between 0,2 and 0,4 $M_{\odot}$, the second most common type of white dwarfs found.

The spectra emitted by white dwarfs allow us to obtain important information on the characteristics of a star such as: temperature structure by studying its effective temperature, and pressure stratification by determining surface gravity and chemical composition of the atmosphere. To better classify white dwarfs, a new classification system was created based on the composition of its atmosphere and the lines identified in its spectrum. A star would then be classified as a D, for dwarf, and then one or more letters from the table in figure 1.11 to describe its characteristics.

**White dwarf spectral types**[25]

| Primary and secondary features | |
|---|---|
| A | H lines present; no He I or metal lines |
| B | He I lines; no H or metal lines |
| C | Continuous spectrum; no lines |
| O | He II lines, accompanied by He I or H lines |
| Z | Metal lines; no H or He I lines |
| Q | Carbon lines present |
| X | Unclear or unclassifiable spectrum |
| **Secondary features only** | |
| P | Magnetic white dwarf with detectable polarization |
| H | Magnetic white dwarf without detectable polarization |
| E | Emission lines present |
| V | Variable |

Figure 1.12: Table with white dwarf spectral types classified by different lettering

SOURCE Figure 1.12: https://en.wikipedia.org/wiki/White_dwarf

As an example, a white dwarf whose atmosphere is mainly H would be classified as a DA type, which constitute approximately 80% of all detected white dwarfs. This subtype can be found across a wide range of temperatures (6000 K -70 000 K) and almost all Balmer lines should be visible.

The next category includes star with He dominated atmospheres where are included the DB, DC, DO, DZ and DQ subtypes.

The DB subtype, which accounts for roughly 18% of all white dwarfs, includes white dwarfs from 12 000 to 30 000 K where there can only be observed He I lines, with no H or metal lines present. There have also been discovered DB white dwarfs that show weak hydrogen lines, named DBA, and make up to 20% of all DB stars. Also, interestingly, there are no DB stars to be found in the range 30 000 to 45 000 K, where He I line ought to be considerably strong.

The DC subtype is consistent of DB type white dwarf stars whose temperature is below 12 000 K. The reason for the change in lettering is due to the fact that at these temperatures He lines are not visible anymore, being the continuum/optical spectra the only one observable.

The DO are He rich white dwarf stars whose temperatures go from 45 000 to 100 000K and have H abundance of at least 1%. As they cool they will become DB stars.

Finally, DQ and DZ white dwarf stars have atmospheres where the presence of other elements besides H and He can be detected, respectively, $C_2$ molecule lines (DQ) and Ca II (and at times Mg, Fe, and Si) lines in the case of DZ stars. It is to be noted, though, that metal abundances in these stars are always lower than what is observed for solar values. To see examples of spectra of different types of white dwarfs see figure 1.13.

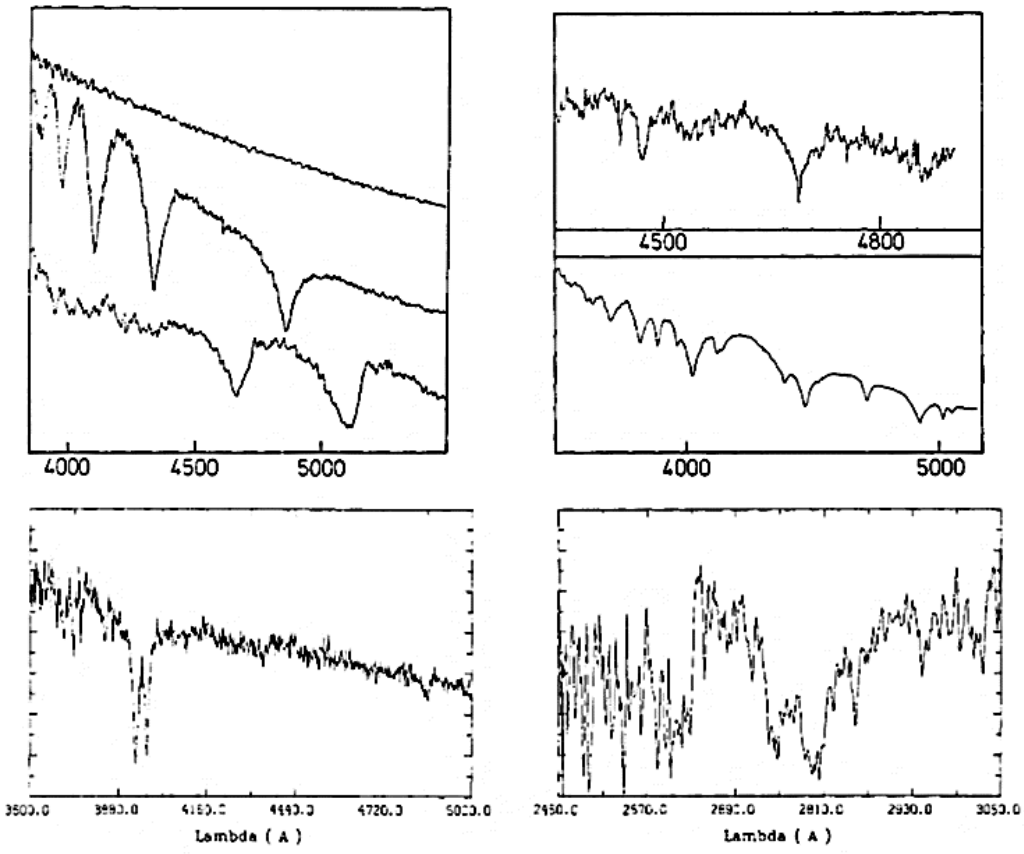


Figure 1.13: Spectra of different types of white dwarfs: left upper corner – **DQ** (former DC – L97-3), **DA** (LDS455A) and **DQ** (L870-30); left down corner – **DZA** (K789-37); right upper corner – **DO** (HZ21) and **DB** (GD353); right down corner – UV spectrum of K789-39

Despite the detailed classification system, there is also another broader way to classify white dwarfs according to their temperature, either into hot or cold white dwarfs. Hot white dwarfs are considered to include the subtypes DA, DO and DB; whereas cool white dwarf are considered to have temperature approximately below 12 000 K and include DC, DQ and DZ subtype white dwarfs. [22] [24]. The separation between cold and hot white dwarfs in practice varies a bit depending on the convention adopted by each investigator. For example, some authors consider stars with $T_{eff}$ below 20 000 K to be cold (Barstow et al. 2014 MNRAS paper) while others consider 25 000 K (Klein et al. 2010 ApJ 709)

SOURCE Figure 1.13: http://whitedwarf.org/theses/kowalski.pdf

## 1.3. Circumstellar disks and white dwarf pollution

First of all, a circumstellar disk can be defined as a disk or ring made of gas or particulate-sized matter that takes form around the star. It is to be noted that they exhibit a rather planar structure and are unlike envelopes of dust/gas or nebular clouds, which expand in 3D.

The circumstellar disks we are interested in, are set apart from previous accretion disks since they are located within the former giant star radius and, therefore, had to be produced during this evolutionary stellar stage. To put it simply these debris disk can be thought as the whole planetary system, minus the planets which are now dust. So far, hundreds of isolated white dwarfs have been discovered as having closely orbiting debris disks.

One of the signs of the presence of debris disks is when these white dwarf stars, that were expected to have a pristine stellar surface, show instead the presence of heavy elements in their atmosphere. This phenomenon is called "white dwarf pollution". In general, the surface gravity of a white dwarf is so intense that the time scale for sinking metals, from the photosphere into the star, is inferior by several orders of magnitude compared to its cooling period. Thus, in theory, white dwarfs should have pure H or He atmospheres. However, in fact, between 25% to 33% of all cooler white dwarfs (below 20 000K) exhibit metal lines in their photosphere [1] [7]. In addition, even for hot white dwarfs there is evidence for an external origin of the heavy elements detected in their atmospheres

### 1.3.1. Difficulties in detection/Infrared emission

When it comes to detection, even though it is easier to detect planets around white dwarfs than other main sequence stars due to their low luminosity (up to less 10 000 less than our Sun), this characteristic also makes it difficult to spot these disks that derive their luminosity from the star they orbit (the first white dwarf with a hot circumstellar disk was found in 1987 and the second only in 2005 [22]). In fact, dust disks are almost exclusively detected around white dwarf with $T_{eff}$> 10 000 K, even though cooler stars are known to accrete matter as well. [5]

What happens is that the particles of the disk absorb in UV and reemit in the infra-red (IR), which facilitates the discovery of certain white dwarfs that otherwise would be missed. Still, the dust itself is notoriously very difficult to detect and study. So far, the number of elements detected through spectroscopy of disk-lines is smaller than the number of species detected through white dwarfs' atmosphere lines. This is why astronomers/astrophysicists depend on the "falling" of this dust material to the white dwarf atmosphere to be able to study it properly. Thus, this infrared emission became the first insight associated with white dwarf search parameters. [1] [5]

On the other hand, there are instances where the dust that composes the debris disk produces infrared excess emission and can outshine the white dwarf itself, especially if the white dwarf has a companion. [1] [2]

There are types of disk that can, however, miss detection: fully gaseous disks; very narrow disks, that despite possibly being opaque, do not have enough surface area; and disks whose dust that is too thin optically, meaning that there are not enough emitting grains.

### 1.3.2. White dwarf pollution characteristics: settling time and cooling time

As it was referred before, metals in the white dwarf's atmosphere should have an external source since the star can only sustain heavier elements in its photosphere during the short period while it's a relatively young white dwarf. In other words, because the star will still be contracting and emitting heat, the generated radiation pressure will work against downward diffusion due to gravity and keep heavy components afloat. [24]

Any white dwarfs whose temperature reaches a value less than 25 000 K ($T_{eff}$ < 25000K), starts to exhibit convection which increases the gravitational settling and, along with its high surface gravity, leads to a quicker sinking of metal elements present in its atmosphere. In fact, the accretion rate may have to reach values of up to $10^8$ g/s just to sustain the metal present in the atmosphere. [1] [5] The reason why this is an average is because accretion rates are very hard to calculate since they depend on estimates of the bulk composition from the disk versus a scaling of the observed one in the atmosphere. The more convective the layers of the star, the harder it is to estimate.

Since the downward diffusion process takes a lot less time than the stars' own cooling timescale, this process should be over long before any considerable decrease in the star's temperature is reached, which lead us to the conclusion that any metals in the photospheric layer should be externally sourced. [1] [5]

In addition to this, one of the differences between DA stars and DB stars, for temperatures between 20 000 and 30 000 K, is the fact that DB stars develop a convective zone, where the plasma is homogenously mixed, which leads to longer diffusion times. [1] [2] To further illustrate this, when it comes to settling time of atmospheric metals, for DA stars it is less than 100 years whereas in DB stars it could be longer than 100 000 years. Also, lines detected in DA and DB stars, for the same abundance, will appear to be stronger in a He-rich atmosphere (DB) than in a H-rich atmosphere (DA). This is because He opacity is a lot lower than that of H. Both these characteristics, favor the study of DB stars when studying a small population of white dwarf stars. [7]

### 1.3.3. Possible origins of matter of the debris disks and models

The existence of a debris disk serves as a mean to mainly facilitate the deposition of metals in the photosphere, regardless of source. There are 3 main possible sources for the heavy metals present in a white dwarf's polluted atmosphere: stellar material, interstellar medium (ISM) and debris from circumstellar environment.

Stellar material, either from primordial origin or from fallback, was the first explanation to be presented. However, this hypothesis has been refuted due to several reasons. First, there is the fact that material originated from the star should quickly sink due to its high gravity. The proof of this is the fact that pure H or He white dwarfs are the most detected types. In addition to this, most of the material resulting from the AGB phase will be removed by sublimation, engulfment, radiation pressure or drag forces, so there would never be much material to start with. Finally, there is also the cooling timeframe issue: once a white dwarf has been cooled to 25 000K, heavy elements can no longer be supported by radiation pressure. They are diffused from the atmosphere quickly, and this period could last from days to years while pollution could be observed from 30 to 600 Myr. [1] [5]

Another theory that arouse was the possibility that the interstellar medium (ISM), i.e. accretion from the surrounding interstellar gas, could be the source of these metal elements. This was initially the most accepted theory since the majority of detected white dwarfs were cool and He-rich stars. What is special about these stars is that they have rather transparent outer layers and deep convection zones, where metal diffusion can last up to 1 Myr. Consequently, occasional encounters with these gas clouds could indeed supply the necessary material and have it remain for a relatively long time in the atmosphere.

Nonetheless, the discovery of other types of white dwarfs came to discredit this theory as an explanation for all cases of polluted white dwarfs: ISM accretion cannot account for polluted and non-polluted subpopulations of white dwarfs. In this case, the types of white dwarfs in question are most of the He-rich stars polluted with metals (supposedly originated from the ISM) that are hydrogen deficient. If they were accreting interstellar matter, which exhibits similar composition to what is found in the solar system, then all should reveal a H layer and thus H lines. An example is the DBZ stars (He rich metallic white dwarf) which display a near universal lack of H.

On the other hand, the ISM single source model also could not explain the detection of metals in DAZ stars (rich in H and exhibit metal lines) whose diffusion timescale should only last days to years. Lastly, another problem detected was the lack of dense clouds in the Local Bubble (a cavity in the ISM the Orion Arm of our Milky Way galaxy), meaning no relevant amount of ISM matter should be available to justify any considerable pollution of the white dwarf stars discovered there. [1] [8]

Finally, a different possible source of debris was suggested to be the intrinsic circumstellar environment, making the dust the vestige of a former planetary system. This source led to the creation of 2 different circumstellar accretion models.

The first model to be devised was the cometary impact model and its main advantage resided with justifying the lack of H in most DBZ stars with the fact that comets would naturally be depleted of volatiles. Nevertheless, the discovery of a few stars that had a short metal diffusion rate implied that there would be a need for a continuous supply of comets to maintain the stars' photosphere pollution. Yet, the necessary debris disks could never be originated through an impact.

The second model to be created was the asteroid disruption model, which improved upon the previous model's flaws. It was modeled after the situation where a tidally-destroyed minor planet/asteroid originates a flat and opaque disk similar to that of Saturn. For this to happen, a few favorable conditions were required: the asteroid had to possess a highly eccentric orbit and pass within the Roche's limit of the star to then be torn apart by gravitational tidal waves. The dust would have then to be heated by the star to produce infrared excess and the material would be brought to the inside of the accretion disk by Poynting-Roberston drag. Finally, as it passes the Roche's limit, it would be sublimated, then accreted via magneto-rotational instability and, eventually, it would rain down onto the star's surface.

As a side note, it should be explained that the Roche's limit consists in the limit in which a stellar body, that possesses self-gravity, will disintegrate due to tidal waves of another body having stronger gravity pull than the gravity that holds the original body together. Also, the Poynting-Robertson effect mentioned takes place when the radiation pressure from the star hits small particles orbiting it that are too big to be blown away by radiation pressure, causing them to slow down and spiral towards it. This "vacuum" is formed due to the interaction between the star's radiation and gravity, effectively dragging the particle down.

Nowadays, an improved model based on asteroid disruption and accretion from exoplanetary system has been deemed the standard model, mainly due to the existence of strong evidence that a very substantial fraction of white dwarfs is indeed accreting material from extrasolar circumstellar debris, either planetary or from asteroids. The model states that asteroids should be, on average, further than 2.5 AU during the main sequence phase and have a radius bigger than 10 km, to survive the expansion and the heat and frictional drag during the ejection of stellar mass. Also, since it is a flat disk model, most of the debris mass is shielded from the full stellar radiation field and, hence, disks with cm-sized pebbles should survive being quickly destroyed by the nearby star. [1] [5] [8]

In conclusion, 3 important ideas can be highlighted: there is strong evidence that a very substantial fraction of white dwarfs are accreting material from extrasolar circumstellar debris, the tidal disruption of asteroids/planetesimals is considered to be the standard model to justify the existence of these disks, and finally, spectroscopic determination of abundances in white dwarfs' atmospheres is an indirect but powerful way to measure in detail the composition of accreted extrasolar planets. This last idea, is what the work developed on this thesis will be based on, meaning trying to learn more about the white dwarf accretion processes by studying the circumstellar and non-stellar absorption components in the UV spectra of several white dwarfs and also trying to understand where that gas is in relation to the star and the ISM around it.

## 1.4. The interstellar medium (ISM)

The universe, according to current cosmological models, is made of approximately 69% of dark energy, 26% of dark matter and 5% of baryonic matter. Baryonic matter can essentially be explained as being made of protons and neutrons along with enough electrons, which are not baryons but leptons (elementary particle with half-integer spin), so that total charge neutrality is maintained on a considerable scale. More specifically, baryonic matter can be found in two different forms: compact objects such as stars, planets and stellar remnants, which account for roughly 7% of all baryonic matter; or in diffuse form as gas and dust.

This diffuse form of baryonic matter can then be divided in different types according to its to the location: the interstellar medium (ISM) which is the volume that occupies the space between stars and solar systems in a galaxy, making 1% of all diffuse baryonic matter; the circumgalactic medium (CGM), which is trapped inside the dark halo of a galaxy, totaling 5% of all gas, the intracluster medium (ICM) that binds a cluster of galaxies together, accounting for another 4% of gas; and finally, all that lays beyond the former's scope, the intergalactic medium (IGM), reaching around 83% of all baryonic matter in the form of mostly photoionized gas and shock heated gas, generally ionized hydrogen (a plasma that has the same number of protons and electrons). It is however, to be noted, that this classification has not been standardized and other authors may take a broader approach in the divisions of all diffuse baryonic matter. Also, it should be stressed that within the space the ISM occupies there are also cosmic rays (high energy particles with relativistic kinetic energy) and electromagnetic radiation that forms the interstellar radiation field. [29] For this thesis, only the ISM will be briefly introduced and discussed since the rest falls out of scope of the data being analyzed and the objectives of this study. [28]

The interstellar medium, arguably responsible for delivering the most stunning photographs of space such as the Pillars of Creation, is the most important component of galaxies, for is through it that new stars are created. This medium was only discovered about 80 years ago while observing remote star clusters that exhibited reddening of the light emitted and absorbed by surrounding dust. Reddening is the decrease in light intensity and its shift towards longer wavelengths and is caused by the absorption and scattering of the photons crossing the ISM. What the spectra from the gas showed was the existence of narrow absorption lines, which led to the conclusion that much of the matter would be organized in clouds or absorption systems. [26]

Figure 1.14: Image of the Eagle's Nebula Pillars of Creation taken by the Hubble Space Telescope in visible light

The contents of the ISM are not static, as galaxies evolve the ISM is transformed into stars but at the same time some of it may have be ejected from the galaxy by the way of galactic winds. The intergalactic medium can also remove or deposit gas and dust in the ISM. There are also other sources of material for the ISM, namely, stars by the way of stellar winds and as they reach the end of their lives by injecting richer gas into the ISM, like in supernova blasts. An example of this dynamic can be found in the figure 1.14 regarding the Milky Way. In fact, in the case of our galaxy, only around 10% of the baryons still belong to the ISM having the majority already been converted to stars and other celestial objects. [25] [28]

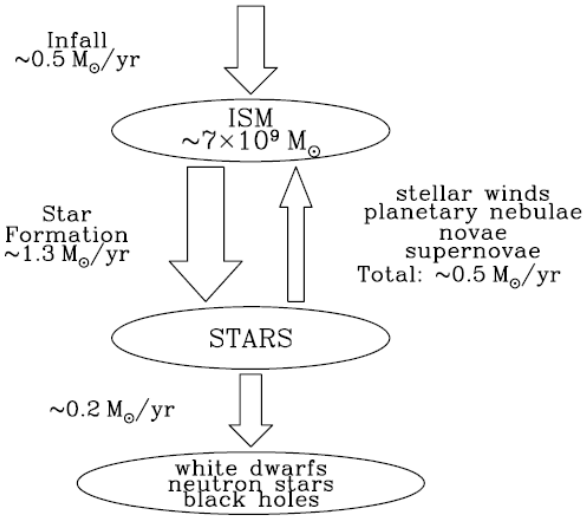


Figure 1.15: Diagram demonstrating the movement of baryons in our galaxy, the Milky Way

Alongside low-density ISM gas one also must consider interstellar dust. This dust is composed of extremely small grains (below microns) of solid or porous material made of ice, silicates, graphite, carbonaceous material and even diamond. The reason why this happens is both due to historical reasons, where dust and gas were "bagged" as the same "non-stellar material", but also because the dust and gas physically affect each other. Since the dust is made of refractory components it can effectively change the radiation that passes through the gas, which in turn can lead to a variation in chemical abundances. On the other hand, the dust particles have other import functions such as being the place where gas molecules form and where most of the free electrons are originated from. Therefore, the denser the area of ISM, the more impact interstellar dust has on the gas.

In fact, the ISM is not only characterized by the dust and gas it is composed from, it can be classified has having multiple phases according to the type of matter (atomic, ionic or molecular) that it is made of along with the its density, temperature and velocity. When it comes to the composition, the ISM is made mostly of H (91,2%), He (8,7%), both mostly resulting from primordial nucleosynthesis, and with vestigial amounts of heavier elements such as oxygen, carbon and nitrogen (0,1%), all originated through the enrichment processes that occur naturally during stellar evolution. This way, there could be more than one cloud in a given place with different abundances, velocities and temperatures. In the case they have $H_2$ as their dominant type of H, they are called molecular clouds and account for one third of all ISM mass. It is in these clouds, where the highest density values of the ISM are reached ($10^6$ molecules per $cm^3$), that self-attracting volumes appear that can, in turn, lead to the formation of stars. On the contrary, in the hotter and more diffuse areas of the ISM the density could be as low as $10^{-4}$ ions per $cm^3$. [28]

Other types of interstellar regions include:

- supernova remnants: material resulting from the explosion of a massive star or of a white dwarf that accreted material from a companion star;
- refractive nebulae: clouds of dust and non-ionized gas that do not receive enough energy from the nearby star(s) to emit light and are only able to scatter it.
- H II regions: clouds made of partially ionized gas and of low density, usually around newly formed stars.
- planetary nebulae: vestige of the stellar evolution of a low mass stars and their expansion phases and demise.

In addition, it is also extremely relevant to this thesis to discuss the place where the ISM begins and the circumstellar medium ends. The circumstellar medium begins where the star's heliosphere ends. In the case of our Solar System, the frontier is clear, it is until the place where flow of solar wind can reach, at around 120 AU [28] from the Sun called the heliopause. However, in the case of giant stars that have intermediate mass and that emit heavily in the infrared from solid particles and in the microwave range due to simple molecules, this makes the border less precise and with no clear division. [27]

Finally, it should be mentioned as well that the volume of ISM closest to the solar system is called the local interstellar medium (LISM) where usually abound warm and low density partially ionized clouds. These clouds will have the name of LISM clouds and in order to be detected, one must use space telescopes that can observe strong atomic transitions located in the UV. In the case of our solar system, the LISM is situated at approximately 100 pc from the Sun. The image 1.15 illustrates the

divisions of the circumstellar and interstellar medium referred during this subchapter applied to our Solar System, to better illustrate what has been said.

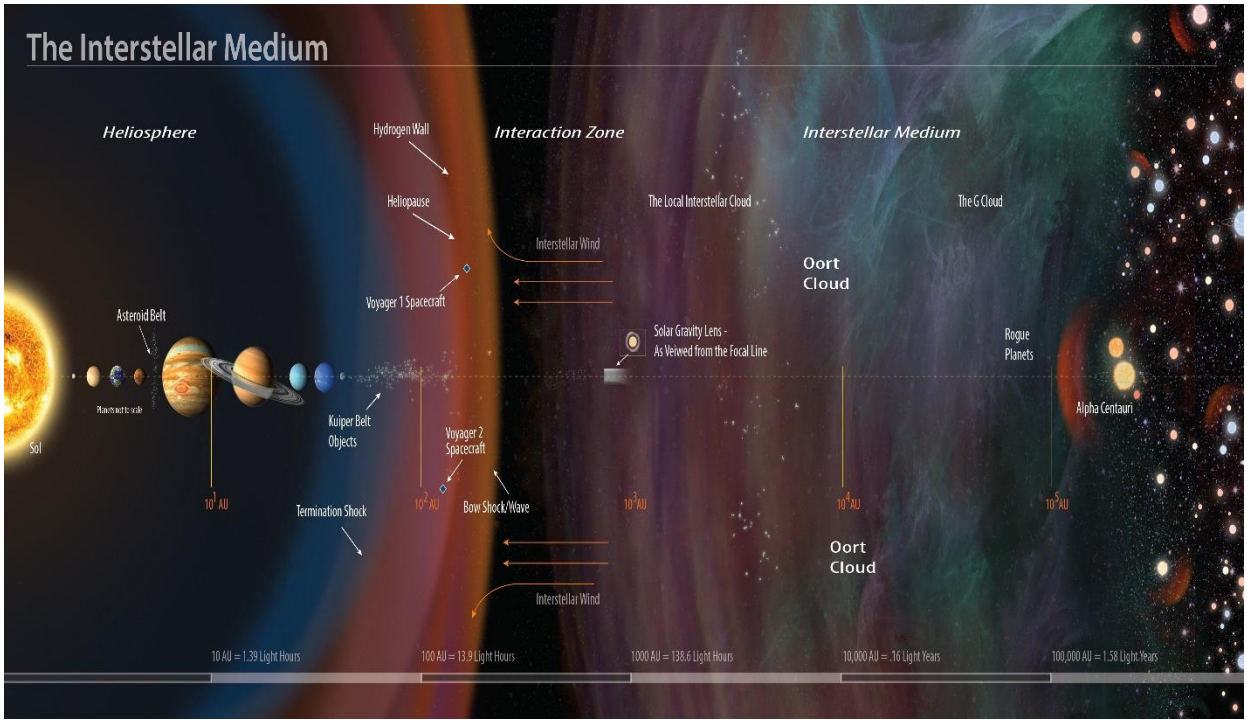


Image 1.16: A diagram of the circumstellar and interstellar medium around our Solar System and its boundaries and relevant points of interest; along with the relative positioning of the spacecrafts Voyager 1 and 2

For this thesis, observational data derived from spectroscopy, namely detection and measurement of absorption lines and other physical quantities, has been used to derive information about the regions surrounding selected white dwarf stars and their physical properties. This will be discussed in more detail in the following chapter.

SOURCE Figure 1.14: https://cdn.spacetelescope.org/archives/images/wallpaper2/heic1501a.jpg

SOURCE Figure 1.15: [25]

SOURCE Figure 1.16: http://sredfield.web.wesleyan.edu/images/ism%20graphic_07.jpg

# Chapter 2: Instruments and Methodology

As discussed in the previous chapter, the debris disks around white dwarfs are most likely formed by tidally disrupted planets or asteroids. These planetary remnants do not emit light on their own, but they absorb and reemit in the infrared, light from their parent star. Infrared spectroscopy is then one of the most powerful tools to study the physical properties of these systems and the James Webb Space Telescope, currently being built by NASA and ESA, is expected to make great contributions in this field

Another line of research into these systems has emerged in the last few years connected to the study of polluted white dwarfs with the realization that many white dwarf spectra show the presence of metals, in disagreement with model predictions, for both cool and hot white dwarfs. Several mechanisms have been proposed to explain the origin on these metals, from accretion from the interstellar medium, to accretion from planetary debris discs or even gas disks. [6]

In order to study what happens in the ISM near those polluted white dwarfs, we must be able to observe strong atomic transitions of those atoms and ions in the gas clouds. These transitions appear in the UV part of the spectrum and that are only available from space since the Earth's atmosphere absorbs it. That iss why we used data from 2 space observatories in this work: FUSE and HST/STIS

In this chapter, we describe the space telescopes used to obtain the data used in this work as well as the methodology used to process it along with an explanation of all necessary physical concepts necessary to understand it. Finally, an introduction is also made into the chosen targets and data analyzed, finishing with a brief description of the IDL methods and steps that were used to obtain the desired measurements.

## 2.1. Far Ultraviolet Spectroscopic Explorer (FUSE)

The Far Ultraviolet Spectroscopic Explorer (FUSE) was a space-based telescope/satellite developed and run by The John Hopkins University (JHU) for NASA in conjunction with the University of Colorado Boulder, the University of California at Berkeley (UC Berkeley) and international space agencies the Canadian Space Agency (CSA) and the French Space Agency (CNES).

FUSE was launched in June 1999 as part of NASA's Origins program and its purpose was to explore the Universe in the far-ultraviolet (FUV) band of the electromagnetic spectrum, more specifically from 905 to 1187 Å, using high resolution spectroscopy with a resolving power of around 20 000.

This wavelength region contains important astrophysical transitions such as the Lyman series of hydrogen and deuterium (except for Lyα), molecular hydrogen absorption bands and ground state transitions of carbon, oxygen, and nitrogen along with other metal lines such as Si, Fe, and Ar. The

detection of various lines of N I, O I and even Fe II is extremely significant since they can be used to measure the metallicity and dust in absorption clouds.

The FUSE mission lasted 8 years until 2007, and while its primary goals were to study deuterium in the universe and the chemical evolution of galaxies, it observed an incredible number of targets, nearly 3000, and spanning a wide range of object types from stars to planets and comets, to even quasars and erroneously thought to be empty regions of interstellar and intergalactic space. All the data it collected is currently stored on the Mikulski Archive for Space Telescopes (MAST), from which all the data analyzed in this thesis was retrieved. [11] [14]

### 2.1.1. FUSE – Instrumentation and design overview

The FUSE observatory was 5,5 m long by 1,9 m and was divided into two main sections: the spacecraft itself and the science instrument. The spacecraft oversaw the supply of power and positioning the satellite, housing several components such as the solar panels, the altitude control systems, the antennas and the communications system along with its computer. The science instrument collected light from the chosen target (using the mirror system), dispersed it (using the spectrograph and detectors system), and saved the data obtained (using the onboard computer).

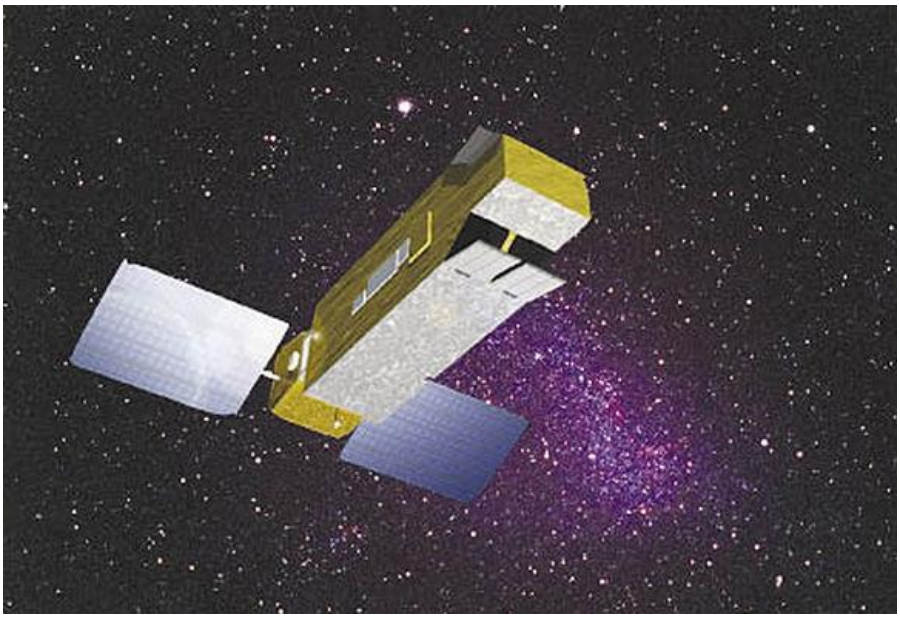

Figure 2.1: Rendering of the FUSE observatory

SOURCE Figure 2.1: : https://spinoff.nasa.gov/Spinoff2008/ct_1.html

The FUSE spectrograph is based on the Rowland circle design, and it has four different channels (or optical paths) that reflect the light to each of the four separate mirrors. The separate mirrors had to be co-aligned to make sure the light from the selected target illuminated adequately all four channels to maximize the throughput of the instrument, which had a spectral resolution of around 15 to 20 km/s. Two of the mirrors were coated with silicon carbide (SiC) that reflects better in shorter UV wavelengths (905 to 1110 Å), while the other two mirrors were coated with lithium fluoride over aluminum (LiF) that provides improved reflectivity in longer wavelengths (above 1000 Å). [11] [30]

The light from each of the four channels is then recorded in 2 different microchannel plate detectors, that have 2 separately functioning segments each (A and B) divided by a small gap. Since both detectors are illuminated with a SiC and LiF spectra, FUSE has in fact 8 segments. To put it in another way, this arrangement consists in the existence of 4 optical channels (SiC 1, SiC 2, LiF 1 and LiF 2) and 4 detectors segments (1A, 1B, 2A and 2B) that in turn results in having 8 different channel combinations: SiC 1A, SiC 1B, SiC 2A, SiC 2B, LiF 1A, LiF 1B, LiF 2A and LiF 2B. This was an advantage in the FUSE design since all observed absorption lines were covered by 2 or even 4 different channels, depending on whether is lies in the wavelength ranges 900 to 1000 Å or 1080 to 1180 Å (2 channels) or from 1000 to 1080 Å (4 channels). Also, because the detectors allowed multiple wavelength observations to happen at the same time, this made FUSE especially more sensitive than any FUV space observatory before it. [8] [11]

Nevertheless, before the light reached the detector it had first to be dispersed into a spectrum by gratings, 1 for each mirror. In this case, the gratings were actually curved instead of flat and very large, in which a large number of fine “parallel” grooves were etched that dispersed FUV light into a spectrum for further analysis. This characteristic was what gave the spectrograph such high resolving power and, thus, the ability to see details.

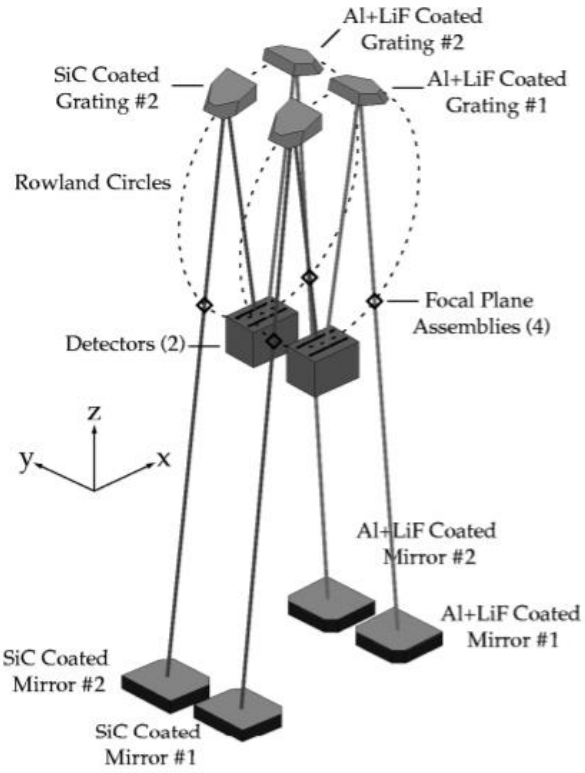


Figure 2.2: Schematics of the design of the FUSE's optical system

It can also be referred that FUSE had 3 distinct apertures varying in size:

- the small HIRS (4,0x20"), which provided maximum spectral resolution and minimum sky background but risked total loss from 1 or more channels due to thermal induced mirror motions;
- the medium MDRS (1,21x20"), which had a stable mirror alignment and ensured maximum throughput and spectral resolution on par with HIRS, but was more susceptible to airglow contamination;
- the large LWRS (30x30"), which was the least sensitive to alignment problems but also the one with the most sky background contamination issues, that could be mostly corrected by the pipeline depending on the data collection mode. [12] [31]

Finally, data from FUSE could be obtained in 2 different modes: the tag time or photon address mode (TTAG), useful on low counting rates (up to 2500 cps) where the x-y address of each photon and its pulse height are recorded along with a time marker (1/s with an accuracy of 8 ms) inserted in the data; and the spectral figure mode (HIST) suited for higher counting rates where partial data loss could happen due to data not being transferred fast enough from the detector. In HIST mode, the figure is integrated over an exposure and the data is stored as a histogram without pulse height and arrival time data. [14] [31]

SOURCE Figure 2.2: [14]

### 2.1.2. FUSE – Data processing and factors affecting data quality

After the data from FUSE was dumped each time the satellite passed the ground station in Puerto Rico, which amounted to 6 to 8 times per day, it was transferred to the satellite control center at JHU and verified for duplicates or missing packets. Once checked, the data was converted to processable formats by the automated processing system OPUS, and passed onto the pipeline that processes the data from FUSE, CalFUSE. In turn, CalFUSE screens the data to search for low quality and questionable data, corrects instrumental effects added in each step when possible, and executes corrections such as:

- thermal drift correction, caused by misalignment of individual channels in-orbit due to thermal effects,
- dead time correction, necessary due to a time lag where the detector isn't counting events despite there being radiation reaching it because it is still busy processing earlier data or being momentarily saturated,
- wavelength calibration, since wavelength drifts slightly due to time and environmental effects,
- background subtraction among others. [8] [11] [31]

It should be noted that all the data used on this work was calibrated using the most recent version of the CalFUSE pipeline available in the MAST archive at Space Telescope Science Institute (STScI).

There are instrument artifacts that need to be taken into account when analyzing FUSE data. These artifacts may originate on the instrument like astigmatism distortions (large Y height) which are a consequence of the optical design of FUSE. Another issue is the spectral motion due to grating motions, where small thermal variations are induced on the gratings, shifting the figure up to 15 pixels depending on the timescale (for example in a SiC channel by being exposed to direct sunlight on and off); or mirror motions, when the mirror experiences small thermal variations. These could lead to small misalignments between the channels, which manifest themselves as small offsets of the wavelength scale between the different channels.

Other artifacts can originate on the detector itself like Moiré patterns (strong fixed pattern noise in HIST spectra of bright targets), dead zones (opaque spots on the detector figure), grid wires (which can produce shadows on the detectors that attenuate up to 50% of the incident flux and varies with wavelength), gain sag (caused by prolonged exposure to photons that eventually make the detectors less efficient) and fixed patterned noise. The last one is especially important since it is a systematic effect and was detected in all the data analyzed in this work. This systematic effect is described in more detail below.

### 2.1.3. FUSE – Systematic effects and noise

The importance of systematics effects lies in their contribution to uncertainties calculated or estimated for any measurements and derived values. In this subchapter, only the most common systematic effects observed will be mentioned and any necessary extra comments will be made later while discussing the data in question.

The first, and most obvious effect, is the fixed-pattern noise, a noise that is in a fixed position spatially and results from non-uniformity between pixels. It manifests itself as distortions in the shape of the spectral profiles and can modify the apparent strength of the observed absorption lines or make them harder to identify. One way to deal with this is to combine data from different exposures, identify which ones have less fixed-pattern noise, when compared to ever-present statistical noise, and exclude bad fits while co—adding the best. This averages out the noise, though it can never be completely erased, and results in a higher signal-to-noise spectrum. Nonetheless, this cannot be corrected using the CalFUSE pipeline and must be done by the user. [11]

The second is the presence of airglow, which is the result of the excitation of components of the upper atmosphere of our planet that ultimately shows up on the target's spectrum. This effect could not be prevented since the instrument did not have a shutter. Airglow is always stronger during orbital day than during orbital night (see figure 2.3 below). Also, the severity of airglow contamination will depend other factors such as of the size of the aperture, the alignment of the satellite with the Earth's atmosphere and the phase of the solar cycle. Prominent affected absorption lines include H I (949 Å, 972 Å and 1025 Å), O I (988 Å, 990 Å, 1025 Å and 1039 Å) and N I (1083-1085 Å triplet and 1134 Å triplet). [30]

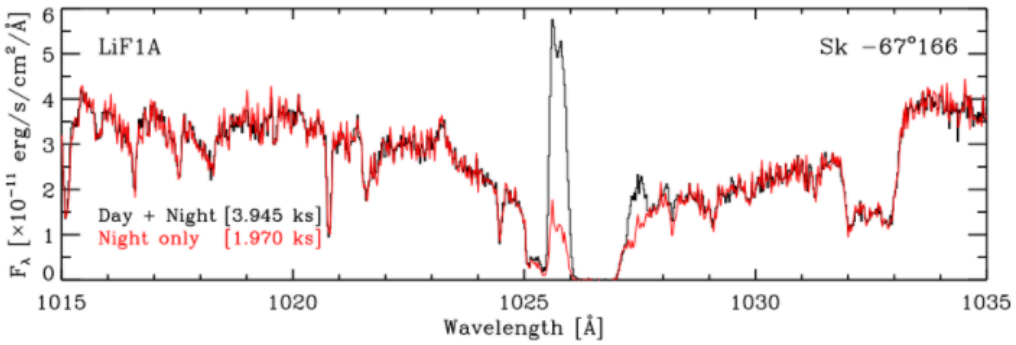


Figure 2.3: Spectra of an O4 supergiant in the Large Magellanic Cloud – difference of airglow contamination can be seen between spectra taken during orbital day + night (black line) vs. orbital night only (red line), especially in the H I 1025 Å region.

Finally, another problem faced when analyzing the data is the ability to resolve different components along the line of sight. In other words, an absorption line might have more than 1 absorption component from the same element but due to the resolution of the instrument, one might not be able to detect or resolve the different components. This will be discussed in more detail in section 2.3.

SOURCE Figure 2.3: [30]

## 2.2. Hubble Space Telescope (HST) – Space Telescope Imaging Spectrograph

### 2.2.1. Overview of the Space Telescope Imaging Spectrograph (STIS)

The Space Telescope Imaging Spectrograph (STIS) is a second-generation spectrograph, still in use on the Hubble Space Telescope, that substituted the 2 original HST spectrographs (GHRS and FOS). STIS was built by the Ball Aerospace Corporation for the Goddard Space Center, and was installed on HST in 1997. It is actually a 2,4 m long reflecting telescope and is orbiting at 600 km. Its primary mission is to obtain a "fingerprint" (temperature, density, motion, and chemical composition) of the observed target such as planets, stars, black holes, galaxies, the ISM among others. [33]

STIS is essentially a general-purpose spectrograph, possessing both imaging and spectrographic capabilities, via 3 two-dimensional detectors (2 MAMAs and 1 CCD) that operate on a large wavelength range, from near infra-red to the UV, providing throughout a high quantum efficiency and good dynamic range. It saves a time integrated figure on a data taking mode called ACCUM, very similar to the FUSE's HIST mode, although it also supports a mode similar to FUSE's TTAG. The STIS CCD records light from the visible to the infra-red portions of spectrum.

Besides the CCD, STIS also has 2 photon-counting multimode microchannel array (MAMA) detectors, that cover from the UV region to the visible. These detectors are very sensitive and, thus, have performance and safety brightness limits to avoid damaging the detector or compromising the data, since at high illumination count rates become nonlinear. To avoid this, bright object checks are obligatory prior to any observations. Also, the detector can record their data on ACCUM mode or TIME-TAG mode (similar to FUSE's TTAG mode). [32] [33]

When it comes to optical system, the complex design had its base on the following properties: enhancing throughput of the reflective optical system by canceling all unnecessary reflections, especially in the UV; correcting HST aberrations at the entrance of the spectrometer by having in-flight adjustments capabilities (which assured the figures would be clear and sharp); and installing redundant modes of operation to mitigate possible data loss in case 1 or more detector malfunctioned.

The assembly of the optical system itself consists of 2 subassemblies. The first is a two-element reflecting corrector to eliminate spherical aberration originated by the primary mirror manufacture error, while the second is an imaging spectrograph composed of: a corrector, whose function is to correct the telescope's off-axis astigmatism and spherical aberrations via a two-mirror system, the gratings and the camera equipment responsible for the telescopes high quality spectroscopy and imaging capabilities. [33]

When it comes to the gratings, there are actually 16 diffraction gratings, 12 first-order and 4 echelle gratings, that support 12 out of the 13 available spectral modes. For the data used on this thesis it is of special interest the echelle gratings, which have a high spectral resolution between 30 000 and 100 000 (much superior to FUSE) and encompass a large wavelength range from 1150 to 3100 Å. These gratings work by dispersing light pertaining to each order perpendicular to the dispersion direction, in orders that span a few Å, which allows to a considerable wavelength range to be covered in a single observation. The light dispersed by the gratings is then recorded by the MAMA detectors mentioned above. Another advantage of the echelle gratings is that neighboring echelles orders have wavelength ranges that overlap by around 10% at the edges. This means that lines identified at the beginning of the spectrum of one echelle order will also be seen at the end of the spectrum of the other echelle order, which helps to ensure that possible lines at the edges of the spectra are not compromised or missed. [11]

Finally, after the data is collected from the ground station it is processed by the CalSTIS calibration pipeline and goes through a process very similar to that of the FUSE data described above., The data used in this work were obtained from the MAST archive and were calibrated using the most recent version of the CalSTIS pipeline at the time the data were retrieved. It can also be added, that the data used in this work were obtained either with the E140M echelle grating, (which has a resolving power of 45 800 and spans from 1140 Å to 1735 Å), or the E230H grating (which has a resolving power of 114 000 and spans from 1620 Å to 3150 Å). [11] [32]

It should also be noted that some of the comments made regarding systematic effects and noise from FUSE can be applied to STIS data as well (such as airglow juxtaposition and fixed pattern noise). In the particular case of airglow, because the apertures used to obtain the data used in this work are small (0.2"x0.2") the effect of airglow on STIS data is much smaller than that on FUSE data.

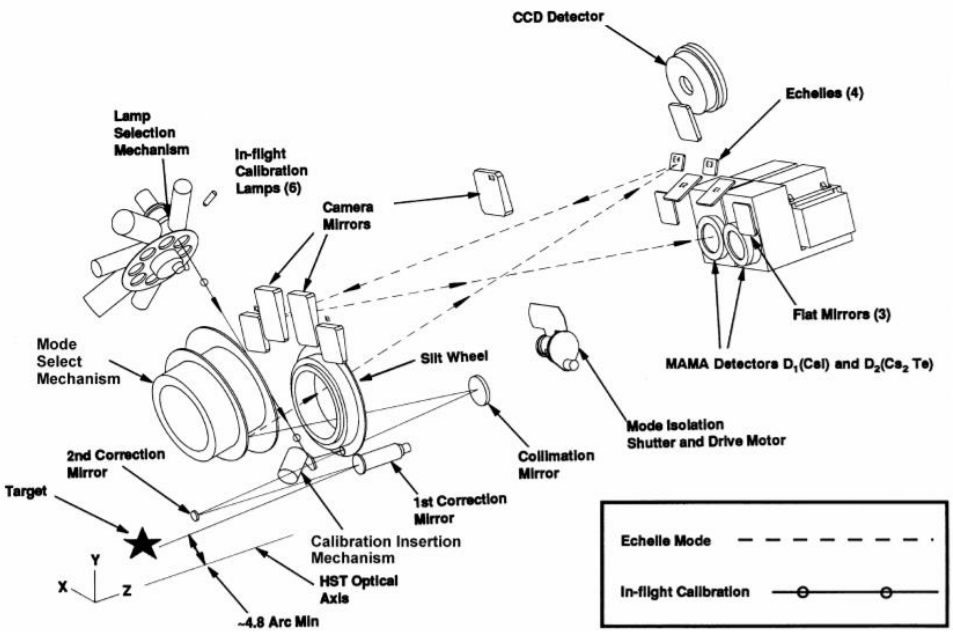


Figure 2.4: The STIS complex optical design includes corrective optics, a focal plane slit wheel assembly, fixed optics, collimating optics, a grating selection mechanism, focal plane detectors and an independent calibration lamp assembly

### 2.2.2. Overview of the Goddard High Resolution Spectrograph (GHRS)

The GHRSS was one of the 4 original axil instruments on board Hubble observatory and had as its principal mission to detect UV coming from celestial objects, remining active for 7 years (until 1997) until being replaced by STIS. It observed a wavelength band pass from 1150 to 2300 Å. Like STIS, the GHRSS divided light into its different spectral components, so that trough analysis and posterior processing important physical quantities could be measured such as temperature, composition, motion and others. It also had 3 resolution modes: low resolution, from 0,6 Å to 1200 Å; medium resolution, from 0,06 Å to 1200 Å; and high resolution, from 0,012 to 1300 Å.

The reason why GHRS will not be introduced with such detail is due to only have been used briefly to compare data measures from STIS and not actually been one of the main sources of data. [3] [4]

SOURCE Figure 2.4: [33]

## 2.3. Analysis methodology and Physical concepts

One of the ways to obtain information about a distant celestial target is to analyze the characteristics of the light it emits or reflects, which is the purpose of the spectrographs discussed earlier. However, the data obtained can be processed and analyzed in different ways. In this work, the aim was to analyze the spectra of selected white dwarf targets, identify and measure absorption lines (non stellar) to then derive abundances, and try to understand whether the absorption lines seen were due to pollution from the ISM onto the white dwarfs' atmosphere or if they were instead of circumstellar or interstellar nature. To measure abundances, 2 techniques were used: equivalent width measurement and apparent optical depth technique. Their physical concepts are explained in this subchapter along with the characteristics, advantages and disadvantages of the aforementioned methodology.

### 2.3.1. Opacity and optical depth

The first physical concept necessary to understand before actually discussing the techniques used is that of opacity. The light beam emitted from a star or reflected by another celestial body does not reach the observer without having lost some of its intensity, either by some of the photons being absorbed by atoms, ions or molecules in the gas of, for example, the ISM, or by being scattered. This incremental light extinction of the intensity ($dI_\lambda$) over an infinitesimal distance (ds) can be expressed as:

$$dI_\lambda = -k_\lambda \rho I_\lambda ds \quad (2.1)\ [18]$$

Where, $\rho$ is the density of the gas the light travels through (in g cm$^{-3}$), $ds$ the infinitesimal distance travelled (cm) and $k_\lambda$ the absorption coefficient or opacity (cm$^2$g$^{-1}$).

Secondly, there's another distance that can be defined which is the optical depth (or thickness), meaning the level of transparency of the medium being travelled by the light and, of course, is dependent on the absorption coefficient and, thus, on the wavelength:

$$\tau_\lambda = \int_0^s k_\lambda \, \rho \, ds \quad (2.2)\ [18]$$

where the product of the absorption coefficient, $k_\lambda$, with the density of the gas, $\rho$, can be translated as the fraction of photons of the light beam scattered per cm of gas crossed. In fact, eq 2.2 can be rewritten in function of the photons mean free path $\mu$ since:

$$\mu = \frac{1}{k_\lambda \rho} = \frac{1}{\sigma_\lambda n} \quad (2.3)\ [18]$$

where $\sigma_\lambda$ is the interaction cross-section (cm$^2$) and $n$ the volume density of particles (cm$^{-3}$).

$$\tau_\lambda = \int_0^s k_\lambda \, \rho \, ds = \int_0^s n\sigma_\lambda \, ds \quad (2.4)\ [18]$$

It is to be noted that $k_\lambda$, $\rho$ and $\tau_\lambda$ are all function of wavelength. This is the reason why looking at the same part of space using instruments sensitive to different wavelengths or different filters produces different Figures, since the gas in that part may be opaque to certain wavelengths but not others, like the example in Figure 2.5.

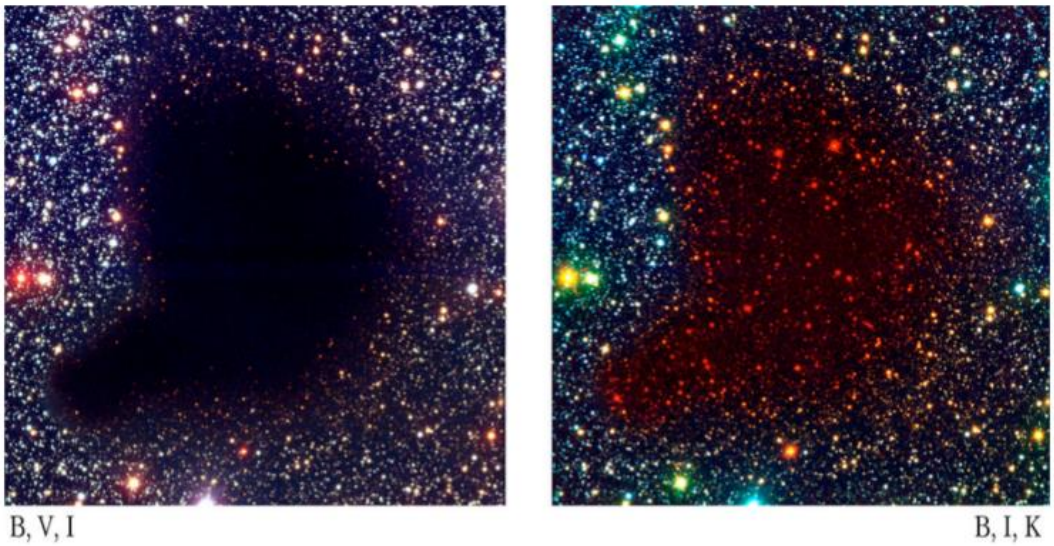


Figure 2.5: ESO Figures of the Dark Cloud Barnard 68 seen through different filters – at the left is the visible light (left) and near infrared (right) – There is a dust cloud that scatters particularly well visible light, thus blocking the light from stars behind the cloud. The dust cloud absorbs and re-emits the near-infrared light from the stars behind the cloud and they become "visible"

Gas with values of $\tau_\lambda$ superior to 1 is considered optically thick, whereas gas with $\tau_\lambda$ lower than 1 is considered optically thin (in an extreme case if $\tau_\lambda$ were to be zero then $I_o = I_\lambda$ which would mean that the beam that reached the observer would be the same as the one that left the star).

Finally, by taking equation 2.1 and integrating it according to eq 2.2, one obtains the intensity of the beam that should reach the observer:

$I_\lambda = I_{\lambda,0} e^{-\tau_\lambda}$ (2.5) [18]

Where $I_{\lambda,o}$ is the value of intensity that should be measured if there was no absorption or scattering of the light. [18]

SOURCE Figure 2.5: [18]

### 2.3.2.Equivalent width measurement and line strengths

The analysis starts by plotting the intensity of a star's spectrum versus its wavelength so that the absorption lines can be detected and their shape (or line profile) studied. Figure 2.6 shows the example of an ideal absorption line and 2 different areas that can easily be discerned – the core and the wings. [12]

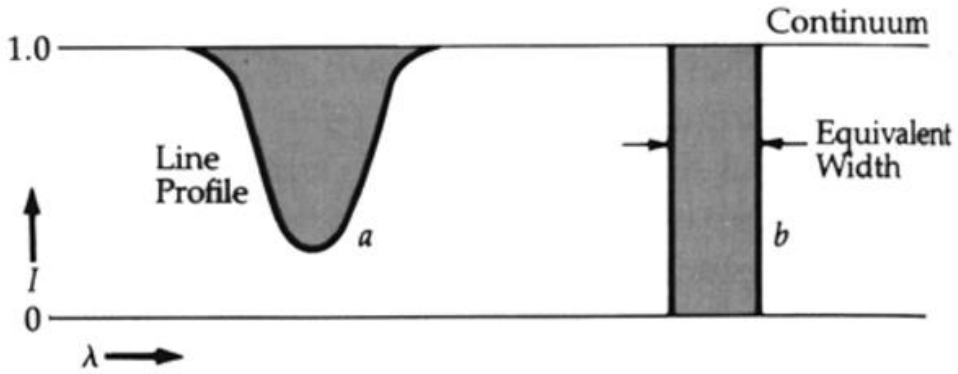


Figure 2.6: Diagram representing the equivalent width of an absorption line (area covered the blue rectangle) along with the star's spectrum line main details

Different types of information can be derived from the line profile, for example, if a star is rotating, the portion of light from the incoming side will be a bit blue shifted, while the light from the receding side will be faintly redshifted, which will result in a particular broadening of the line and, from that, its rotation period can be inferred.

The equivalent width of an absorption line $W_\lambda$ is the width of the rectangle in figure 2.6 that has an area equal to that of the absorption line, in relation to the continuum in that region after the spectra has been normalized. The equivalent width corresponds to the equal value of the energy that would be removed from the line for its intensity to become zero. This area can be expressed as an integral that depends on the intensity of the line and its wavelength, as expected:

$$W_\lambda = \int_{-\infty}^{\infty} \frac{I_{\lambda,0} - I_\lambda}{I_{\lambda,0}} = \int_{-\infty}^{\infty} (1 - e^{-\tau_\lambda}) d\lambda \quad (2.6)\ [18]$$

where, $I_o$ is the intensity of the continuous radiation source while $I_\lambda$ is the intensity emitted from that strip of light alone.

SOURCE Figure 2.6: http://ircamera.as.arizona.edu/astr_250/images/eq_width.gif

Furthermore, the equivalent width measurement allows for comparison between line strengths and is dependent on the quantity of atoms that are present on the line of sight as well on the strength of the particular transition observed. Also, for a certain temperature, the more atoms there are, the broader and stronger the line will be. As it can be seen in the figure below, there are 4 lines with different profiles but with the same value of equivalent width. This shows that judging a line's strength by its shape can be deceptive and can lead to incorrect results. [18]

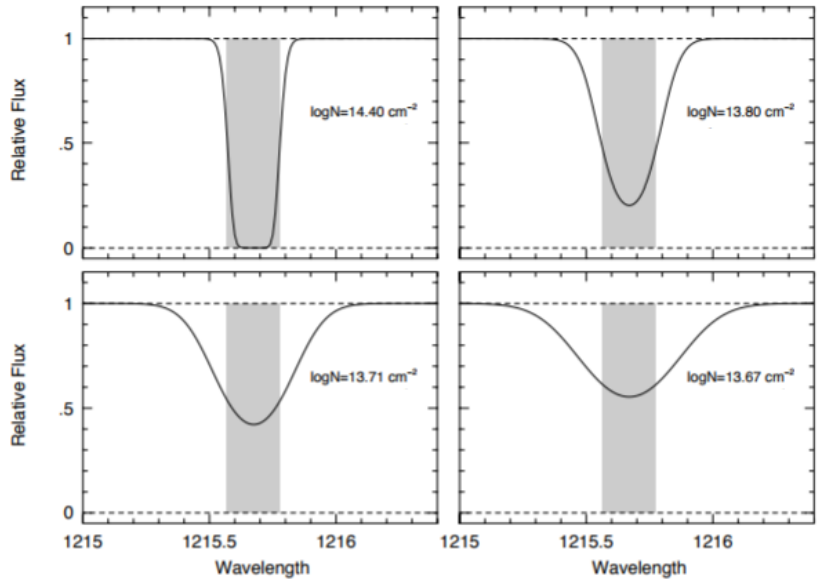


Figure 2.7: Profile of 4 absorption lines with the same equivalent width but different line profiles (N is column density or number of atoms per cm² – discussed in 2.3.4)

SOURCE Figure 2.7: [18]

### 2.3.3. Line broadening processes and line profiles

There is always a possibility that the wavelength of the photon absorbed by the gas might vary between $\lambda$ and $\lambda+d\lambda$. The broadening function $\varphi_\lambda$ and the probability of this type of event occurring $\varphi_\lambda d\lambda$ are defined so that when an absorption does happen in the line:

$$\int_{-\infty}^{\infty} \phi_\lambda d\lambda = 1 \quad (2.7)\ [18]$$

The value of the broadening function will be bigger near the center of the line ($\lambda_o$) and will diminish quickly as it drifts to shorter or longer wavelengths than $\lambda_o$.

Moreover, the cross-section for absorption $\sigma_\lambda$ will also be dependent on the broadening function $\phi_\lambda$:

$$\sigma_\lambda = \sigma_0 \phi_\lambda \quad (2.8)\ [18]$$

where $\sigma_o$ will include the transitions atomic parameters:

$$\sigma_0 = \frac{\lambda^4}{8\pi c}\frac{g_u}{g_l} a_{ul} \quad (2.9)\ [18]$$

where $a_{ul}$ is the transition probability, $g_u$ and $g_l$ the statistical weights of the upper and lower electronic energy levels, and the other symbols maintain their respective common meaning.

The reason why this is important is because it is in the atmosphere of the stars there are few physical processes that can and do indeed broaden the absorption lines, from which the main are: doppler broadening, due to motions of the absorbers caused by thermal variations; and natural broadening or pressure broadening that takes place in the star's atmosphere where the electronic energy levels can be affected by an ion's electric field or collisions with neutral atoms. [18]

These processes will lead to there being 2 distinct line profile shapes:

- The Doppler profile, known also as thermal broadening, is gaussian shaped and dominates formation of line cores.
- The Lorentzian profile, known also as pressure broadening, dominates the wings of the lines.

In turn, these two different line profiles can be combined into one called the Voigt profile. It can accurately model a number of spectral features but for spectral analysis the gaussian profile usually provides already good enough accuracy since the lines of interest are generally very weak or saturated, which makes the Lorentzian contribution nearly irrelevant.

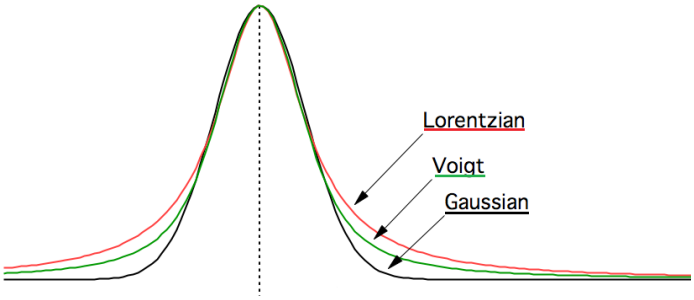


Figure 2.8: Diagram comparing the Doppler, Lorentzian and Voigt profiles

This difference in profile shapes can be observed when comparing stellar lines and non-stellar absorption lines. The light as it comes from the star reveals broad lines, yet when it passes through an interstellar dust cloud part of light will be absorbed, which in turn will originate narrower absorption lines, as it can be seen in image 2.9. However, it should be noted this is not the only way we distinguish them. By plotting the spectrum in velocity-space we can tell at the velocity of the medium that originated them, as it will be further discussed in chapter 3.

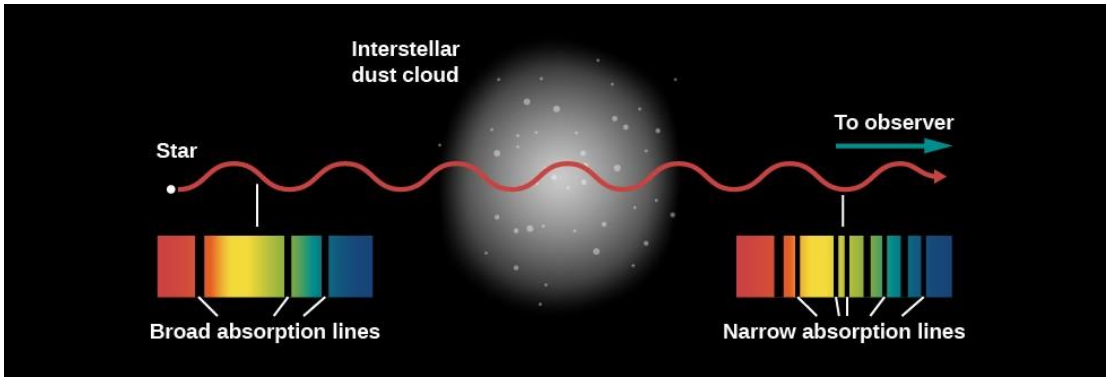


Figure 2.9: Diagram showing what happens to light after it passes through an interstellar dust cloud

SOURCE Figure 2.8: adapted from https://www.wavemetrics.com/products/igorpro/dataanalysis/peakanalysis/multipeakfittingpix/mpf2peaktypesgraph.png

SOURCE Figure 2.9: https://s3-us-west-2.amazonaws.com/courses-images/wp-content/uploads/sites/1095/2016/11/03160514/OSC_Astro_20_02_Spectrum.jpg

### 2.3.4. The curve of growth and column density

The curve of growth (COG) is an analysis technique done for a single species that measure equivalent width of different transitions with different oscillator strengths (f), a dimensionless quantity that translates the probability of absorption of radiation consequence of transition between energy levels. In this thesis, this technique was not used but it is still important to introduce its concept in order to understand the conditions we assumed to be working in.

The curve of growth, as it can be seen in figure 2.10, has essentially 3 regimes:

- The linear portion, where $N\lambda f$ is proportional to $W_\lambda/\lambda$ and as you move to the right, both are increasing.
- The flat part, where regardless of how much N you add, $W_\lambda$ is not going to change. This is just a consequence of the regime where you start with very optically thin lines that then become optically thick and has nothing to do instrument.
- The square root part, which happens when a point is reached where so much material has been put in that the line starts to develop dampening wings and Lorentzian profile starts to dominate.

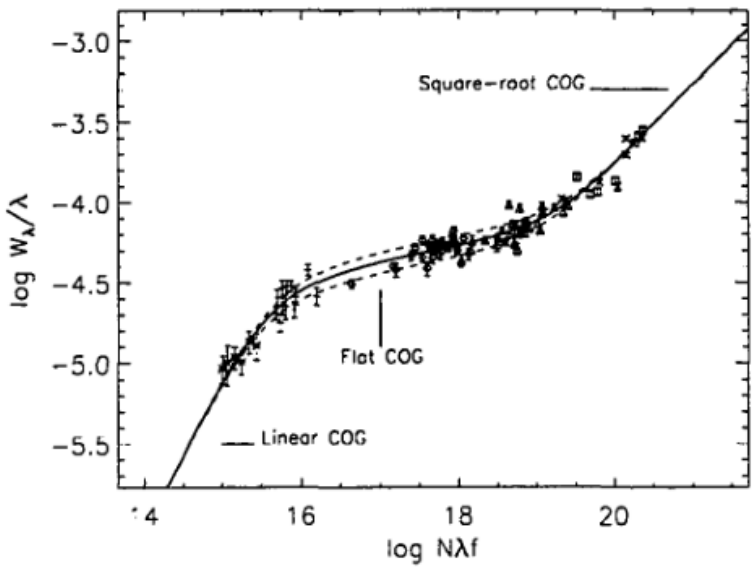


Figure 2.10: Example of a curve of growth for molecular hydrogen

An example of the difference in profile shape of the absorption line depending on the regime the transition is in can be seen in the figure below.

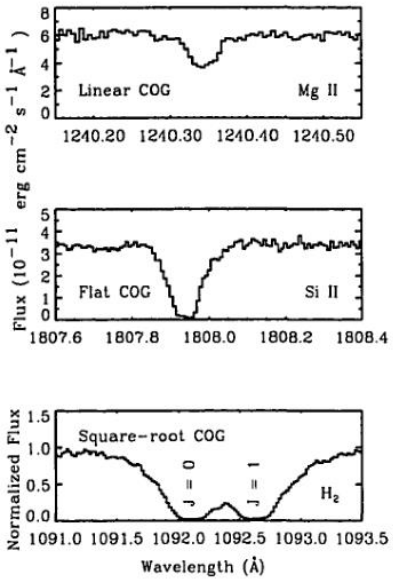


Figure 2.11: Difference in absorption line profile depending on the part of the COG they are in

It can be said that in the linear part of the COG the line reveals a Gaussian profile whereas in the square-root portion it shows dampening wings, making the line's profile Lorentzian. Also, for the line pertaining to the flat part of the COG we can see it is saturated as it reaches zero flux and appears to be slightly broaden.

Now we can finally introduce the concept of column density (N), which is the amount of material (atoms, molecules, etc) observed along a line of sight. What was just discussed is important in understanding the regime we worked in and how N was calculated. By taking into consideration that when the absorption lines are weak enough the gas is considered to be optically thin, then the equivalent width can be considered a sensitive measure of N. This means we will be in the linear COG regime and the intrinsic line profile will be Gaussian.

To further explain in more detail, an absorption system, or a cloud, is a random gas structure that can be described by the number of atoms, ions or molecules that occupy its volume, meaning its density will be a function of position within the cloud: $n(\mathrm{cm}^{-3}) = n(x,y,z)$. Thus, when observing a star's sight line, the observable distance covered will be finite and each infinitesimal location along the line of sight dependent in its position: $s = s(x,y,z)$. In turn, the quantity of the gas density sampled will be a function of $s$, and consequently, of $xyz$. Therefore, the column density ($N$) can be defined as the integral of the density along the line of sight.

$N = \int_0^s n ds, \quad$ (2.10) [18]

where *n* is the volume density of particles ($cm^{-3}$) and *ds* the infinitesimal distance travelled along the line of sight (cm).

In fact, since column density is the quantity aimed to be measured when determining the equivalent width of a line, in order to calculate N (for the linear regime of the COG) one begins by integrating equation 2.6. Knowing that the gas is considered to be optically thin ($\tau_\lambda$ <<1) in this regime, as it was mentioned earlier, and the line profile is Gaussian, then the approximation $e^{-x} \cong 1 - x$ when x<<1 is valid.

By substituting eq 2.7 and 2.8. into 2.6, the last can be rewritten as:

$W_\lambda = \int_{-\infty}^{\infty} \tau_\lambda d\lambda = N\sigma_0 \quad \int_{-\infty}^{\infty} \quad \phi_\lambda d\lambda = N\sigma_0 \quad$ (2.11)

This equation translates the relationship known as the linear part of the Curve of Growth that describes how $W_\lambda$ grows with the increase of N, as it can be seen in figure 2.10. As a note, it can be added that for this work only the linear part is of relevant interest and so it was the one for which the expression was derived (equation 2.11). The other parts, "the flat part" and the "the square root part" are not directly relevant to the data analyzed and therefore won't be discussed further. [18]

Finally, picking up from equation 2.11, by substituting the value of $\sigma_0$ by equation 2.9 and knowing that

$\lambda g_l f = \frac{m_e c \lambda^3}{8\pi^2 e^2} g_k a_{kl} \quad$ (2.12) [18]

, where f is the oscillator strength of the transition in question (that can be retrieved from compilations of atomic data), the expression for the column density N is derived:

$N\ (cm^{-2}) = 1{,}13 \times 10^{20} \frac{W_\lambda\ (\text{Å})}{f\ \lambda^2 (\text{Å})} \quad$ (2.13) [18]

In addition, for the gaussian profile, the optical depth can be approximated and written in function of N(λ) as well:

$\tau(\lambda) = \frac{\pi e^2}{m_e c^2} f \lambda^2 N(\lambda) \quad$ (2.14) [18]

SOURCE Figure 2.10 and 2.11: [11]

### 2.3.5.Apparent optical depth technique

The apparent optical depth technique (AOD) is a method developed to analyze interstellar absorption lines and derive column densities while at the same time determining whether there are unresolved or saturated structures in the spectrum that might affect the column density measurement. This technique first appeared as a quicker but reliable alternative to a technique where careful analysis of the growth curve was required. One of its main advantages is that it is not necessary to have prior knowledge of the component structure. Nonetheless, this technique can only be used with data that has good enough S/N ratio, since for lower resolution data it will overestimate calculated values. [35] [36]

Continuing from what was discussed in section 2.3.1, where optical depth was defined, it is pertinent to now consider the apparent optical depth ($\tau_a$). When a line of sight is observed through an instrument with finite resolution, the apparent optical depth is the actual value being measured. For the AOD method to work properly, the instrumental resolution should be higher than the line width, so that the line studied is fully resolved and making $\tau_a$ a reasonable approximation to the true $\tau$ ($\tau_a \approx \tau$) is valid. The following expressions define the true optical depth (2.15) and the apparent optical depth (2.16):

$$\tau(\lambda) = ln\left[\frac{I_0(\lambda)}{I(\lambda)}\right] \quad (2.15)$$

$$\tau_a(\lambda) = ln\left[\frac{I_0(\lambda)}{I_{obv}(\lambda)}\right] \quad (2.16)$$

Where $I_o$ is the real intensity of the light and $I_{obs}$ is the intensity, after absorption, seen by the instrument.

Following from equation 2.15 one can express the optical depth in terms unit velocity as:

$$\tau(v) = \frac{\pi e^2}{m_e c^2} f\lambda \;\; N(v) = 2{,}654 \times 10^{-15} f\lambda \;\; N(v) \quad (2.17)$$

Where $\lambda$ is the wavelength of the absorption line (Å) and $N(v)$ is now given in atoms $cm^{-2}$ /(km $s^{-1}$) . [35]

Now taking eq. 2.17 and solving in function of $N(v)$ and by making appropriate substitutions and replacing the constants, the expression of the apparent columns density can be derived.

$$N_a(v) \;\; (cm^{-2}(km\, s^{-1}))^{-1} = \frac{3{,}768\times10^{14}}{f\lambda} \; ln\left[\frac{I_0(\lambda)}{I_{obv}(\lambda)}\right] dv \quad (2.18)\ [11]$$

The column density is then obtained by integrating eq. 2.18 over the velocity range defined by the absorption line. The plot resulting from this equation will have apparent column density per unit velocity ($N_a(v)$), allowing the user to directly infer physical conditions in the absorbing medium as a function of velocity. From this it is possible to better understand if the line has more than 1

component and if so, establish a minimum limit (2+ or 3+ components, for example) and get a sense of the relative velocity of each component. [11] [36]

The AOD technique can be used to assess and correct the level of saturation in the data as well, through comparison of the apparent column density value obtained from a stronger line (higher $f\lambda$, where f is the oscillator strength of the particular line considered) with another from a weaker line (lower $f\lambda$). A difference in $f\lambda$ values of around a factor of 2 is preferred so that saturation effects can be clearly perceived. In other words, if the $N_a$ value of the stronger line is significantly smaller than that of the weaker line, this a sign of the presence of unresolved saturation. Furthermore, when defining a $N_a$ value for a particular element the most reliable value is that of the weaker line, since there's less possibility of saturation taking place and, according to 2.16, the weaker the line the higher $N_a$ value obtained.[36]

Lastly, the error sources for this method come mostly from the fixed pattern noise in the detectors (fixed pattern noise effected can be mitigated by co-adding data obtained at different detector locations) and from the placement of the continuum (especially important in UV band and for weaker lines). In order for the continuum placement to be reliable it needs a relatively clean background source with a smooth continuum and reasonable S/N ratio. Also, the only downside of this method is that, while it can identify the existence of more than 1 absorption component in a line as discussed before, it cannot determine the column densities for each the absorption components independently. [35]

## 2.4.Analyzed targets and its characteristic

### 2.4.1. Characteristics of the white dwarfs

For this thesis 4 targets were chosen, all DA white dwarfs that had been previously observed in the FUV region of the spectrum with FUSE and some with STIS all well. For all of the targets in this work, there is some work in the literature where abundances have been determined for each line of sight and where circumstellar components have been detected. This allows us to compare our measurements with previous work. Some of the data analyzed in this work was not available yet at the time previous studies were published. In addition, previous studies focused mostly on high ionization species, while in this work both low and high ionization species were considered.

Table 1 summarizes the properties of the white dwarfs used in this study, while table 2 summarizes the FUSE and STIS observations used.

Table 1: Stellar properties

| Target name | Alternate name | Spectral Type [a] | *l* (deg) [a] | *b* (deg) [a] | $L/L_{sun}$ [c] | *d* (pc) [c] | V (mag) [a] | $T_{eff}$ (K) [b] | log *g* ($cm/s^{-2}$) [b] |
|---|---|---|---|---|---|---|---|---|---|
| WD 0232+035 | Feige 24 | DA | 82.05 | 5.49 | 5.86 | 78 | 12.41 | 60 487 ± 1 100 | 7.50 ± 0.06 |
| WD 0455-282 | REJ 0457-281 | DA | 52.50 | 10.20 | 1.85 | 108 | 13.92 | 50 960 ± 1 070 | 7.93 ± 0.08 |
| WD 1611-084 | REJ 1614-085 | DA | 4.30 | 29.30 | 0.43 | 86 | 13.43 | 38 840 ± 480 | 7.92 ± 0.07 |
| WD 2111+498 | GD 394 | DA | 91.37 | 1.13 | 0.45 | 57 | 13.09 | 39 290 ± 360 | 7.89 ± 0.05 |

Reference: [a] http://simbad.u-strasbg.fr/simbad/ , [b] Barstow et al. (2003), [c] Bannister et al (2003), and references therein

Table 2: LOG of FUSE and STIS Observations

| FUSE Observations | | | | | |
|---|---|---|---|---|---|
| Star | Program ID | Date | Exposure Time (ks) | Aperture | Mode |
| WD0232+035 | P1040503000 | 2/1/2004 | 16.12 | MDRS | HIST |
| | P1040504000 | 6/1/2004 | 12.00 | MDRS | HIST |
| WD0455-282 | P1041101000 | 3/2/2000 | 19.67 | MDRS | TTAG |
| | P1041102000 | 4/2/2000 | 10.12 | MDRS | TTAG |
| | P1041103000 | 7/2/2000 | 17.68 | MDRS | TTAG |
| WD1611-084 | B1190401000 | 2/4/2004 | 9.64 | LWRS | TTAG |
| WD2111+498 | M1010703000 | 11/10/1999 | 3.66 | LWRS | TTAG |
| | M1010704000 | 11/10/1999 | 5.65 | LWRS | HIST |
| | M1010706000 | 13/10/1999 | 4.69 | LWRS | HIST |
| | M1053201000 | 27/10/2007 | 4.40 | LWRS | TTAG |
| | M1053202000 | 4/9/2002 | 7.96 | LWRS | TTAG |
| | P1043601000 | 20/06/2000 | 28.31 | LWRS | TTAG |

STIS Observations

| Star | Program ID | Date | Exposure Time (ks) | Aperture | Grating/ Filter | Cenwave | Mode |
|---|---|---|---|---|---|---|---|
| WD0232+035 | O4G701010 | 4/1/1998 | 2.16 | 0.2X0.2 | E140M | 1425.000 | ACCUM |
| WD2111+498 | OCKM01010 | 25/08/2015 | 2.60 | 0.2X0.2 | E140M | 1425.000 | TIME-TAG |
| | OCKM02010 | 23/08/2015 | 2.60 | 0.2X0.2 | E140M | 1425.000 | TIME-TAG |
| | OCKM03010 | 24/08/2015 | 2.60 | 0.2X0.2 | E140M | 1425.000 | TIME-TAG |
| | OCKM04010 | 22/08/2015 | 2.60 | 0.2X0.2 | E140M | 1425.000 | TIME-TAG |
| | OCKM05010 | 21/08/2015 | 2.60 | 0.2X0.2 | E140M | 1425.000 | TIME-TAG |
| | OCKM06010 | 21/08/2016 | 2.60 | 0.2X0.2 | E140M | 1425.000 | TIME-TAG |
| | OCKM07010 | 20/08/2015 | 2.60 | 0.2X0.2 | E140M | 1425.000 | TIME-TAG |
| | OCKM08010 | 24/08/2015 | 2.60 | 0.2X0.2 | E140M | 1425.000 | TIME-TAG |
| | OCD854010 | 23/12/2013 | 1500.00 | 0.2X0.2 | E230H | 2713.000 | ACCUM |

Reference: https://archive.stsci.edu/xcorr.php

### 2.4.2. Measurement Procedures and IDL routines

This subchapter consists of a brief summary of the steps and IDL routines used to obtain the equivalent width and column density measurements, where focus is given to the main tasks accomplished per program used as well an introduction to its origin and main purpose. In other words, the following instructions outline the general steps taken in order to obtain the desired measurements. Smaller detail inputs and corrections have been left out in order to better understand the larger procedure and because they will change from file to file.

After the data has been retrieved from the MAST archive at Space Telescope Science Institute, the individual exposures for each observation were co-added to increase the signal-to-noise ratio of the final dataset use in the analysis, and then the following steps were executed:

1. Convert the files (either in .fit or .fits format) to ASCII (.dat format) using an IDL routine made for it (annex 1.1).
2. Use the existing IDL plotting procedure *xiplot.pro* (from source: http://www2.iap.fr/Fuse/outils.html) to plot flux versus wavelength of desired ASCII file. The installation of IDL Astron Library from GSFC is also necessary. (http://idlastro.gsfc.nasa.gov/homepage.html)
    a. Use the function "Find Lines" to put markers along the spectrum to aid in identifying possible absorption lines.
    b. Check carefully the existence of the line by searching for another of similar or higher strength ($f\lambda$) (used atomic data list containing vaccum wavelengths and oscillator strength, supplied by C. Oliveira, private communication). If this other line is not observed even though it falls in the wavelength range of the spectrum at hand then the line seen is either an unknown stellar line or an artifact, and should be disregarded.
    c. If an absorption line is detected take note of its wavelength and corresponding species.
3. Once all files have been analyzed, use an IDL routine that can read in the desired ASCII file and save each identified absorption line in a separate ASCII file (annex 1.2).
4. Use the spectrum analyzing procedure *imnorm.pro* (from K. Sembach, 1999) to perform the bulk of the measurements. Steps taken for each transition from each target are outlined here:
    a. Convert the original spectrum from wavelength (Å) vs flux to velocity (km/s) vs flux.
    b. Adapt the range of the spectrum so it will focus on the target absorption line, making sure enough continuum remains for the following fit.
    c. Mark an appropriate interval of the stellar continuum before and after the absorption line.
    d. Estimate the stellar continuum around the absorption line using a low order Legendre polynomial fit to the data.

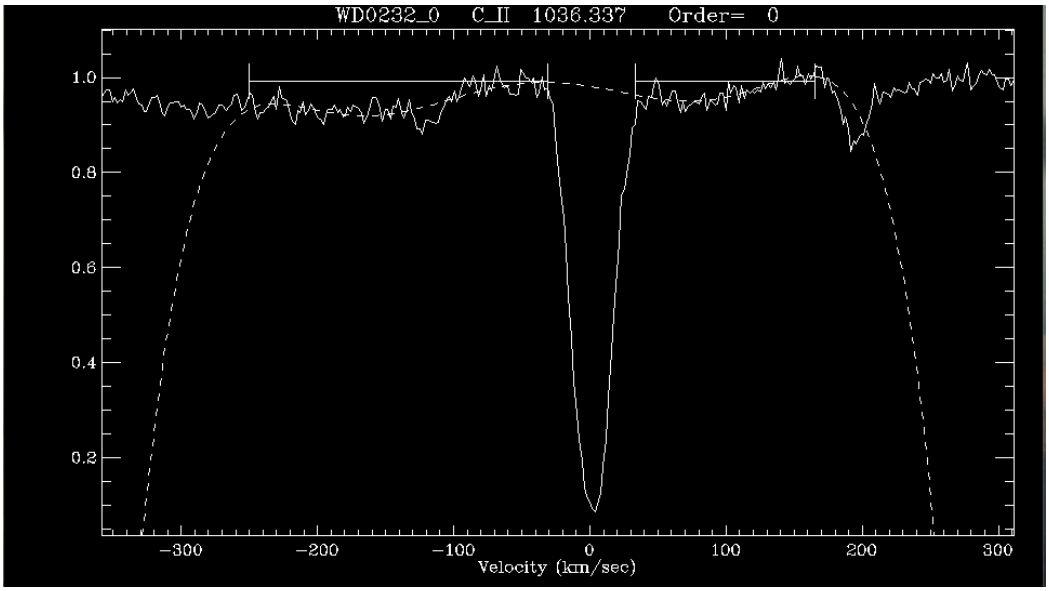


Figure 2.12: Continuum placement and its polynomial it

e. Convert the spectra back to wavelength space.
f. Enter equal width measurement mode and mark the area where the polynomial fit crosses the absorption line (at the beginning and the end) to define the area to be measured.
g. Choose to measure the absorption in fixed pattern noise mode. Take note of the equal width measurement values and its uncertainties.

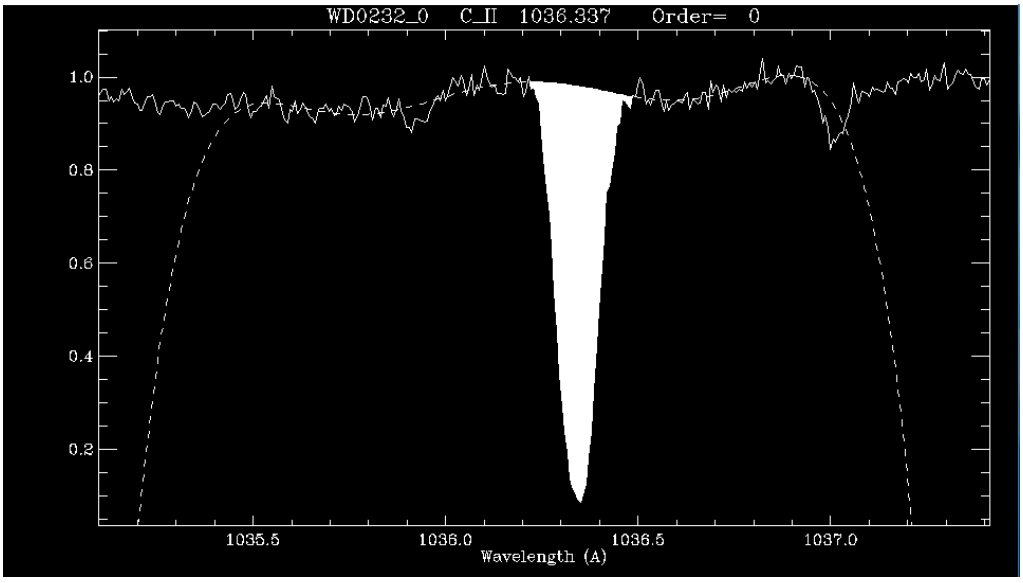


Figure 2.13: Equivalent width measurement

h. Convert spectra to velocity-space again.
i. Re-expand the spectrum to view the absorption line in column density mode. Pay special attention in augmenting the upper limit of the y-axis to values between 1e12 and 1e14 for the next step to work.
j. Enter column density mode and choose as limits the same values used to delimitate the equivalent width area that was measured.
k. Choose to enter the appropriate oscillator strength (*f*) value for the transition in question.
l. Choose again the same limits values used to delimitate the equivalent width area and in step j.
m. Choose to measure the column density in fixed patter noise mode. Take note of all column density values and its uncertainties.

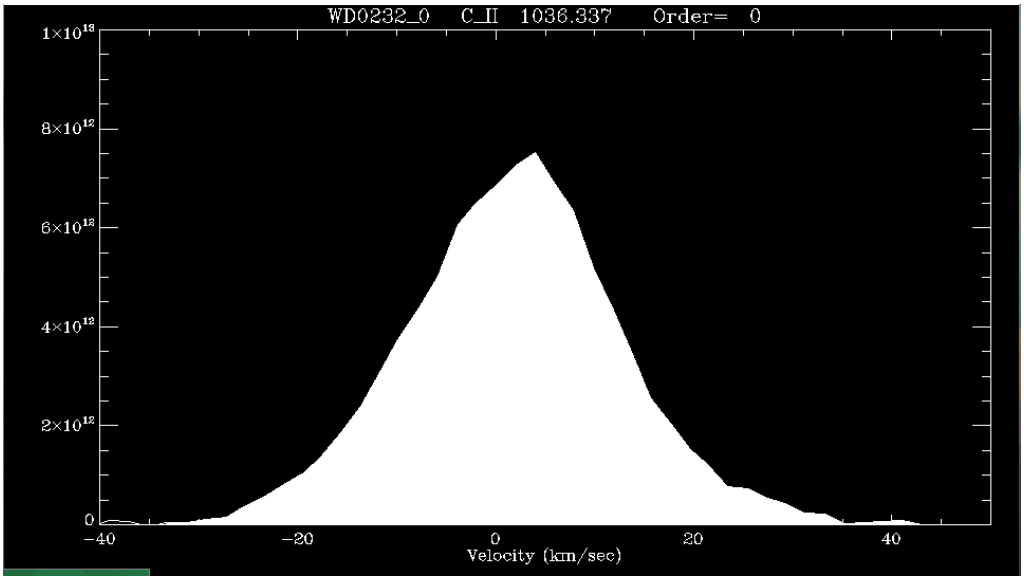


2.14: Columns density measurement

As a note, the main factors that will affect the uncertainties include: contributions from Poisson noise, high frequency fixed pattern noise that remains in the co-added data, the uncertainties regarding the appropriate choice of the continuum in step c, uncertainties in the Legendre fit parameters and uncertainties regarding the choice of the area to calculate the value of the equivalent width of the line. [11] [35]

# Chapter 3: Analysis of the White Dwarfs' Spectra and Determination of Abundancies

In this chapter are included the most important graphics and all the measurements obtained using the methodology presented in chapter 2. The graphics represent all relevant observed absorption lines and some stellar lines (identified by the ** marker before the line's species' name), in order to help differentiate one from the other. However, not all identified absorption lines were measured and its reasoning is explained case by case. It should also be noted that the results are given separately by target with the purpose of establishing pertinent comparisons between lines, whenever deemed necessary.

Furthermore, all the formulas or programs used to calculate uncertainties or other measurements are introduced when first necessary and thereafter are assumed to be the same.

When it comes to error sources, to apply what was said in chapter 2 to the measurements done in this chapter, it could be said that are two kinds of main error sources: errors associated with how the program will fit the continuum, that takes into account Poisson noise, fixed pattern noise (especially relevant in measurement of weak lines) and uncertainties during continuum placement, mainly deviations obtained during the calculation of the equivalent width that are then propagated to the determination the column density; and errors connected to whether there is saturation, meaning if there are unresolved components, which could lead to obtaining incorrect results. This is why it is always preferred to compare lines with different strengths. However, this is not always possible. To put it another way, much of this type of analysis is based on the assumption that the lines are not fully saturated, which is why when a particular line is very strong and looks saturated a lower limit of N is given instead.

In other words, the 2 the main resolution issues will be:

a) Blending: With the level of resolution from FUSE or STIS, blending between distinct species is not a common occurrence for ISM lines of sight. Still, when it happens, in order to ascertain whether the line in question is really blended, it must be then compared with a line of similar or higher strength that appears isolated and on an area with relative low noise. Nevertheless, for a few transitions like the 952 Å N I triplet and the 988 Å O I triplet it can at times be difficult to determine if it is a line or an effect. The results of this evaluation will change according to the target in question, the characteristics of that exposure and how many observations there are.

b) Saturation :This issue is particularly tricky since saturation effects can be hidden by the FWHM of the equipment by broadening the width of the absorption line. This will make a saturated line look like it is a normal unsaturated absorption line and lead to wrong estimation of values. In order, once again, to ascertain whether the line is saturated or not, it is important to watch out for abnormally or unexpectedly strong lines and search for others with similar strengths and compare their profiles. The measurements of values such as column density can also provide a valuable tool to ascertain saturation problems. [11]

## 3.1. Results for WD 0455-282

As it was referred in chapter 2.4 this star is a DA white dwarf, meaning, that it's atmosphere is rich in hydrogen. The graphics below represent the section of spectrum of the white dwarf observed with the FUSE observatory introduced in chapter 2 and according to table 2.

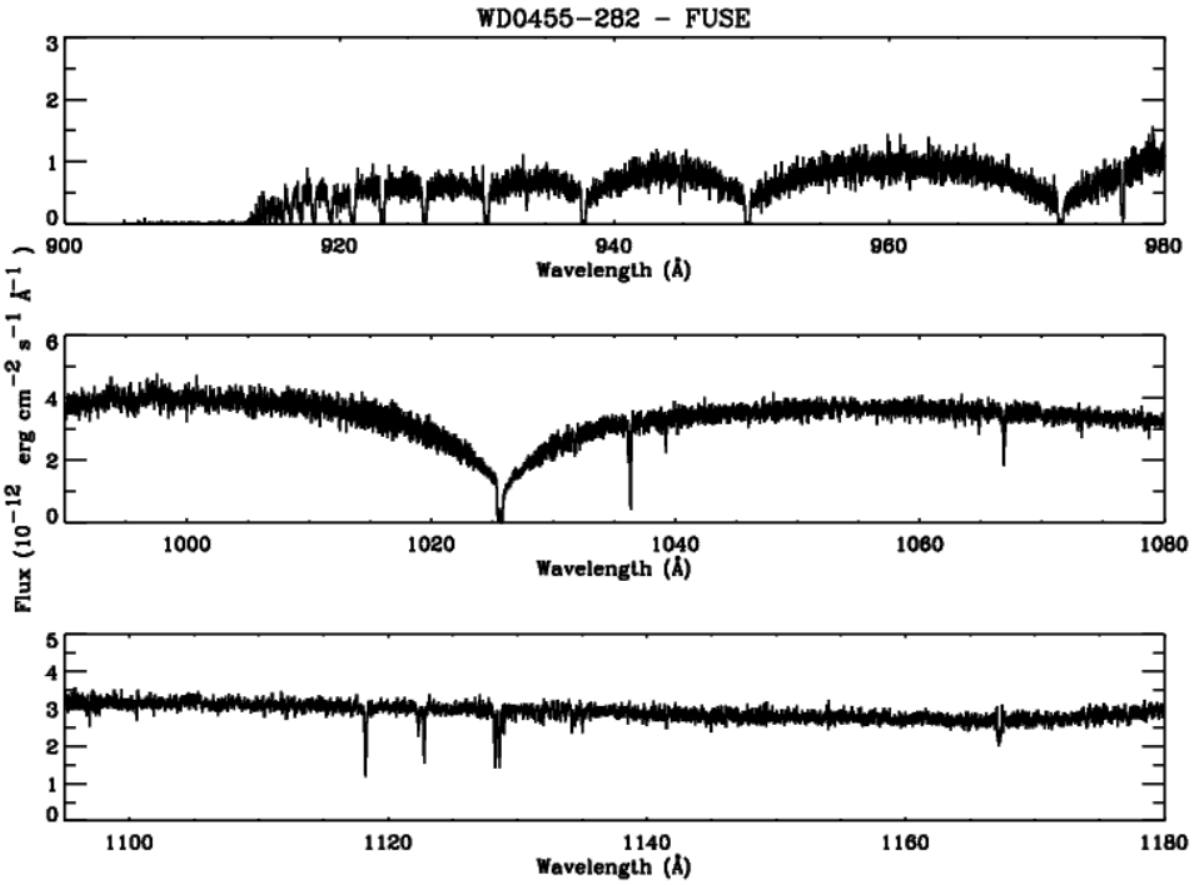


Figure 3.1.1 – FUSE spectra of WD 0455-282

The following graphics represent the normalized flux of each relevant absorption line plotted in velocity-space (km/s). The target name, species and transition are identified in the individual title of each graphic. All pertinent comments regarding each line are made after the graphics and are organized by species. Finally, the two vertical lines represent, respectively, the estimated velocity of the ISM (dashed line) and the velocity of the star's photosphere (dotted line). It should be noted that these lines are merely markers to help guide the eye and better understand the alignment of each line (given that different absorption lines come from different channels in the FUSE instrument and can suffer from small misalignments). These markers allow us to look at the kinematic structure of the different absorption lines and help us to evaluate if the line is of stellar or non-stellar origin. Estimations of the velocity values are made by observing all the spectra obtained for the target and comparing with already calculated values for the star using stellar models retrieved from source [9]. A full kinematic analysis of the component structure can only be performed using the profile fitting technique, which is beyond the scope of the current work.

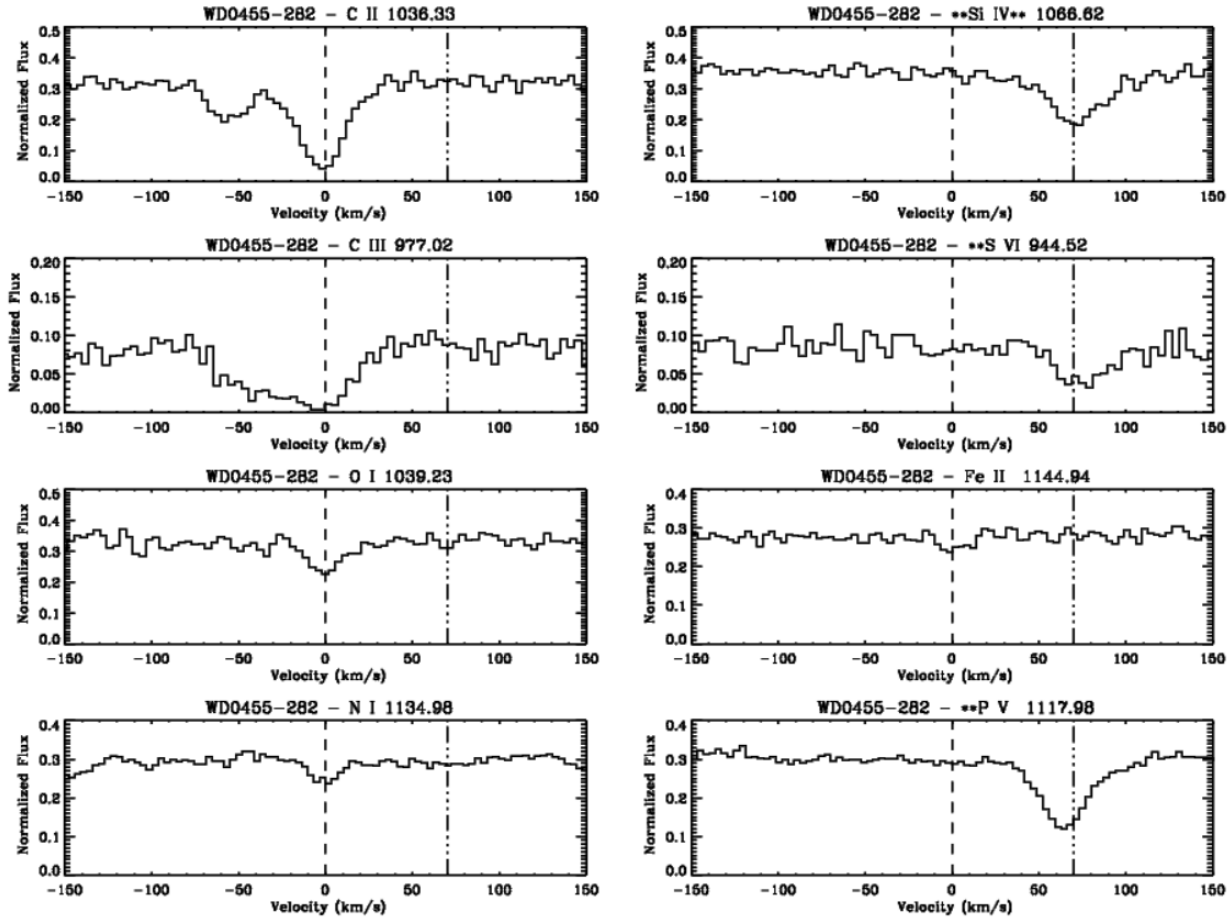


Figure 3.1.2: Relevant absorption lines identified in the FUSE spectrum of white dwarf WD 0455-282 (dashed line is at 0 km/s and dotted line is at 70 km/s)

Regarding figure 3.1.2, the following comments can be made on the species:

- C II: 1036,33 Å:
    - Properly aligned with the ISM velocity marker.
    - At first sight, it might look like it has 2 components but in fact the line at the left is most likely O IV** 1035,8, a stellar line, since it lies at approximately -60 to -70 which is the same difference in velocity-space from the stellar marker to the ISM marker. Were the graphic plotted in order of the O IV** line, the secondary line would appear centered at 0.
- C III: 977,02 Å:
    - Looks a bit shifted to the left of the ISM velocity marker, but this line seems to originate in the ISM
    - Potentially blended with something on the left, which might justify its shift.
- O I 1039,23 Å:
    - Properly aligned with the ISM velocity marker.
    - There seems to be only a single absorption component but its possible that other components exist but are not detected due to the resolution of FUSE
- N I 1134,96 Å:
    - Reasonably aligned with the ISM velocity marker.
    - It is the strongest transition of a N I triplet, yet it is still a very weak line as its profile hints, which is why it was the only line from the triplet plotted.
- Fe II 1144,94 Å:
    - Reasonably aligned with the ISM velocity marker.
    - This is a weak absorption feature that seems to have a shape that is not the expected one for a single absorption component, however due to the S/N and instrument resolution we cannot tell
- **S VI 944,52 Å:
    - Well centered around the marker for the star's photosphere velocity, thus leading to the conclusion that it is a stellar line.
- ** Si IV** 1066,62 Å:
    - Line is centered around the marker for the star's photosphere velocity, thus leading to the conclusion that it is a stellar line.
    - Furthermore, this transition is not observed under typical ISM conditions as it is a transition between two high energy states
- **P V 1117,98 Å:
    - Even though line is slightly shifted from the marker for the star's photosphere velocity towards the left (lower velocities), this is a stellar line.

The following table has all the measurements done using the method discussed in chapter 2, which consists in measuring the equivalent width (W) of an absorption line and calculating its column density (*N*) using the apparent optical depth technique.

| Species | Wavelength (Å) | Oscillator Strength (f) | f*λ | W (mÅ) | δW(mÅ) | N (*) | $\sigma_{up}$ (**) | $\sigma_{down}$ (**) |
|---|---|---|---|---|---|---|---|---|
| Fe II | 1144.9379 | 1.06E-01 | 1.21E+02 | 11.53 | 2.12 | 13.00 | 0.09 | 0.10 |
| N I | 1134.9803 | 4.16E-02 | 4.72E+01 | 12.49 | 1.62 | 13.45 | 0.06 | 0.07 |
| C II | 1036.3367 | 1.18E-01 | 1.22E+02 | 99.12 | 4.44 | 14.18 | 0.05 | 0.05 |
| C III | 977.02 | 7.58E-01 | 7.41E+02 | 150.31 | 9.54 | 13.71 | 0.13 | 0.16 |
| O I | 1039.2304 | 9.07E-03 | 9.43E+00 | 21.59 | 3.05 | 14.45 | 0.07 | 0.08 |

*N value presented in logarithmic scale with original units as atoms, ions or molecules/cm$^2$; ** same units as N

Table 3.1: Equivalent width and column density measurements for ISM lines along the line of sight to WD 0455-282

First, regarding the calculation of the uncertainties:

- The final error of the equivalent width measurement ($W_\lambda$) is split into two errors that are output separately by the program used. The first part, i.e. the total error, takes into account the Poisson noise, the fixed pattern noise, and the errors in the coefficients used to place the continuum. The second part takes into account the error on the equivalent width when the continuum is moved up and down by 2%.
- Here we calculated the final error by applying the error propagation formula:
  $\delta W_\lambda = (\text{total error}^2 + 2\%\text{error}^2)^{1/2}$
- A similar analysis is used to derive the uncertainties in the column density, N. Because the errors might not be symmetrical, we use $\sigma_{up}$ and $\sigma_{down}$ to denote the upper and lower 1 sigma error bars, respectively.

This method of calculation of uncertainties will be used throughout all chapter 3 on the other targets' measurements.

Regarding the values calculated in table 3.1, some comments can be made about a few lines that warrant extra explanation to better help understanding of the values obtained:

- C III: 977,02 Å:
  - The velocity range of the C II 1036,33 was placed as the limits for C III to calculate $W_{\square}$ and N since there might be the possibility that C III is blended with stellar features.
  - This reasoning is valid when assuming the gas that gives origin to this transition is the same as the one for C II.
- N I 1134,96 Å:
  - This is strongest transition of the N I triplet, yet as it can be seen from the plot in figure 3.2 this line is very weak. Thus, measuring even weaker lines would be hard to achieve and that's why the strongest line was chosen, when usually it is avoided to prevent possible saturation effects.

## 3.2. Results for WD 1611-084

As it was referred in chapter 2.4 this star is a DA white dwarf, meaning, that its atmosphere is rich in hydrogen. The graphics below represent the section of spectra of the white dwarf observed with the FUSE observatory and GHRS spectrograph, an older instrument onboard the Hubble Space Telescope that was later replaced by STIS, which had a much superior resolving power, introduced in chapter 2 and according to table 2.

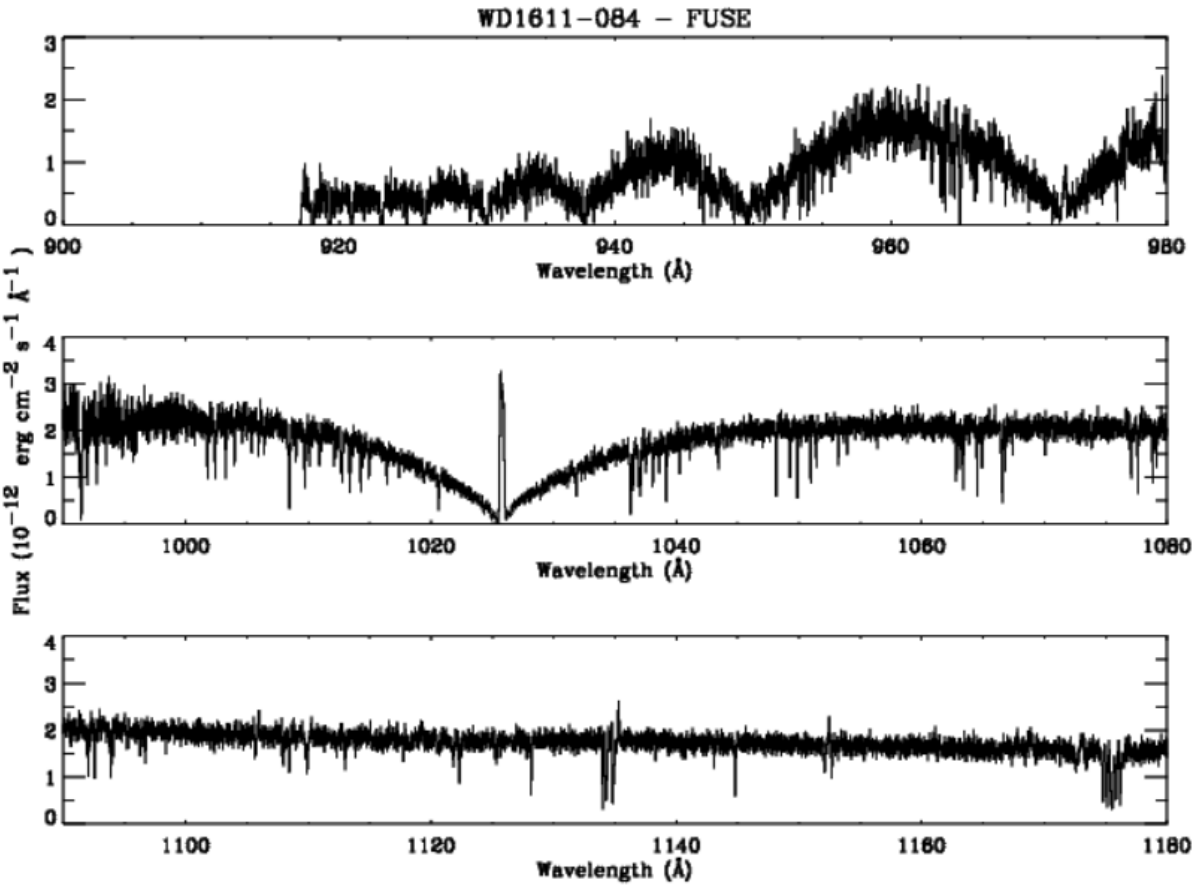


Figure 3.2.1 – FUSE spectra of WD 1611-084

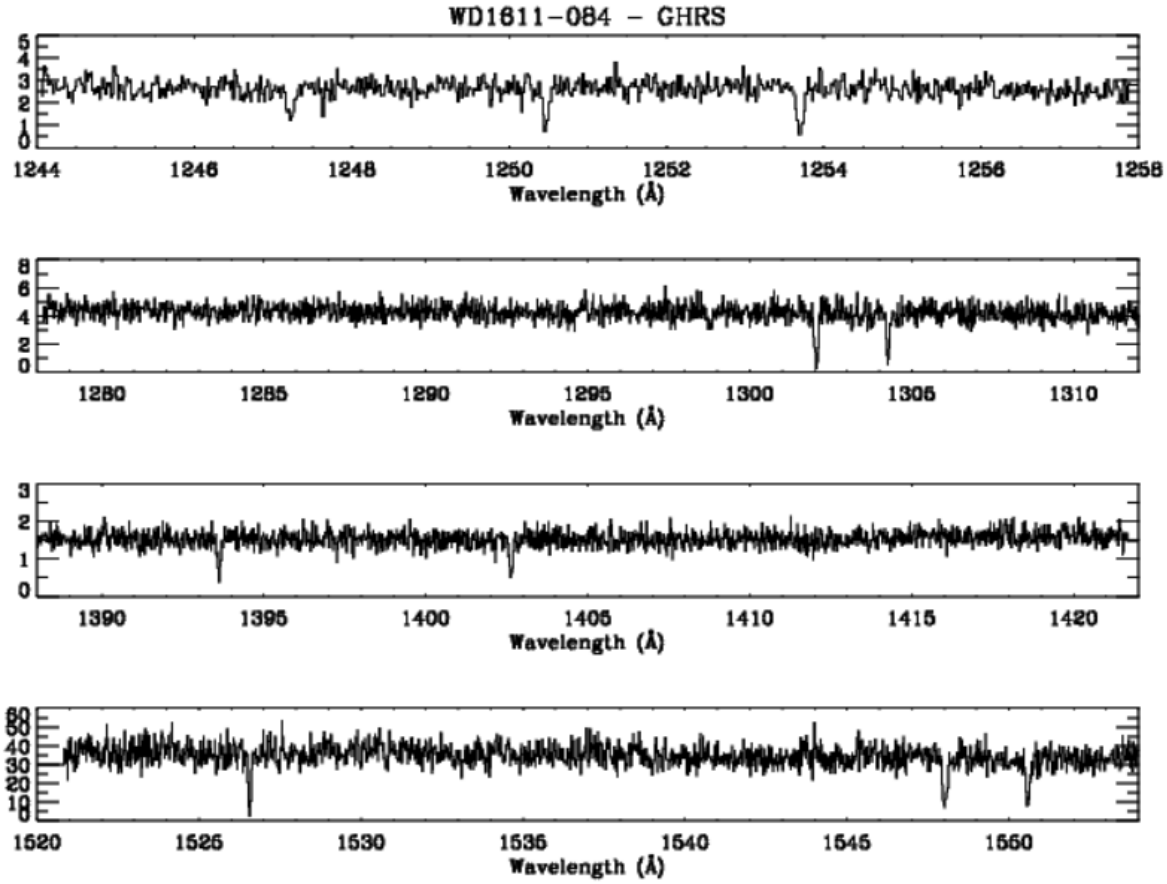


Figure 3.2.2 – GHRS spectra of WD 1611-084

The following graphics represent the normalized flux of each relevant absorption line plotted in velocity-space (km/s). The considerations done in subchapter 2.1 about them still stand as valid for these as well.

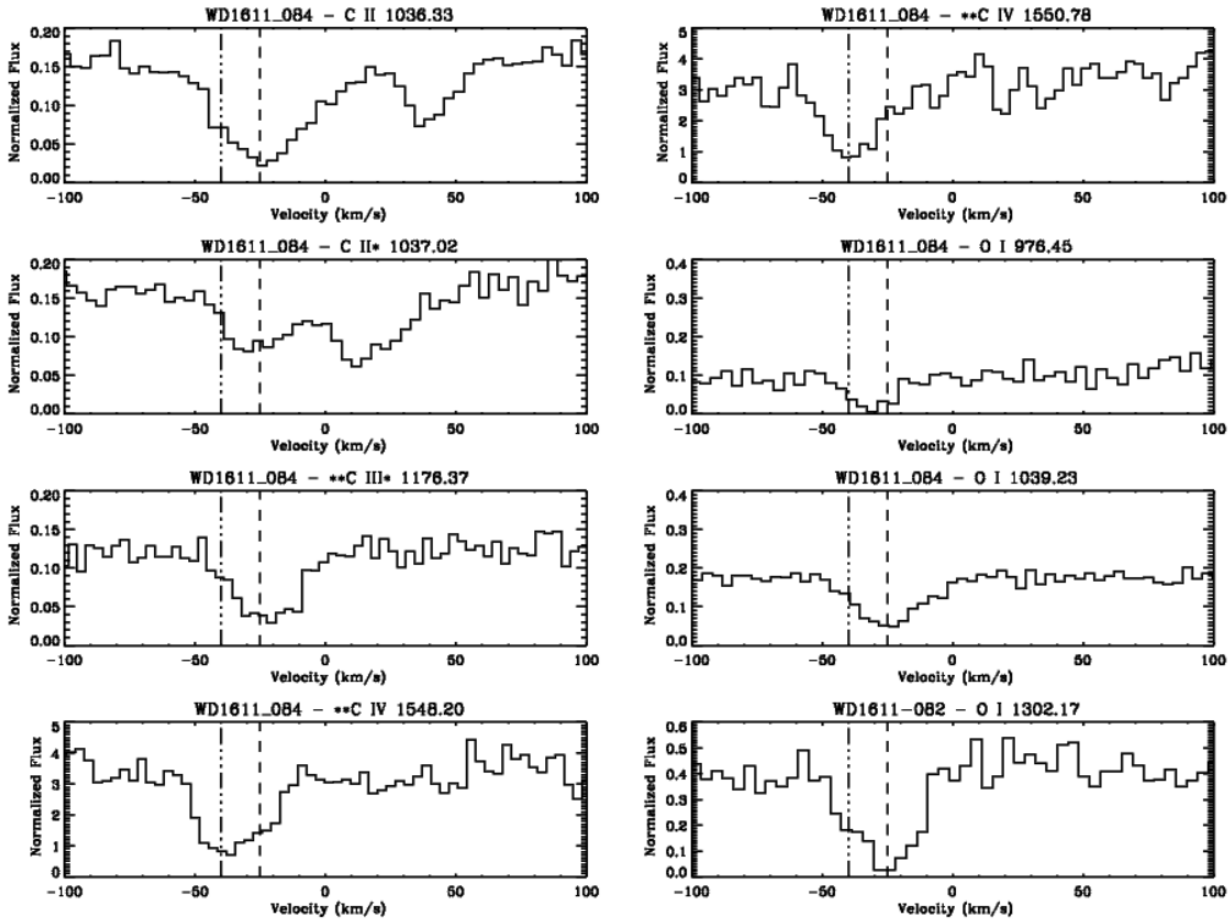


Figure 3.2.3: Relevant absorption lines identified in the spectra of the white dwarf WD 1611-084 (dashed line is at -25 k/s and dotted line is at -40 km/s)

Regarding Figure 3.2.3, the following comments can be made on the species:

- C II: 1036,33 Å:
  - Properly aligned with the ISM velocity marker.
  - It looks like there could be more than 1 absorption component but only profile fitting would allow us to tell for sure.
  - The feature at around 40 km/s is likely H20 (molecular hydrogen with *J=0*).
- C II* 1037,02 Å:
  - Line to the left is properly aligned with the ISM velocity marker.
  - The line at around 10 km/s is very likely an absorption line of H21 (molecular hydrogen with *J=1*).
  - Only proffit fitting would allow us to determine if there are more than one absorption components
- **C III* 1176,37 Å:
  - This particular transition only happens in the photosphere of the star since it is a transition between high energy states
  - The line is very shifted towards the right from the marker of the star's photosphere velocity (instead of being at -40 it's at around -25 km/s ).
  - Since this line is most likely stellar, this shift could be due to channel offset.
- ** C IV 1548,20 Å: and 1550,78 Å:
  - These lines correspond to ground state transitions of C IV and are sometimes seen in the interstellar medium. However the absorption velocity at – 40 kn/s, clearly places this absorption in the star's photosphere
- O I 976,45 Å:
  - Appears slightly shifted towards the left of the dashed line marker.
  - Despite being the weakest measured line from the O I species, there could potentially be some saturation since the line almost reaches 0. The fact that it does not reach has to do with resolution issues within the spectrograph that end up slightly broadening the line instead.
  - Given the S/N it is hard to tell whether it has more than 1 component.
- O I 1039,23 Å:
  - Properly aligned with the ISM velocity marker.
- O I 1302,17 Å:
  - Properly centered around the dashed line marker.
  - Stronger than the previous transitions, thus the line is much deeper, and is likely saturated
  - Due to S/N in the line, one cannot tell whether this line as more than 1 component, even if the line seems asymmetrical, which would indicate the presence of more than one absorption component
  - This line comes from the spectra obtained with GHRS, an instrument with lower resolution than STIS.

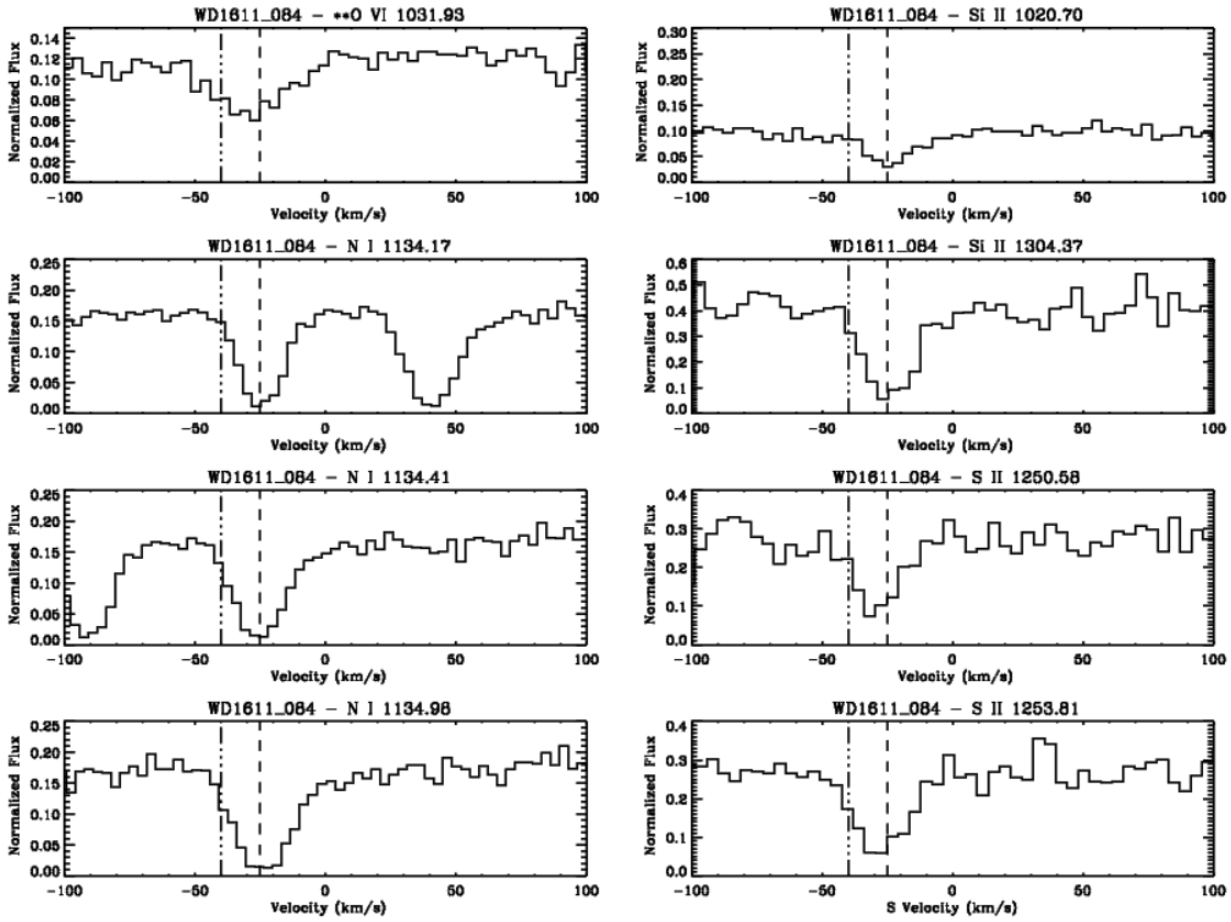


Figure 3.2.4: Relevant absorption lines identified in the spectra of the white dwarf WD 1611-084 (dashed line is at -25 k/s and dotted line is at -40 km/s)

Regarding figure 3.2.4, the following comments can be made on the species:

- **O VI 1031,93 Å:
  - This line corresponds to a ground state transition of O VI and is seen sometimes in the interstellar medium. It is also sometimes seen in the photosphere of the stars.
  - The line seems to align well with the ISM velocity marker, but given the proximity of the ISM and stellar absorption and the small misalignments in the FUSE data only profile fitting combined with a stellar model would allow us to determine the origin of this line (ISM vs. stellar photosphere)
- N I 1134 triplet (1134,17 Å, 1134,41 Å and 1134,98 Å):
  - All 3 lines are centered at around ISM velocity marker., which is the velocity expected for the ISM.
  - The strongest line is N I 1134,98, which can be seen since it is the deepest and broadest line of them all.
  - All lines almost reach 0 and are quite broad, so its possible that even the weakest line is saturated.

- Si II 1020,70 Å and Si II 1304,37 Å:
    - Both lines are properly centered around the ISM marker.
    - The weakest line is the Si II 1020,70 Å as it can be seen from its profile.
    - The low S/N in the continuum around the line does not allow us to determine whether there are any other features at other velocities.
    - Also, no other line clearly shows the existence of more than 1 component which would be expected if different absorption systems were to exist.
- S II 1250,58 Å and 1253,81 Å:
    - The lines appear roughly centered on the ISM dashed line marker.
    - The S/N is low in the continuum around the absorption lines, we cannot determine if there are any extra features at other velocities.
    - The 1253,81 is the strongest line, having a deeper profile and larger width. Looking at the peak of the line, it is possible that this line could be saturated.

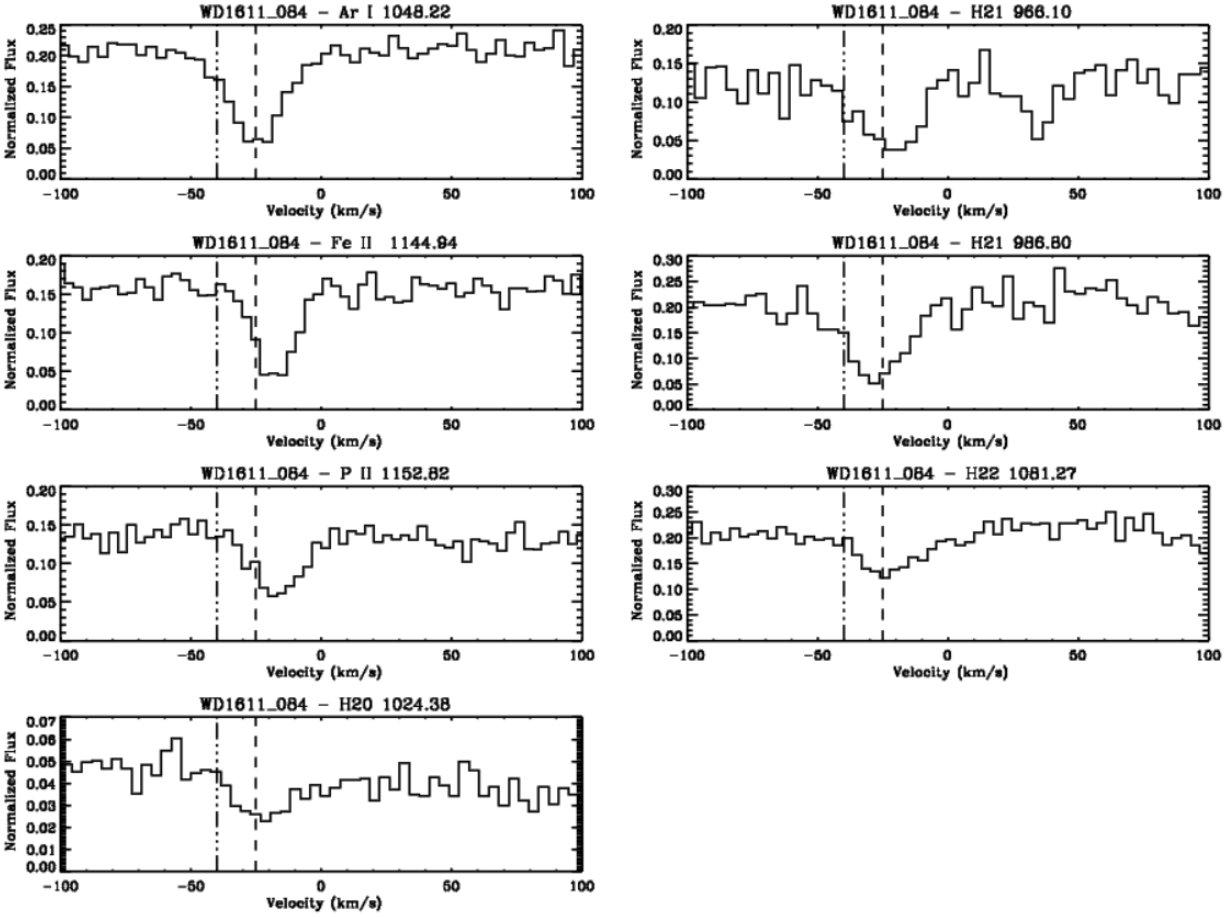


Figure 3.2.5: Relevant absorption lines identified in the spectra of the white dwarf WD 1611-084 (dashed line is at -25 k/s and dotted line is at -40 km/s)

Regarding figure 3.2.5, the following comments can be made on the species:

- Ar I 1048,22 Å:
    - Line is centered properly around the ISM line velocity marker.
    - No other lines can be seen, it is the strongest transition visible for this species.
    - The line has a very symmetrical profile showing no clear signs of having multiple components, even if more than one component can be present but not resolved by the instrument.
- Fe II 1144,94 Å P II 1152,82 Å:
    - Both lines are slightly shifted towards the right of the ISM line velocity marker.
    - They come from the same file as the N I triplet lines that don't appear to be shifted. Instead of a general offset of the whole spectrum, this could be an indicator that there are small scale velocities offsets within the data from a single channel.
    - Given the S/N in the continuum around the area of the lines, one cannot tell if there are other absorption components at different velocities.
- H20 1024,38 , H21 966,10 and 986,80 , and H22 1081,27
    - These lines are molecular hydrogen lines ($H_2$) corresponding to transitions between different J levels. For simplicity, in the figure they are labeled as H20, H21, and H22
    - All these lines were relatively aligned with the ISM velocity marker as expected since they are ISM lines and the main characteristic of molecular gas clouds.
    - They were not analyzed since this work does not have the objective of measuring and studying the abundances of molecular hydrogen.
    - They were included just as an example of this species. In fact, there were many more lines observed but these were the strongest lines and those which did not appear to be blended with stellar lines.

The following table has all the measurements done using the method discussed in chapter 2, which consists in measuring the equivalent width of an absorption line and calculating its column density using the apparent optical depth technique. Regarding the calculation of the uncertainties, what was said in the subchapter 3.1 stands valid for this subchapter as well.

| Species | Wavelength (Å) | Oscillator Strength (f) | f*λ | W (mÅ) | δW(mÅ) | N (*) | N adopted ($\sigma_{up}/\sigma_{down}$ **) | |
|---|---|---|---|---|---|---|---|---|
| Si II | 1020.70 | 1.64E-02 | 1.67E+01 | 61.59 | 5.83 | 14.75 | 14.75 | +0.06 |
| | 1304.37 | 9.17E-02 | 1.20E+02 | 84.91 | 9.45 | 14.03 | | -0.06 |
| C II | 1036.34 | 1.18E-01 | 1.22E+02 | 47.71 | 5.69 | 13.73 | 13.73 | +0.07 |
| | | | | | | | | -0.08 |
| C II* | 1037.02 | 1.18E-01 | 1.22E+02 | 50.69 | 3.49 | 13.76 | 13.76 | 0.05 |
| | | | | | | | | 0.05 |
| S II | 1250.58 | 5.43E-03 | 6.79E+00 | 57.19 | 7.53 | 15.04 | 15.04 | +0.08 |
| | 1253.81 | 1.09E-02 | 1.37E+01 | 83.96 | 9.66 | 14.94 | | -0.09 |
| O I | 976.45 | 3.31E-03 | 3.23E+00 | 51.50 | 8.07 | 15.55 | 15.55 | +0.19 |
| | 1039.23 | 9.07E-03 | 9.43E+00 | 74.78 | 5.88 | 15.11 | | |
| | 1302.17 | 4.80E-02 | 6.25E+01 | 112.28 | 9.42 | 14.50 | | -0.29 |
| P II | 1152.82 | 2.45E-01 | 2.82E+02 | 49.05 | 4.80 | 13.36 | 13.36 | ± 0.06 |
| Fe II | 1144.94 | 1.06E-01 | 1.21E+02 | 95.74 | 7.75 | 14.21 | 14.21 | ± 0.09 |
| Ar I | 1048.22 | 2.63E-01 | 2.76E+02 | 62.07 | 4.90 | 13.55 | 13.55 | ± 0.05 |
| N I | 1134.98 | 4.16E-02 | 4.72E+01 | 92.34 | 6.49 | 14.60 | ≤14.60 | |

*N value presented in logarithmic scale with original units as atoms, ions or molecules/cm$^2$; ** same units as N

Table 3.2: Equivalent width and column density measurements for ISM lines along the line of sight to WD 1611-284

Regarding the values calculated in table 3.2, some comments can be made about a few lines that warrant extra explanation to better help understanding of the values obtained:

- Si II 1020,70 Å and Si II 1304,37 Å:
    - Comparing the N value obtained for the 2 transitions it can be seen that they differ by more than 0,5 dex and do not agree within the error bars.
    - The 2 lines have a difference in oscillator strength superior to a factor of 5.
    - The fact that the strongest line gives a lower N indicates that the strongest line is saturated and so the column density derived from it is a lower limit.
    - The adopted N was chosen as the calculated N value of the weaker line, more reliable because saturation is less probable, although possible.
- S II 1250,58 Å and 1258,81 Å:
    - The difference in N values calculated for both is slightly different, with the stronger line giving a lower column density as expected in the case of saturation.
    - Because both lines give values that are only different by 1 dex, the weakest line is less likely to be saturated and therefore was chosen as the adopted N value for this species.
- O I 976,45 Å, 1039, 23 Å and 1302,17 Å:
    - The N values measured for all the lines do not agree within error bar values.
    - In the case of the strongest transition it is very likely to be saturated. One indicator is the fact that, despite the line being stronger than the other 2 by at least a factor of 7, its N value is much lower. If it wasn't saturated then the N values measured for all the lines should agree.
    - The adopted value for the N measurement for this species was chosen from the weakest line since it less likely to be saturated. Still, there could potentially be some saturation since the line almost reaches 0. However, to find that out either another line of the same strength or lower would be needed for comparison and there wasn't one. Another alternative, would be profile fitting.
- N I 1134,96 Å:
    - This is strongest transition of the N I triplet. As can be seen from the plot in figure 3.2.4 all the N I lines are very strong and are likely saturated.
    - The adopted N value can only be taken as a lower limit.

### 3.3. Results for WD 0232+035

As it was referred in chapter 2.4 this star is a DA white dwarf, meaning, that it's atmosphere is rich in hydrogen. Also, this star is fact part of a binary system and has as a companion that is a M dwarf. The graphics below represent the sections of spectrum of the white dwarf observed with the FUSE observatory and STIS spectrograph introduced in chapter 2 and according to table 2. Because this is a binary system the stellar lines appear at different velocities in each of the single different exposures and visits that were taken with FUSE while the ISM lines are stationary.

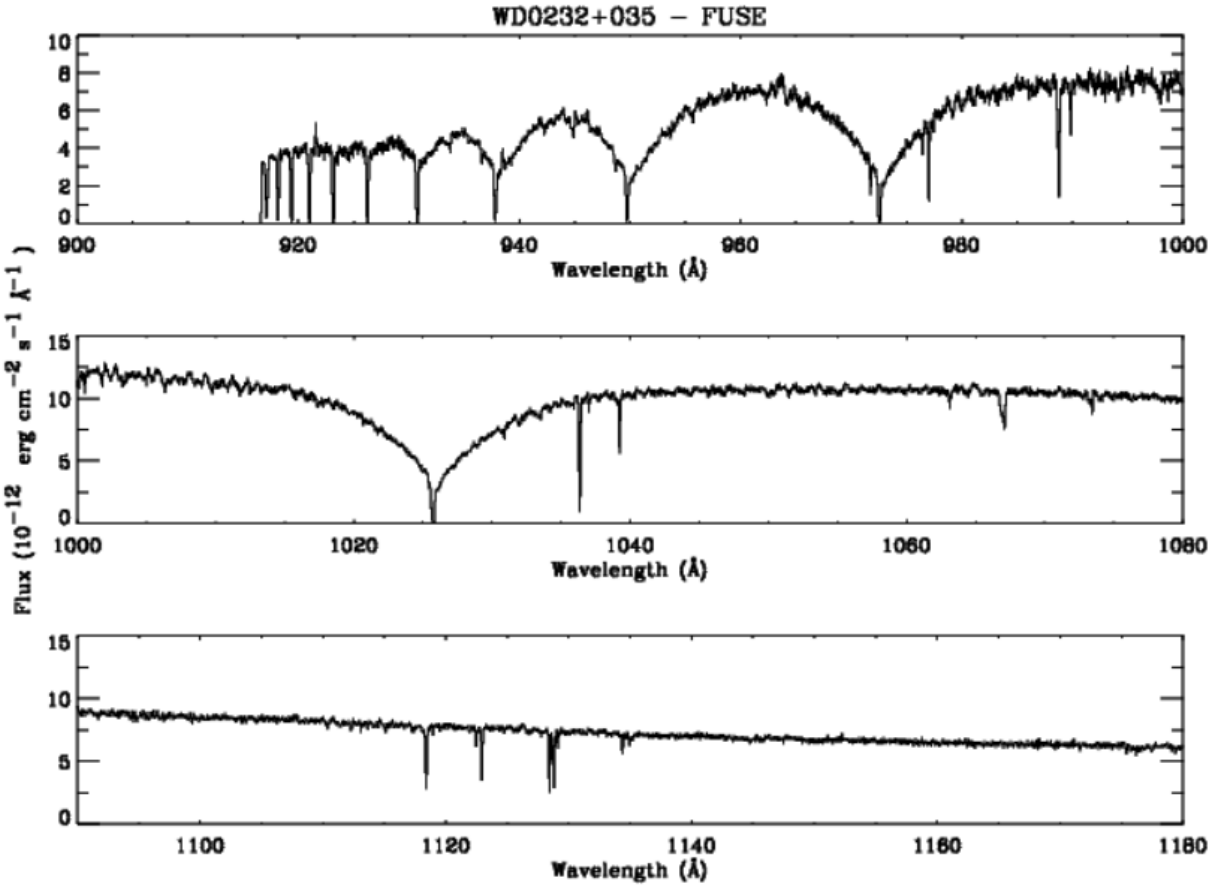


Figure 3.3.1 – FUSE spectra of WD 0232+035

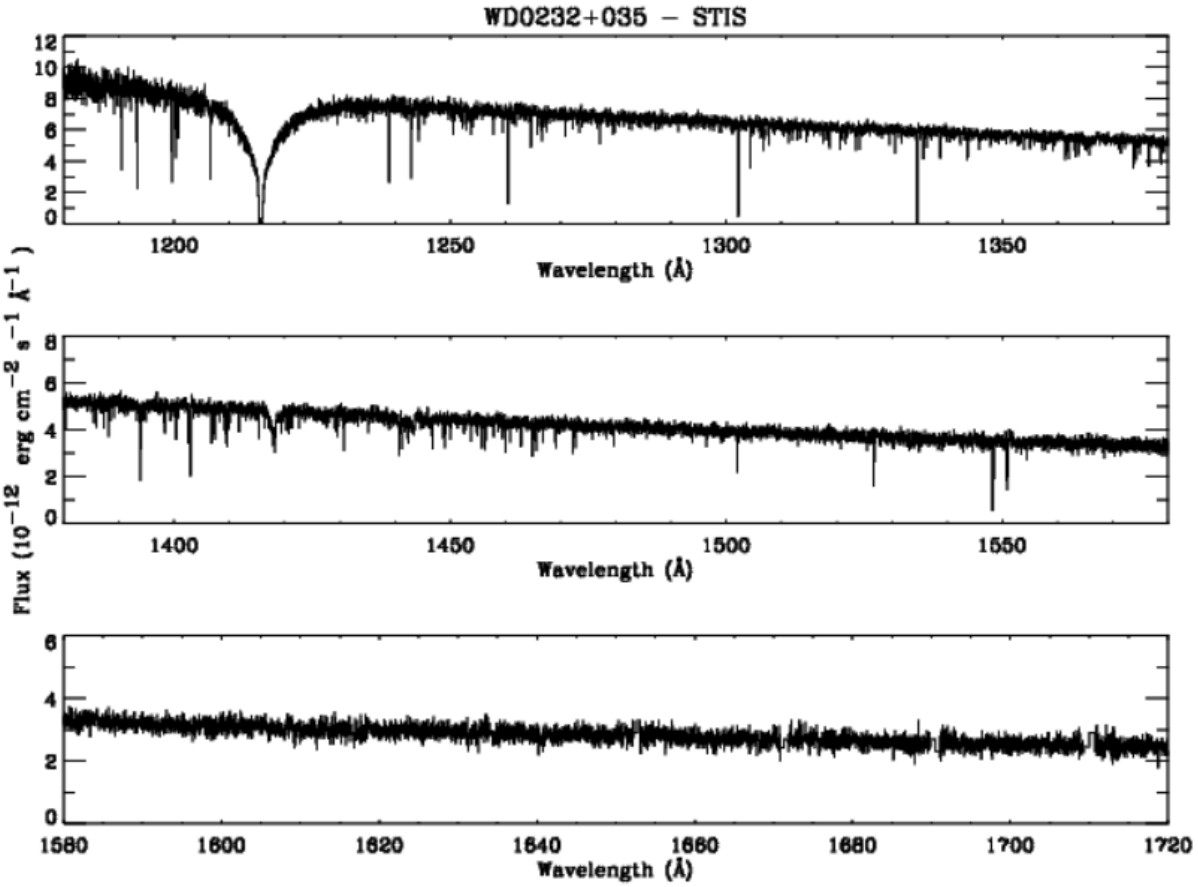


Figure 3.3.2 – STIS spectra of WD 0232+035

The following graphics represent the normalized flux of each relevant absorption line plotted in velocity-velocity (km/s). The considerations done in subchapter 2.1 about them still stand as valid for these as well.

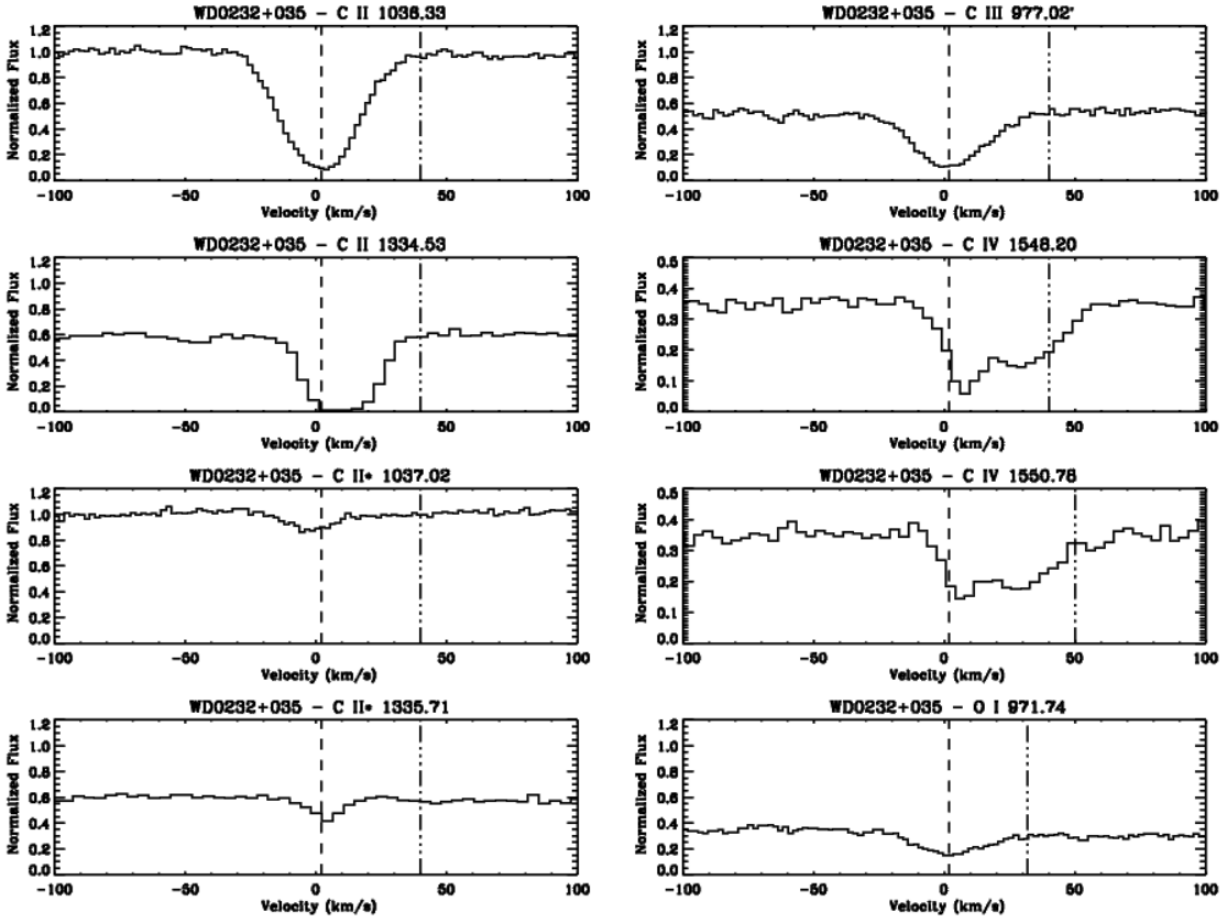


Figure 3.3.3: Relevant absorption lines identified in the spectra of the white dwarf WD 0232+035 (dashed line is at 2 k/s and dotted line is at 32 km/s)

Regarding figure 3.3.3, the following comments can be made on the species:

- C II 1036,33 Å and 1334,53 Å:
    - The 1036,33 Å lines appears to be aligned with the ISM velocity marker while the 1334,53 Å is slightly shifted towards the right. This discrepancy might be due to the fact that these lines were measured using different instruments, in which an offset might exist. Previous work has found two ISM components at around +2.85 and +17 km/s [9] so the 1334 line (from STIS) is likely at the correct velocity while the 1036 line (from FUSE) is likely offset due to a channel mis-alignment
    - The strongest line is actually 1334,53 Å and it can be seen that it reaches zero flux, so it is likely saturated.
- C II* 1037,02 Å and 1335,71 Å:
    - The lines appear to be slightly shifted from the ISM velocity marker in opposite directions. The same comment for C II 1036 and 1334 applies here regarding the velocity offset
    - The strongest line is 1335.
- C III 977,02 Å:
    - The line is centered around the ISM velocity marker and thus is not a stellar line.
    - This line is likely saturated but does not reach zero flux probably due to broadening by the instrument.
- C IV 1548,20 Å and 1550,78 Å:
    - The lines show two components. A narrower component consistent with the ISM marker and thus a non-stellar origin, and a broader component consistent with a photospheric origin.
    - The strongest line is the 1548,20 Å as it can be seen by its deeper core in the line's profile.

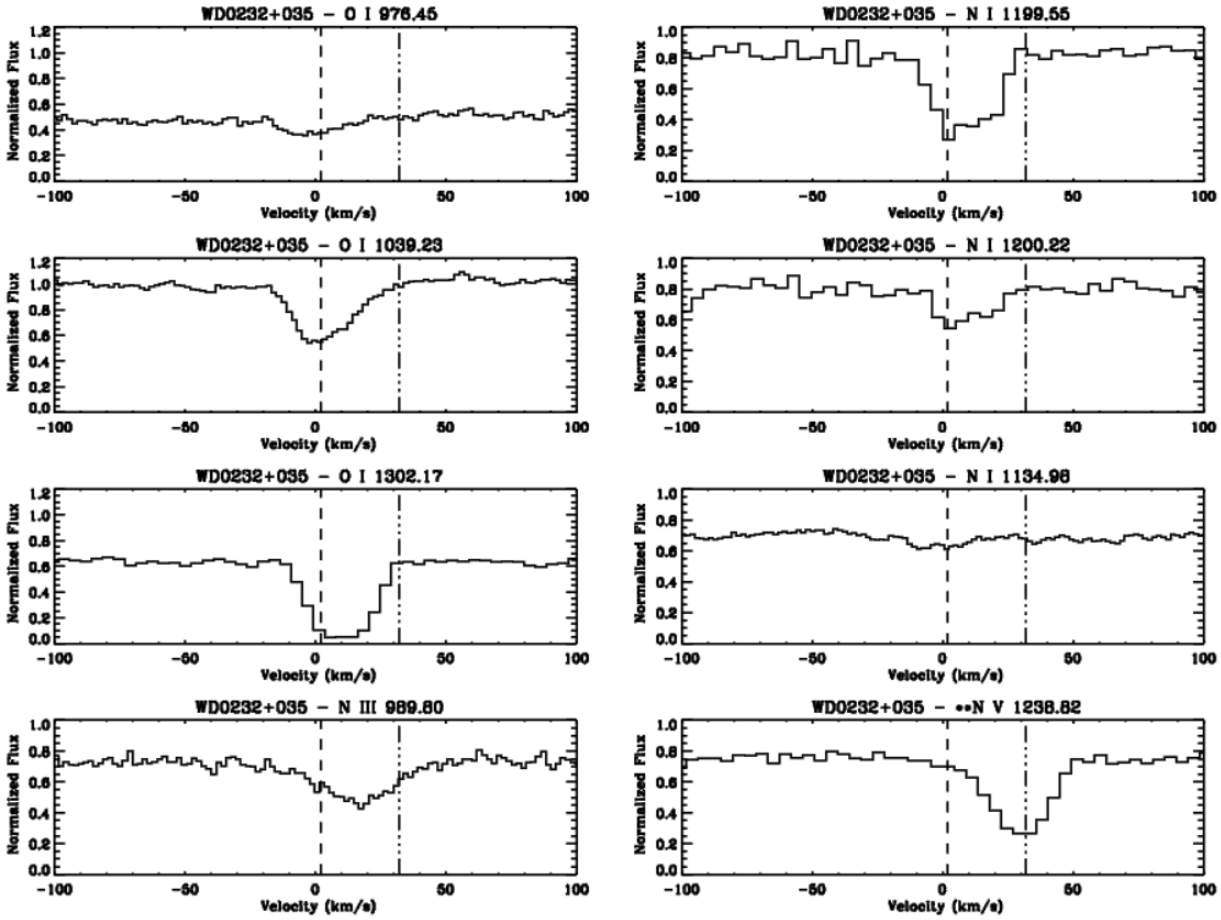


Figure 3.3.4: Relevant absorption lines identified in the white dwarf WD 0232+035 (dashed line at 2 k/s and dotted line at 32 km/s)

Regarding figure 3.3.4 (and still O I 971,74 Å from figure 3.3.3), the following comments can be made on the species:

- O I 971,74 Å, 976,45 Å, 1039,23 Å and 1302,17 Å:
  - The line 971,74 Å appears to be well centered around the marker for the ISM velocity while the 976,45 Å and 1039,23 Å lines, together with 1302,17 Å seem to have extra absorption on the right side of the line. This is consistent with the picture of two components as described above.
  - The strongest line is the 1302,17 Å as it can be seen by its deeper profile and it appears to be saturated.
- N III 989,60 Å:
  - The line looks considerably shifted to the right of the ISM velocity maker.
  - Without detailed stellar modelling it is hard to determine if this line if of stellar or interstellar origin, just from a kinematics analysis.

- N I 1134,98 Å, 1199,55 Å, and 1200.22 Å:
    - The lines appear to be aligned reasonably around the ISM velocity marker.
    - The strongest transition is the 1199,55 Å line since it has the deepest profile while the 1134,98 Å is the weakest and can barely be seen.
    - The 1199,55 Å line indicates the presence of more than 1 component albeit unresolved. This is further reinforced by the fact that other O I and Si II lines also look like they have more than 1 component.
- ** N V 1238,82 Å and 1242,80 Å (figure 3.3.5):
    - These are stellar lines and they look well aligned with the stellar velocity marker.
    - The strongest line is the 1238,82 but its profile looks only slightly deeper than the other weaker one 1242,80, so the difference can be difficult to identify.
    - Both present a wing-like structure.

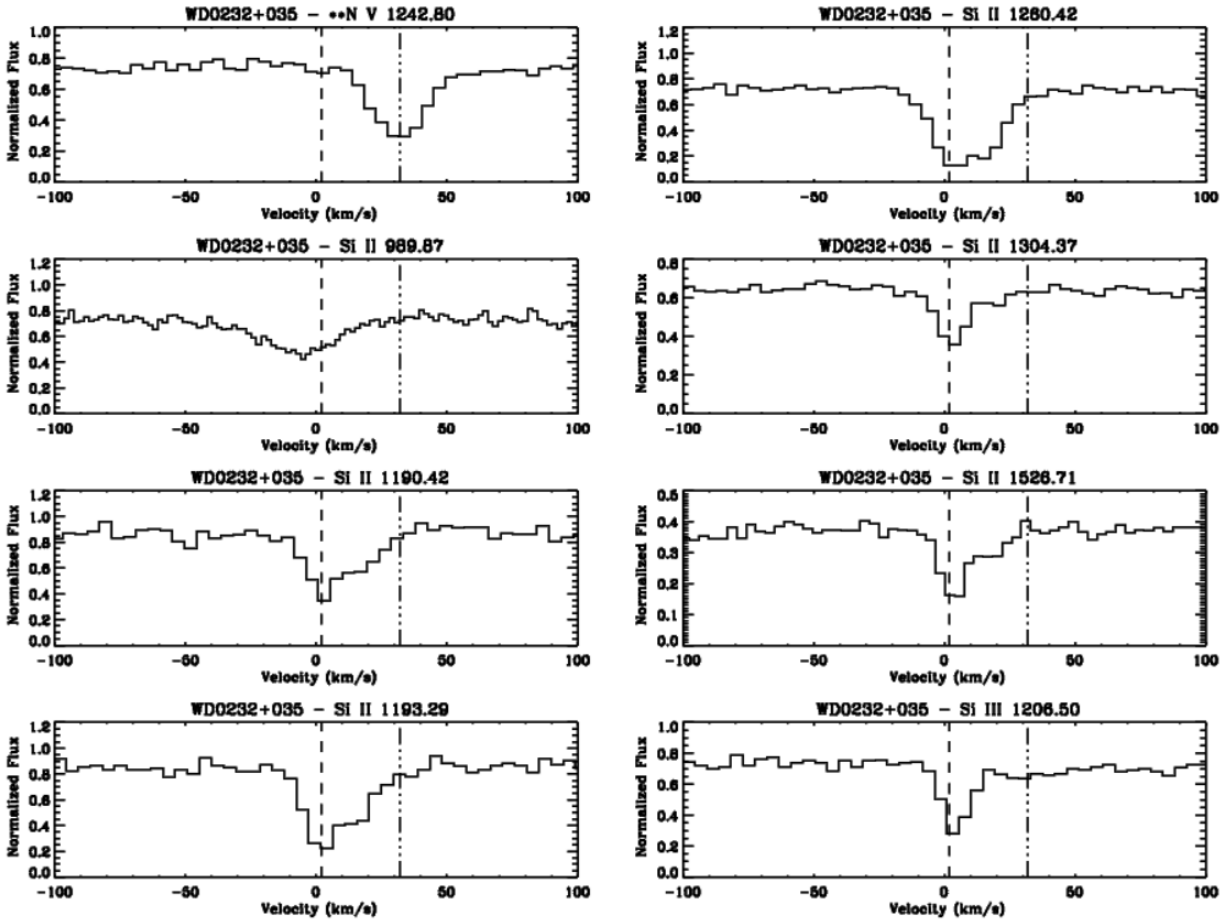


Figure 3.3.5: Relevant absorption lines identified in the spectra of the white dwarf WD 0232+035 (dashed line at 2 k/s and dotted line at 32 km/s)

Regarding figure 3.3.5, the following comments can be made on the species:

- Si II 989,67 Å, 1190,42 Å, 1193,29 Å, 1260, 42 Å, 1304,37 Å and 1526,71 Å:
    - The lines appear to be reasonably aligned around the ISM velocity marker.
    - The strongest line is the 1260 , 42 Å as it can be seen by its deep and slightly broad profile, while the weakest line is the 989,67 Å as it can barely be seen.
    - All of the above-mentioned lines, with the exception of the weakest, reveal a profile that strongly indicates the presence of more than 1 component, albeit unresolved. This is also present in other species like O I and N I for this target.
- Si III 1206,50 Å:
    - The line is positioned reasonably around the ISM velocity marker.
    - Given the S/N of the continuum around this line it is hard to tell if there is more than 1 absorption component.

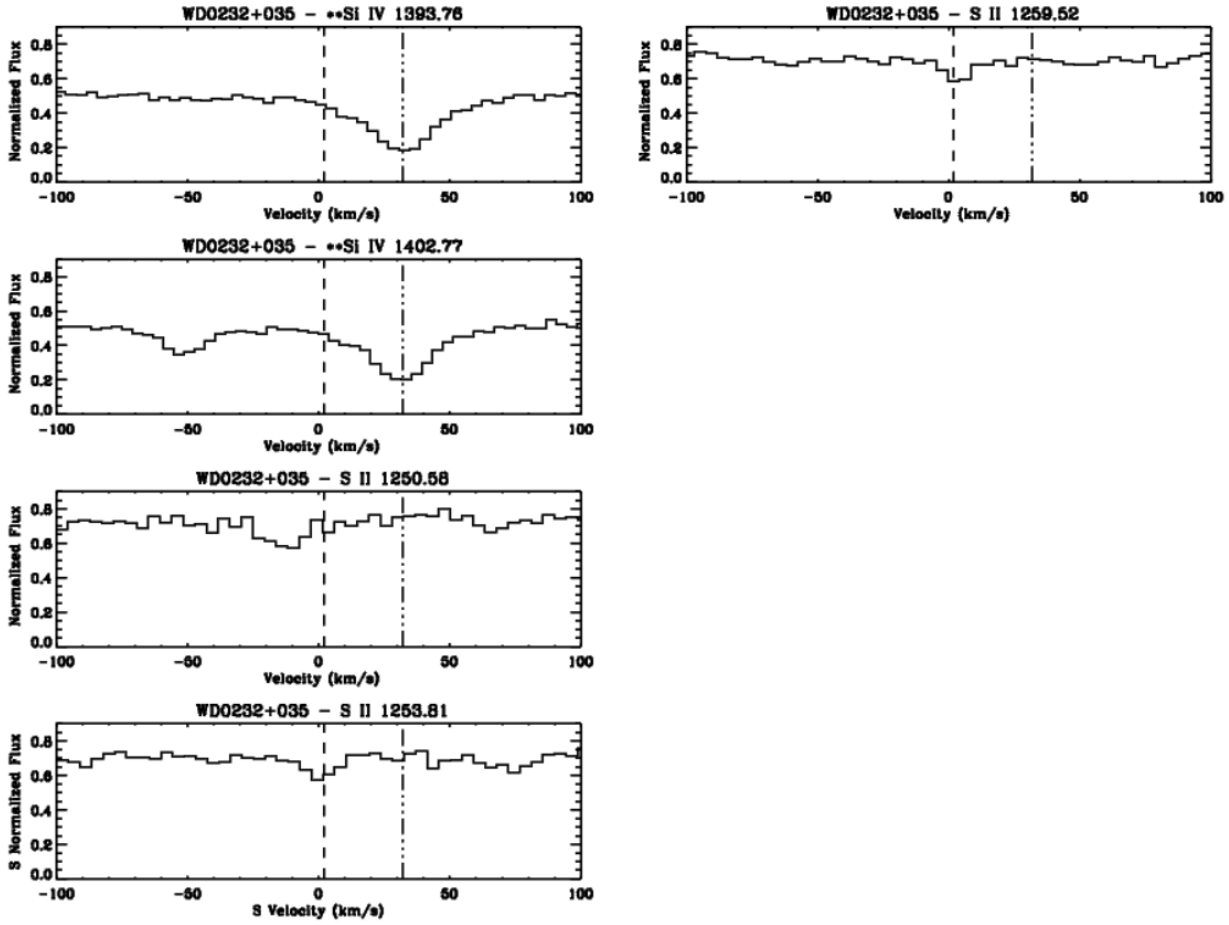


Figure 3.3.6: Relevant absorption lines identified in the spectra of the white dwarf WD 0232+035 (dashed line is at 2 k/s and dotted line is at 32 km/s)

Regarding figure 3.3.6, the following comments can be made on the species:

- **Si IV 1393,78 Å and 1402,77 Å:
  - These are stellar lines and well aligned with the stellar velocity.
  - The strongest line is 1398,78 Å.
  - Both are very broad due to thermal effect on the star's photosphere in which the gas is accelerated to very high velocities, which in turn, broadens the line. In this case, since the line is broader than the instrument resolution, the line is resolved and if it does not reach zero flux then it is not saturated.
- S II 1250,58 Å, 1253,81 Å and 1259,52 Å:
  - Two of the lines appear to be reasonably centered around the ISM velocity marker while another (1250,58 Å) is slightly shifted to the right.
  - Actually the 1250,58 Å is so weak that can hardly be seen and that line to the left is more likely a stellar line or an artifact from the instrument.
  - The strongest transition is 1259,52 Å as it can be seen from its line profile.

The following table has all the measurements done using the method discussed in chapter 2, which consists in measuring the equivalent width of an absorption line and calculating its column density using the apparent optical depth technique. Even though the presence of a second absorption component is hinted at in some of the lines, all the measurements performed here assume a single component. The presence of the second weaker component on the weaker lines, from which we derive N adopted, is not clearly seen and can only be properly determined with profile fitting. Regarding the calculation of the uncertainties, what was said in the subchapter 3.1 stands valid for this subchapter as well.

| Species | Wavelength (Å) | Oscillator Strenght (f) | f*λ | W (mÅ) | δW(mÅ) | N (*) | N adopted ($\sigma_{up}/\sigma_{down}$ **) | |
|---|---|---|---|---|---|---|---|---|
| Si II | 1190.42 | 2.93E-01 | 3.49E+02 | 54.78 | 4.25 | 13.28 | 13.48 | +0.04 |
| | 1193.29 | 5.85E-01 | 6.98E+02 | 73.96 | 3.76 | 13.17 | | |
| | 1260.42 | 1.18E+00 | 1.49E+03 | 107.65 | 3.85 | 13.04 | | |
| | 1304.37 | 9.17E-02 | 1.20E+02 | 34.95 | 2.67 | 13.48 | | -0.04 |
| | 1526.71 | 1.32E-01 | 2.02E+02 | 50.18 | 3.09 | 13.38 | | |
| Si III | 1206.50 | 1.67E+00 | 2.01E+03 | 41.19 | 3.67 | 12.38 | 12.38 | +0.05 -0.05 |
| N I | 1199.55 | 1.32E-01 | 1.58E+02 | 68.26 | 3.43 | 13.76 | 13.76 | +0.04 |
| | 1200.22 | 8.69E-02 | 1.04E+02 | 51.57 | 3.59 | 13.76 | | -0.04 |
| S II | 1253.81 | 1.09E-02 | 1.37E+01 | 11.58 | 1.35 | 13.91 | 13.55 | +0.08 |
| | 1259.52 | 1.66E-02 | 2.09E+01 | 7.69 | 1.32 | 13.55 | | -0.09 |
| C II | 1036.34 | 1.18E-01 | 1.22E+02 | 110.06 | 2.45 | 14.27 | 14.27 | +0.03 |
| | 1334.53 | 1.28E-01 | 1.71E+02 | 141.54 | 3.83 | 14.30 | | -0.03 |
| C II* | 1037.02 | 1.18E-01 | 1.22E+02 | 8.54 | 0.61 | 12.90 | 12.90 | +0.04 |
| | 1335.71 | 1.28E-01 | 1.71E+02 | 18.10 | 1.95 | 13.00 | | -0.04 |
| C III | 977.02 | 7.58E-01 | 7.41E+02 | 85.96 | 3.10 | 13.33 | ≤13.33 | |
| C IV | 1548.20 | 1.90E-01 | 2.94E+02 | 76.59 | 2.74 | 13.50 | 13.60 | +0.04 |
| | 1550.78 | 9.48E-02 | 1.47E+02 | 59.27 | 2.55 | 13.60 | | -0.04 |
| O I | 976.45 | 3.31E-03 | 3.23E+00 | 19.17 | 1.74 | 14.88 | 14.88 | +0.05 |
| | 1039.23 | 9.07E-03 | 9.43E+00 | 41.86 | 1.28 | 14.77 | | -0.05 |

*N value presented in logarithmic scale with original units as atoms, ions or molecules/cm$^2$; ** same units as N

Table 3.3: Equivalent width and column density measurements for ISM lines along the line of sight to WD 0232+035

Regarding the values calculated in table 3.3, some comments can be made about a few lines that warrant extra explanation to better help understanding of the values obtained:

- Si II 1190,42 Å, 1193,29 Å, 1260, 42 Å, 1304,37 Å and 1526,71 Å:
    - The weakest line was excluded from the measurements since it couldn't clearly be seen and appeared a bit broad.
    - The N values decrease with the strength of the line as expected.
    - While comparing the results for the 2 least strong lines, it can be seen that they are not consistent within the errors.
    - Nevertheless, the N value taken as valid for this species was the one pertaining to the weakest transition since it is the least likely to be saturated.
- N I 1199,55 Å and 1200,22 Å:
    - The line N I 1134,98 Å wasn't measured since it is too weak.
    - The strengths of the lines 1199,55 Å and 1200,22 Å differ by less than a factor of 2 and gave exactly the same value for N, which indicates that the line is not saturated and the column density derived with this method is reliable.
- S II 1253,81 Å and 1259,52 Å:
    - The value for the 1250,58 Å was not calculated since the line is very weak.
    - Comparing the N results for both measured lines, a discrepancy in values is noted. Usually this happens when the stronger line is saturated. However, looking at the absorption profile of the stronger line it seems very weak, so it is hard to tell if it is really saturated.
    - Instead, what might happen is that the weaker 1253,81 Å line could be blended with stellar features, which would account for the considerably higher N value. Therefore, the N value of the strongest line was adopted instead.
- C II 1036,33 Å and 1334,53 Å:
    - The measurements of N for the 2 lines agree within error.
    - As always, the value from the weakest stands as the most reliable since it is the least likely to be saturated.
- C II* 1037,02 Å and 1335,71 Å:
    - The measurements of N for the 2 lines do not agree within error.
    - The weakest line (1037), gives a lower N, which is not the expected behavior
    - The oscillator strength (f) for the 1335,71 Å line actually results from the sum of the f value of 2 very close C II* lines (1335,66 Å and 1335,71 Å) that are blended. Without this correction, the discrepancy between measured N values was even bigger.
    - Therefore, the value from the strongest stands as the most reliable since the weaker line gives a lower N.
- C III 977,02 Å:
    - Since this line appears to be saturated, the measured N value can only be a lower limit.

- C IV 1548,20 Å and 1550,78 Å:
    - Since the right component is of photospheric origin, only the left component was measured and used to derived column density.
    - Comparing both transitions, the N value measured are not consistent within errors. Since the most reliable value is the one from the weakest line due to being less likely to be saturated, the N value chosen was that from the 1550,78 Å.
- O I 976,45 Å and 1039,23 Å:
    - The N value of the 971,74 Å was not calculated since the line is very weak, while the N value for 1302,17 Å was not calculated because it is very likely to be saturated.
    - The 2 measured lines differ in strength by a factor superior to 2, as desired. However, the calculated N values are not consistent within errors and so, the value from the weakest is taken as most accurate one since it is the less likely to be saturated.
    - Nonetheless, it should be noted that saturation might be present is both lines.

## 3.4. Results for WD 2111+498

As it was referred in chapter 2.4 this star is a DA white dwarf, meaning, that it's atmosphere is rich in hydrogen. The graphics below represent the sections of spectrum of the white dwarf observed with the FUSE observatory and STIS spectrograph introduced in chapter 2 and according to table 2. The STIS data was obtained fairly recently, as so the analysis from that data presented cannot be compared with literature values.

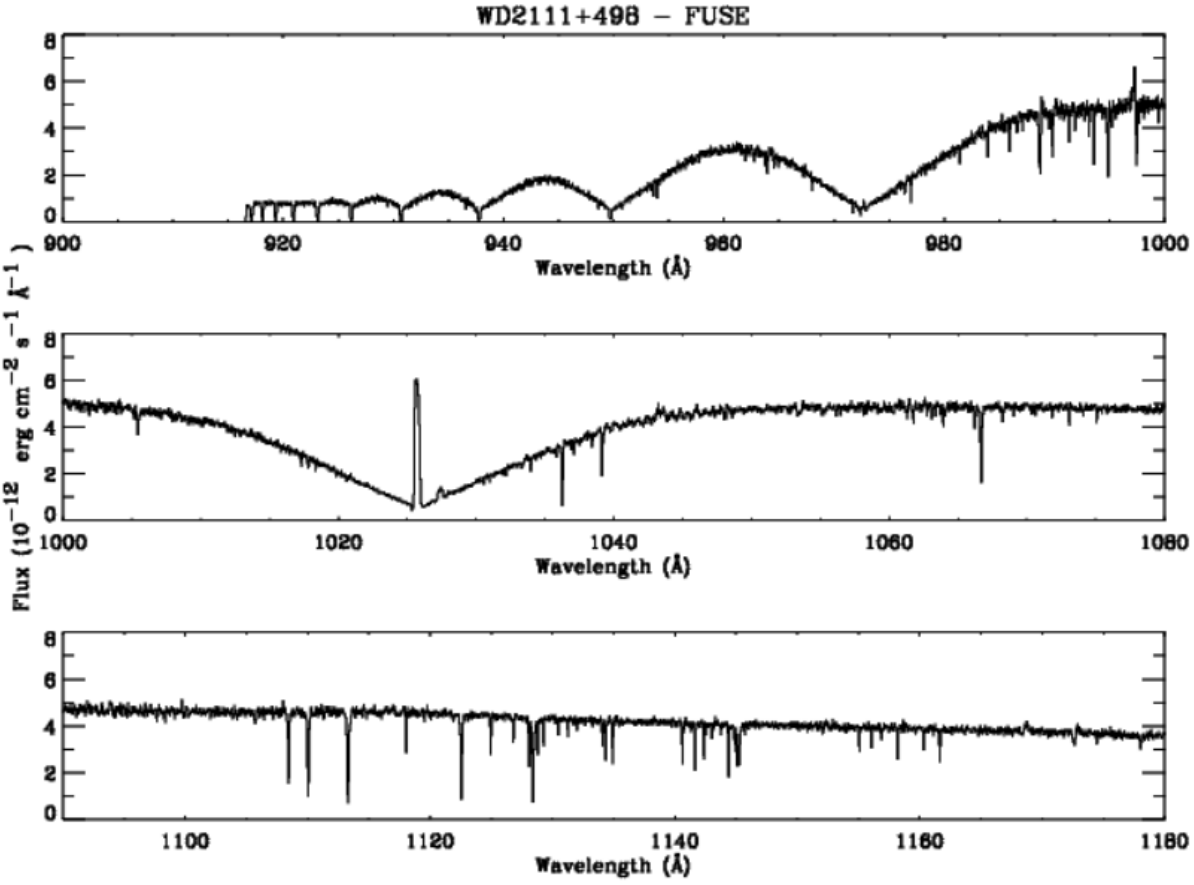


Figure 3.4.1 – FUSE spectra of WD 2111+498

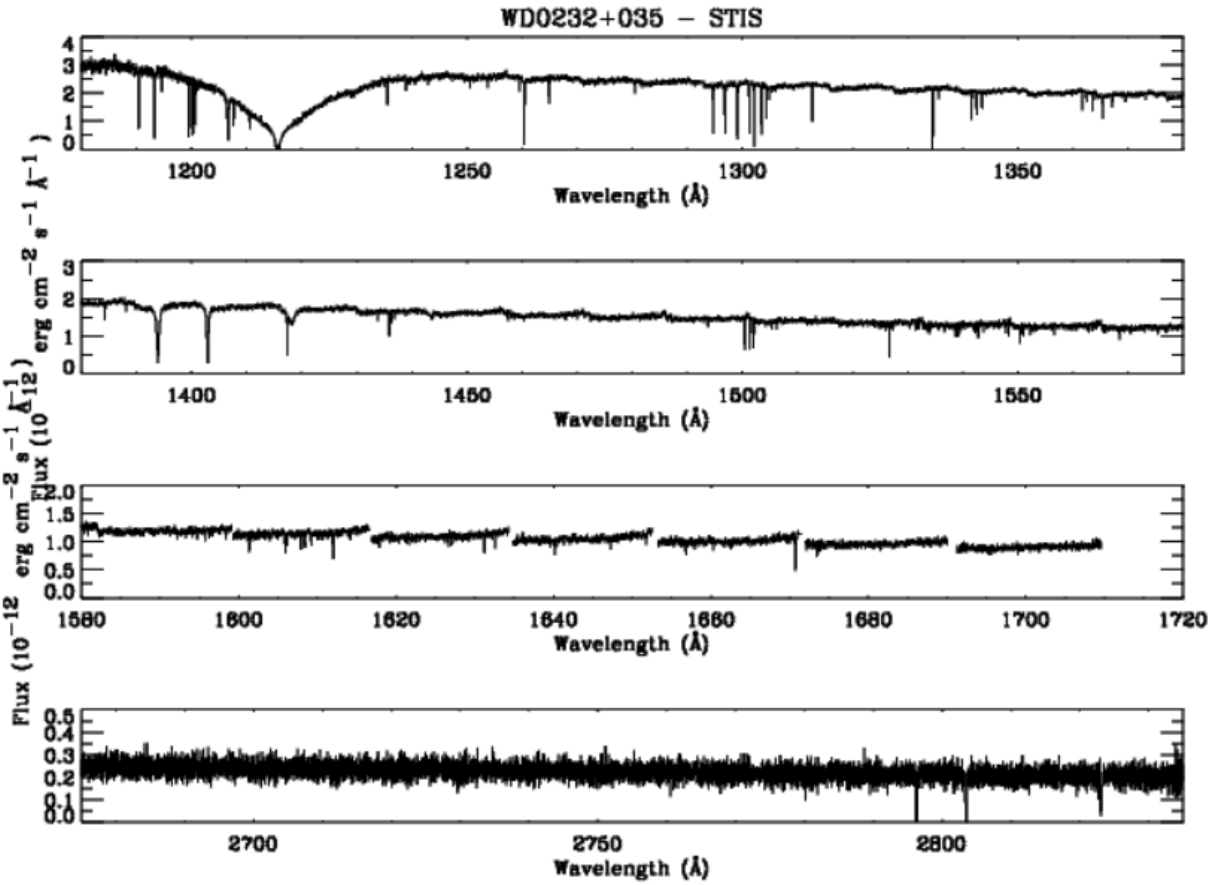


Figure 3.4.2 – STIS spectra of WD 2111+498

The following graphics represent the normalized flux of each relevant absorption line plotted in space-velocity (km/s). The considerations done in subchapter 2.1 about them still stand as valid for these as well.

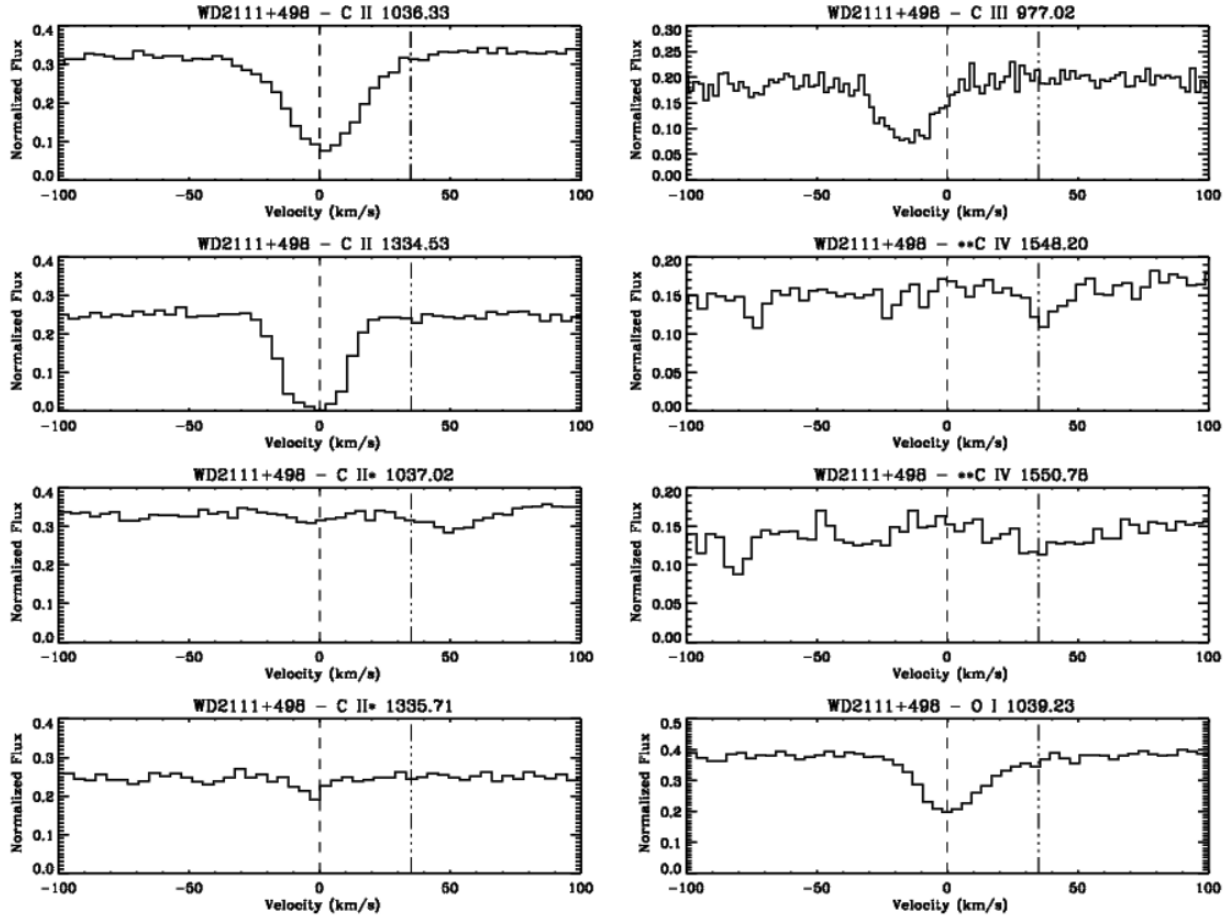


Figure 3.4.3: Relevant absorption lines identified in the spectra of white dwarf WD 2111+498 (dashed line is at 0 k/s and dotted line is at 35 km/s)

Regarding figure 3.4.3 (and O I 1302,17 Å from figure 3.4.4), the following comments can be made on the species:

- C II 1036,33 Å and 1334,53 Å:
    - The 1036,33 Å and 1334,53 Å lines appears to be reasonably well aligned with the ISM velocity
    - The strongest line is actually 1334,53 Å and it can be seen that it reaches zero flux, so it is possible that it might be saturated.
- C II* 1037,02 Å and 1335,71 Å:
    - The lines appear to be slightly shifted from the ISM velocity marker to the left.
    - The strongest line is the 1335,71 Å as it can be seen by its relatively more pronounced profile.
- C III 977,02 Å:
    - The line is shifted towards the left from the ISM velocity marker. This might be due to a wavelength offset in the data file since another line P II 963,60 Å, pertaining to the same file, seems to have a similar shift.
    - It could be saturated since it is very strong transition and the line looks quite broad.
    - Although the shape of the profile does not look symmetric it is hard to tell if there could be several components given the S/N.
- ** C IV 1548,20 Å: and 1550,78 Å:
    - The lines appear aligned with the stellar velocity marker and thus are likely stellar.
    - The strongest line is the 1548 Å as it can be seen by its deeper line profile.
    - The S/N in the continuum around the stellar does not allow us to detect any potential components at other velocities.
- O I 1039,23 Å and O I 1302,17 Å:
    - Both lines seem properly aligned with the ISM velocity marker.
    - The 1302,17 Å line is stronger than the other transition, thus the line is much deeper. Also, there might be saturation since the line reaches zero flux.
    - Although there is no indication of multiple components in these lines, only with profile fitting would one be able to determine if more than 1 components are present.

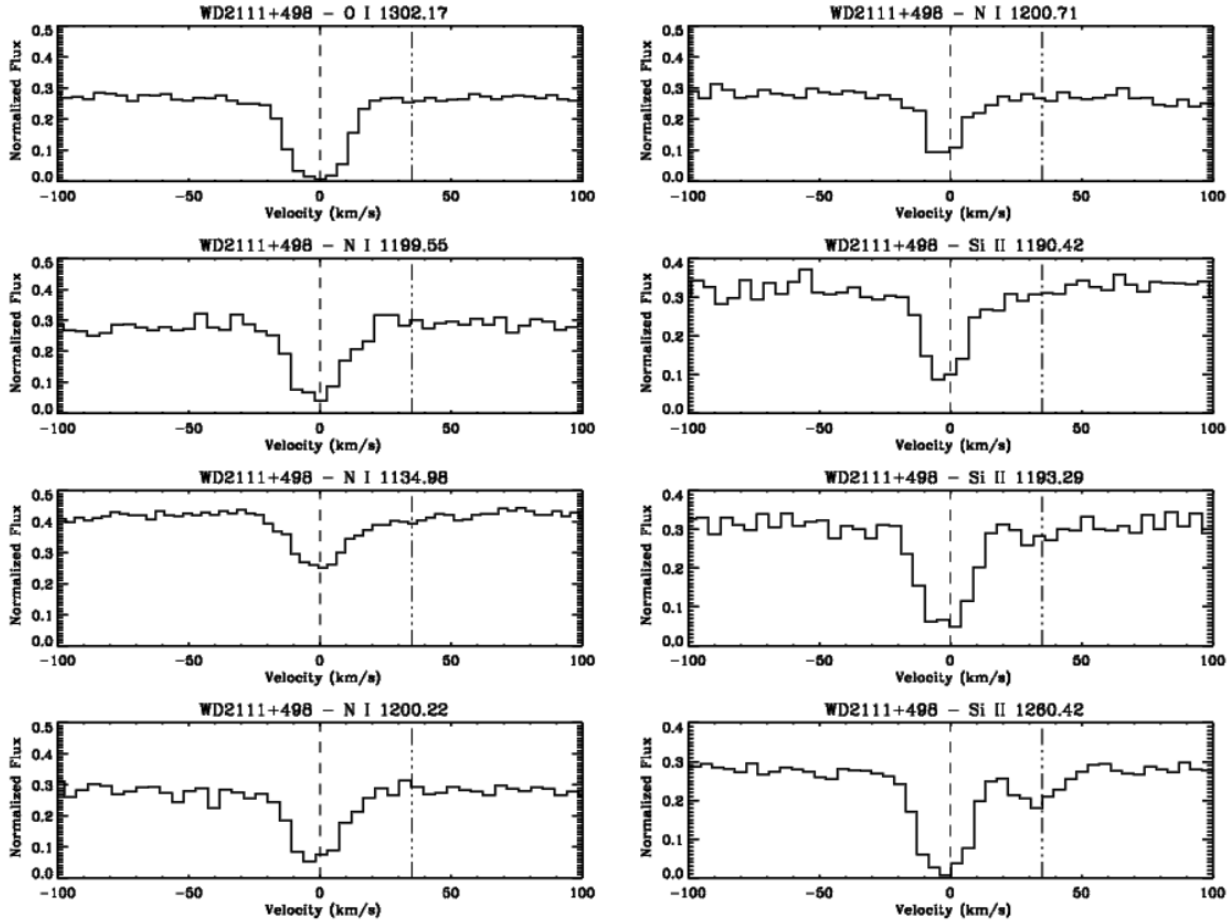


Figure 3.4.4: Relevant absorption lines identified in the spectra of white dwarf WD 2111+498 (dashed line is at 0 k/s and dotted line is at 35 km/s)

Regarding figure 3.4.4 (and Si II transitions from figure 3.4.5), the following comments can be made on the species:

- N I 1134,98 Å, 1199,55 Å, 1200,22 Å and 1200,71 Å:
    - The lines appear to be aligned reasonably around the ISM velocity marker.
    - The strongest transition is the 1199,55 line since it has the deepest profile while the 1134,98 is the weakest.
    - Both the 1199,55 Å and the 1200,22 Å appear to have more than 1 component albeit unresolved. This is further reinforced by the fact that other O I and Si II lines also look like they have more than 1 component.
- Si II 1190,42 Å, 1193,29 Å, 1260, 42 Å, 1304,37 Å and 1526,71 Å:
    - The lines appear to be reasonably aligned around the ISM velocity marker.
    - The strongest line is the 1260,42 Å as it can be seen by its deep and slightly broad profile. Also, the line reaches zero flux which could indicate the presence of saturation.
    - All of the above-mentioned lines have features in their profiles that hint at the possibility of having the more than 1 component, albeit unresolved.
    - The 1260,42 line seems to have a component at the stellar velocity. Without carefully modelling the stellar photosphere we cannot determine if this component originates in the photosphere or not.

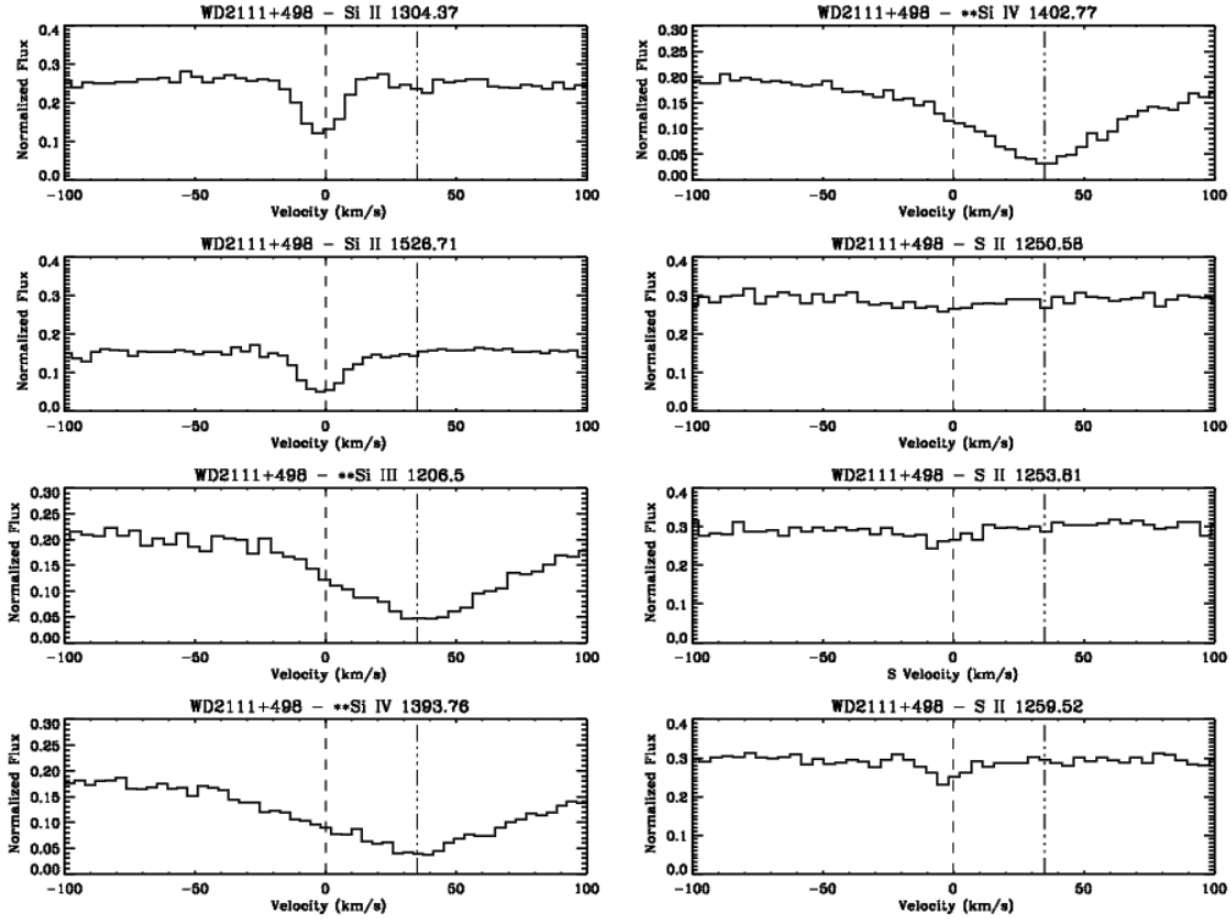


Figure 3.4.5: Relevant absorption lines identified in the spectra of the white dwarf WD 2111+498 (dashed line is at 0 k/s and dotted line is at 35 km/s)

Regarding figure 3.4.5, the following comments can be made on the species:

- ** Si III 1206,50 Å, **Si IV 1393,78 Å and 1402,77 Å:
    - These are stellar lines and well aligned with the stellar velocity marker.
    - The strongest **Si IV line is the 1398,78 Å and it can be seen that it looks slightly broader than the other weaker one 1402,78 Å.
    - All the lines are very broad which reinforces that it should be a stellar lines. This broadening of the line is due to thermal effects on the star's photosphere.
    - Also, since the lines are broader than the instrument resolution, they are most likely resolved and if they do not reach zero flux then probably are not saturated.
- S II 1250,58 Å, 1253,81 Å and 1259,52 Å:
    - All the lines look approximately well aligned with the ISM velocity maker, albeit a bit shifted towards the left. But since they are all very weak, their positioning regarding the marker is hard to understand.
    - The 1250,58 is the weakest line and almost impossible to distinguish from the noise of the continuum.
    - The strongest transition is 1259,52 Å as it can be seen from its line profile.

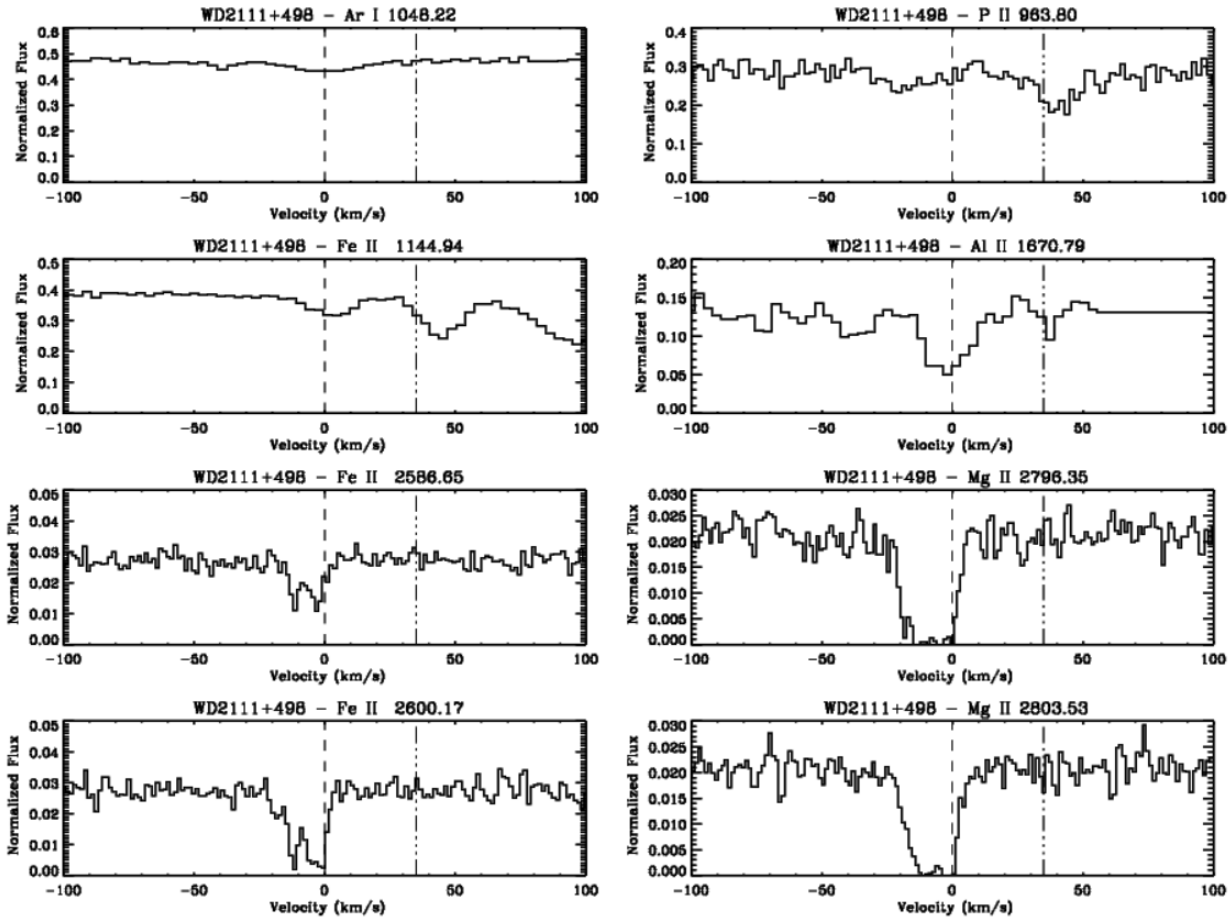


Figure 3.4.6: Relevant absorption lines identified in the spectra of the white dwarf WD 2111+498 (dashed line is at 0 k/s and dotted line is at 35 km/s)

Regarding figure 3.4.6, the following comments can be made on the species:

- Ar I 1048,22 Å:
  - Line appears to be centered properly around the ISM line velocity marker.
  - Despite being the strongest transition for this species, the line is barely visible.
- Fe II 1144,94 Å, 2586,65 Å and 2600,17 Å:
  - The 1144,94 Å appears to be slightly shifted towards the right of the ISM marker. Since other lines from the same file do present the same shift this might be due to channel offset.
  - The other 2 lines, 2586,65 Å and 2600,17 Å , appear to be shifted towards the left of the dashed marker, which is an effect also seen in the Mg II lines. Since these lines come from the same file this might be due to a wavelength offset particular to that data file.
  - Both 2586,65 Å and 2600,17 Å show the presence of at least 2 components, and perhaps 3 in the case of the strongest (2600,17 Å). These lines were obtained with the highest resolution mode on STIS, and so allow us to uncover for the first time the presence of multiple components for this line of sight.
- P II 963.8 Å:
  - The line appears to be slightly shifted to the left of the ISM marker, which could be due to a channel offset. The feature at around 40 km/s is likely a N I line (963.99 Å).
- Al II 1670,79 Å:
  - Line appears to be centered properly around the ISM line velocity marker.
  - Given the S/N in the continuum around the area of the lines, one cannot tell if there are other components at different velocities.
- Mg II 2796,35 Å and 2803,53 Å:
  - The lines appear to be shifted towards the left of the ISM velocity marker, which is an effect also seen in two of the Fe II lines at 2586 and 2600 Å. Since these lines come from the same file this might be due to a wavelength offset particular to that data file.
  - Both lines appear to have a multiple component structure, albeit unresolved.
  - The two lines also appear to be saturated.

The following table has all the measurements done using the method discussed in chapter 2, which consists in measuring the equivalent width of an absorption line and calculating its column density using the apparent optical depth technique. For the lines where we can clearly see a second component, the measurements for each of the components were performed separately. Regarding the calculation of the uncertainties, what was said in the subchapter 3.1 stands valid for this subchapter as well.

| Species | Wavelength (Å) | Oscillator Strength (f) | f*λ | more than 1 measurable component | W (mÅ) | δW (mÅ) | N (*) | N adopted ($\sigma_{up}/\sigma_{down}$ **) | |
|---|---|---|---|---|---|---|---|---|---|
| Si II | 1190.42 | 2.93E-01 | 3.49E+02 | | 73.51 | 7.98 | 13.46 | 13.61 | |
| | 1193.29 | 5.85E-01 | 6.98E+02 | main | 76.59 | 5.10 | 13.26 | | +0.04 |
| | | | | 2nd | 9.24 | 4.06 | 12.12 | | |
| | 1260.42 | 1.18E+00 | 1.49E+03 | main | 98.31 | 3.62 | 13.13 | | |
| | | | | 2nd | 26.89 | 2.29 | 12.27 | | |
| | 1304.37 | 9.17E-02 | 1.20E+02 | | 42.71 | 2.83 | 13.61 | | -0.04 |
| | 1526.71 | 1.32E-01 | 2.02E+02 | | 75.70 | 5.09 | 13.59 | | |
| S II | 1259.52 | 1.66E-02 | 2.09E+01 | | 11.25 | 1.64 | 13.72 | 13.72 | +0.07 -0.08 |
| Fe II | 2586.65 | 6.91E-02 | 1.79E+02 | 2nd | 20.40 | 2.65 | 12.81 | 13.27 | |
| | | | | main | 37.86 | 3.33 | 13.08 | | +0.08 |
| | | | | 3rd | 11.51 | 2.50 | 11.97 | | |
| | 2600.17 | 2.39E-01 | 6.21E+02 | 2nd | 37.20 | 2.92 | 12.70 | | -0.06 |
| | | | | main | 70.63 | 3.97 | 13.01 | | |
| Mg II | 2796.35 | 6.15E-01 | 1.72E+03 | | 203.61 | 8.50 | ≤15.68 | ≤15.96 | |
| | 2803.53 | 3.06E-01 | 8.58E+02 | | 195.16 | 9.21 | ≤15.96 | | |
| O I | 1039.23 | 9.07E-03 | 9.43E+00 | | 48.55 | 2.42 | 14.84 | 14.84 | ±0.03 |
| N I | 1200.71 | 4.32E-02 | 5.19E+01 | | 50.70 | 3.35 | 14.12 | 14.12 | 0.04/-0.05 |
| P II | 963.80 | 1.46E+00 | 1.41E+03 | | 17.77 | 2.23 | 12.21 | 12.21 | 0.06/-0.07 |
| Al II | 1670.79 | 1.83E+00 | 3.06E+03 | | 57.05 | 6.85 | 12.23 | 12.23 | 0.07/-0.08 |
| C II | 1036.34 | 1.18E-01 | 1.22E+02 | | 87.60 | 2.53 | 14.07 | ≤14.23 | |
| | 1334.53 | 1.28E-01 | 1.71E+02 | | 126.17 | 3.67 | 14.23 | | |
| C II* | 1037.02 | 1.18E-01 | 1.22E+02 | | 5.59 | 1.52 | 12.71 | 12.71 | +0.12 |
| | 1335.71 | 1.28E-01 | 1.71E+02 | | 5.68 | 1.27 | 12.68 | | -0.15 |
| C III | 977.02 | 7.58E-01 | 7.41E+02 | | 69.92 | 4.93 | 13.13 | 13.13 | +0.04 -0.04 |

*N value presented in logarithmic scale with original units as atoms, ions or molecules/cm$^2$; ** same units as N

Table 3.4: Equivalent width and column density measurements for ISM lines along the line of sight to WD 2111+498

Regarding the values calculated in table 3.4, some comments can be made about a few lines that warrant extra explanation to better help understanding of the values obtained:

- Si II 1190,42 Å, 1193,29 Å, 1260, 42 Å, 1304,37 Å and 1526,71 Å:
  - The N values decrease with the strength of the line as expected.
  - While comparing the results for the 2 least strong lines, with a difference in fλ by less than a factor of 2, it can be seen that they are consistent within the error.
  - The N value taken as valid for this species was the one pertaining to the weakest transition since it is the least likely to be saturated.
- S II 1250,58 Å, 1253,81 Å and 1259,52 Å:
  - The value for the 1250,58 Å and 1253,81 Å were not calculated since the lines are very weak.
  - The adopted N value for this species is that of the only measured line but since it is quite weak, saturation is unlikely.
- Fe II 1144,94 Å, 2586,65 Å and 2600,17 Å:
  - The value for the 1144,94 Å was not calculated since the line is very weak.
  - It was possible to measure 2 components in the 2586,65 Å and 3 in the strongest transition, 2600,17 Å.
  - In order to determine N, first the velocity range of the strongest line was calculated and then used as the velocity range of the weaker line, to ensure consistency of results.
  - The adopted final value for Fe II is that obtained by adding the column density of all the components, in this case both components measured for the weaker line.
- Mg II 2796,35 Å and 2803,53 Å:
  - Both lines are saturated (with the flux reaching zero) and thus it was not possible to calculate N using the program like it was done for the other line.
  - However, since we measured the equivalent width of each transition, using the formula 2.13 it was possible to establish a lower N limit for each transition.
  - Since both lines are saturated, the value chosen as the adopted N lower limit was that of the weakest transition since it likely more reliable.
- C II 1036,33 Å and 1334,53 Å:
  - The measurements of N for the 2 lines do not agree within error.
  - Also, the N value for the weaker line was lower than that of the stronger line. And since the strongest line was actually saturated, this puts in question the validity of the N value of the weaker line.
  - Thus, the value from the strongest line stands as the most reliable, despite being saturated, and is established as a lower limit.
- C II* 1037,02 Å and 1335,71 Å:
  - The measurements of N for the 2 lines do agree within error.
  - The oscillator strength (f) for the 1335,71 Å line actually results from the sum of the f value of 2 very close C II lines (1335,66 Å and 1335,71 Å) that are likely blended. Without this correction, the discrepancy between measured N values was much bigger.
  - Therefore, the value from the weakest stands as the most reliable as it is the least likely to be saturated.

- C III 977,02 Å:
    - Since there are no other transitions, the value calculated for this line stands as the N measurement for the species.
    - However, it is possible there could be saturation.

# Chapter 4: Discussion of Results

In this chapter, all results obtained and commented on chapter 3 will be further explained, if necessary, and compared with published results for each one of the targets. It should be noted, however, that some of the published results were derived from lower resolution data so they may not necessarily agree with the results obtained in this work.

The problem with limited spectral resolution of the instruments is that it does one allow one to understand the full complexity of the component structure in the spectra being evaluated. Lack of resolution will lead to different components or lines being blended and mistaken for one whole structure. In other words, resolution is the ability to break the line into its different components and resolve exactly where each should be recorded within the detector. It depends not only on the instruments' ability to "see" the different components, which is mostly dependent on the spectrograph and its gratings, but also on the relative strength of the components and their separation in velocity space. If an instrument had infinite resolution then the observed line will always be fully resolved and reach o whenever saturated, which would eliminate the biggest issue with this type of data and analysis: saturated lines that do not look like they are saturated, which in turn, leads to obtain erroneous values for abundances. The only way to circumvent this problem is to try to measure column densities using lines from the same species but with different strengths and compare them, usually adopting the column density value derived from the weakest line as the most reliable, since it is less likely to be saturated. However, many times there are no other lines available in the bandpass to compare.

Another interesting detail that could be seen was the difference between the shape of the lines originating from the star versus the non-stellar absorption lines. Stellar lines in these types of targets (hot white dwarfs) are usually much broader than interstellar lines they are broadened due to thermal effects in the photosphere of the WD. By contrast, the gas in the typical ISM probed by these lines of sight is at much lower temperature and, consequently, the lines are narrower and typically have a width of only a few km/s.

### 4.1. Comments on WD 0455-282

The first thing that could be easily compared is the values for the velocity of the star's atmosphere and the ISM gas found in this work ($v_{phot}$≈70 km/s and $v_{ISM}$≈0 km/s) versus those published. In Dickinson, et al. (2012) [9] they modeled the star's photosphere and derived with: $v_{phot}$=79,28±1,79 km/s and $v_{ISM}$=12,1±1,5 km/s. It is interesting to see, considering this is only a qualitative comparison since our values were estimated and not obtained through modeling, that both are shifted by around 10 km to lower velocities comparing with those from Dickinson, et al. (2012). If one attributes the shift to different methods of co-adding the same data, it can be said our values reasonably agree with those from Dickinson, et al. (2012). Another detail that supports this reasoning is the fact that the **Si IV** and **S VI, stellar lines, are also blue shifted by 10 km/s, which makes the shift a problem resulting from different treatments of data and not because of inconsistencies of measurements.

In this same paper, the velocity for the circumstellar medium was predicted as being $v_{CS}$=18,8±3,34 km/s, from an analysis of C IV, N V, and Si IV, observed with the International Ultraviolet Explorer (IUE). We found no evidence of circumstellar absorption in any of the species we studied in this work and the FUSE bandpass does not cover the C IV, N V, and Si IV wavelength regions. It could be, as the authors suggest, that despite the star being too far to ionize the LISM, some ISM cloudlets near the star are being ionized, which would suggest that the source of pollution for this star could be not only the circumstellar medium but also the ISM.

However, in another study from Lehner et al (2003) [22], the authors did measure abundances from FUSE data for the same species as in this work, namely Fe II, O I and N I.

| Species | Thesis abundances | Uncertainties | Lehner et al. (2003) | Uncertainties |
|---|---|---|---|---|
| O I | 14,45 | +0,07 / -0.08 | ≥14,91 | – |
| Fe II | 13,00 | +0,09 / -0,10 | 12,94 | +0,06 / - 0,11 |
| N I | 13,45 | +0,06 / -0,07 | 13,44 | +/- 0,15 |

It is curious to see that both the Fe II and N I abundances agree within errors values while the O I value shows a large discrepancy, especially since the Lehner et al. (2003) is supposed to be a lower limit. This could be justified by the presence of saturation in our data; it is possible that the O I transition from which we measure the column density suffers from saturation, despite appearing relatively weak, which made the N value lower than it should be, while Lehner et al. (2003) used a weaker O I file, thus obtaining a higher N value.

Now reflecting, exclusively on the data obtained in this work, it was also interesting to find that O I, Fe II, C II and N I all seem to have only one ISM component. In order to obtain accurate values for the velocity of this component and confirm this assumption, detailed profile fitting would have to be done to the data.

## 4.2. Comments on WD 1611-084

Once again, starting by comparing the values for the velocity of the star's photosphere and the ISM gas absorption found in this work ($v_{phot}$≈-40 km/s and $v_{ISM}$≈-25 km/s) versus those published. In Dickinson, et al. (2012) [9] they modeled the photosphere and derived: $v_{phot}$=-40,76±3,56 km/s and $v_{ISM}$=-34,7±1,5 km/s. It is interesting to see, considering this is only a qualitative comparison since our values were estimated and not obtained through modeling, that while the photosphere velocity agrees with our values the ISM velocity is shifted by -10 km/s.

Reflecting on the data found on this work, both C IV (1458 Å and 1550 Å) and C III (1176 Å) lines were identified, which were clearly stellar and at the velocity predicted by Dickinson, et al. (2012). On the other hand, many other absorption lines, which were not measured by the authors, were found at our value for the ISM absorption velocity, namely the N I 1334 Å triplet, C II, C II*, Si II, S II, Ar I, Fe II and P II. Moreover, another interesting aspect was the presence of molecular hydrogen lines, which were also detected at our estimated ISM velocity. This difference in ISM velocity between our measurements and those of Dickinson et al. (20120 [9] is strange because if it were due to a data treatment problem then the shift would be equally seen in stellar lines, which is not. To better understand this inconsistency, more detailed profile fitting of the data of the absorption lines would have to be done to confirm the velocity estimated on this work.

In this same paper, the velocity for the circumstellar medium was also predicted as being $v_{CS}$=-66,67±2,05 km/s, based on a stellar model fit to the photospheric lines, which also included a circumstellar component. We found no evidence of circumstellar absorption in the lines we studied here. Also, according to the author, since the circumstellar velocity is so different from the ISM velocity, any circumstellar material will be located very near the star hinting at the vaporization of planetesimal material.

Another paper by Holberg et al. (1997) [37] hinted at the presence of 2 ISM components at around 47 km/s, namely Si II and O I. Nonetheless, during the analysis of the same data no evidence of their presence was found.

Finally, for this target, the abundances obtained cannot be compared since there are no published results for these species for this star.

## 4.3. Comments on WD 0232+035

This target is a white dwarf that is part of a binary system along with a M dwarf, which will lead to its photospheric velocity to change according to the binary's phase. Therefore, according to Redfield and Linsky (2008), data quoted on the Dickinson, et al. (2012) paper [9], the photospheric velocity will be $v_{phot}$=30,11±0,52 km/s (binary phase 0,24) or $v_{phot}$=128,23±0,31 km/s (binary phase 0,74). The Dickinson, et al. (2012) paper also modeled the stars' photosphere and derived the ISM and circumstellar velocities : $v_{ISM}$=2,8±0,34 km/s (Component 1) or $v_{ISM}$=17,0±1,3 km/s (Component 2) and $v_{CS}$=7,4±0,34 km/s.

This will have an effect on observation in velocity space when it comes to stellar lines, depending on when the data was collected. This explains why some stellar lines appear at slightly different velocities such as 989 Å N III (FUSE) comparing with N V 1238 Å and 1242 Å (STIS).

Secondly, comparing the values estimated for the velocity of the star's photosphere and the ISM gas absorption found in this work ($v_{phot}$≈32 km/s and $v_{ISM}$≈0 km/s) versus those published, it can be said that they agree within the range of values given.

Reflecting on the data found on this work, it was seen that multiple lines hinted at the presence of 2 components, such as Si II, N I and O I, which Dickinson, et al. (2012) authors also suggest. One of those was also C IV, which appeared to have an absorption component at a velocity similar to the circumstellar velocity, in addition to the photospheric absorption.

For the C IV circumstellar component the author determined a column density of N(C IV) = 13,44±0,02 while the one obtained from this work is 13,60 ± 0,04. This difference might be due to the placement of continuum of the line on the left side or by measuring some part that is blended with stellar features.

Another author, Linsky et al. (2006) [38], has measured the abundance value for Si II and obtained column density values of 13.54±0.07 that agree within errors with the values obtained in this work, which were 13.48 ± 0.04.

Lastly, it can only be said that since the value for the ISM velocity and the circumstellar velocity are so close to each other, that in order to determine with better certainty whether a non-stellar line is of ISM or circumstellar origin, one would have to do first profile fitting to determine more accurate values for its velocity. The author Dickinson, et al. (2012), however, suggests that the material being ionized in the target's photosphere is material being lost from its M dwarf companion. [9]

### 4.4. Comments on WD 2111-498

Firstly, starting by comparing the values for the velocity of the star's atmosphere and the ISM gas absorption found in this work ($v_{phot}$≈35 km/s and $v_{ISM}$≈0 km/s) versus those published. In Dickinson, et al. (2012) [9] they modeled the star's photosphere and derived: $v_{phot}$=28,3±1,66 km/s and $v_{ISM}$=-7,6±1,3 km/s. It is interesting to see, considering this is only a qualitative comparison since our values were estimated and not obtained through modeling, that our values seem to be shifted by around +7 km/s comparing to the authors. If one attributes the shift to different methods of co-adding the same data, it can be said our values reasonably agree with those from Dickinson, et al. (2012). It should also be noted that the author did not detect any circumstellar component but also did not analyze STIS data (which only became available after 2012) .

Reflecting on the data found on this work, the Si II lines were found mainly at around the ISM velocity 0 km/s but in the case of Si II 1260 Å a component at the photospheric velocity of 30 km/s can also be seen. It is not clearly if the photospheric model would predict this Si II line or whether this line could have a circumstellar origin. Also, there are C IV lines (1548 and 1550 Å) at the photospheric velocity which were not predicted by the stellar model of Wilson et al. (2017) [13], yet observed, which suggests they might be circumstellar. In order to ascertain better the velocity of either C IV lines or Si II, proper profile fitting would have to be done to determine their exact velocities.

The other absorption lines, such as C II, C II*, O I and S II (FUSE and STIS), usually appear at 0 km/s and appear to have only 1 component. Nevertheless, it is curious that when the target is observed with a higher resolution instrument STIS (E230H grating) the 2796 Å and 2800 Å Fe II lines exhibit 2 to 3 identifiable components at around -2 km/s, -12 km/s and -20 km/s, from which the first is the strongest and interestingly is at the same velocity as the LIC (local interstellar cloud) at -2,35± 1.38 km/s [9].

Another interesting aspect found in the spectrum of this star was the existence of 2 spectral regions around 1417,5 Å and 1443,5 Å which seem to vary from exposure to exposure. First hinted by Dupuis et al. 2000 [21] was the possibility of the existence of a potential accretion spot in the white dwarf's photosphere, coming in and out of view, as a potential source of this variability and responsible for variations in extreme UV with 25% of amplitude during a period of 1,15 days. According to Wilson et al. (2017) [13] no variations were seen in the STIS spectra as released in their preliminary work. However, when carefully analyzing the same data by comparing 8 E140M STIS exposures, obtained at different times, it was found that there are areas of variability, 2 as stated before, that seem to oscillate around a non-fixed position, as seen in the image below. What is even more puzzling, is that no ISM absorption lines are predicted in those regions and no stellar lines were identified. In order to better understand this phenomenon, potentially stellar modeling would have to be done for this target.

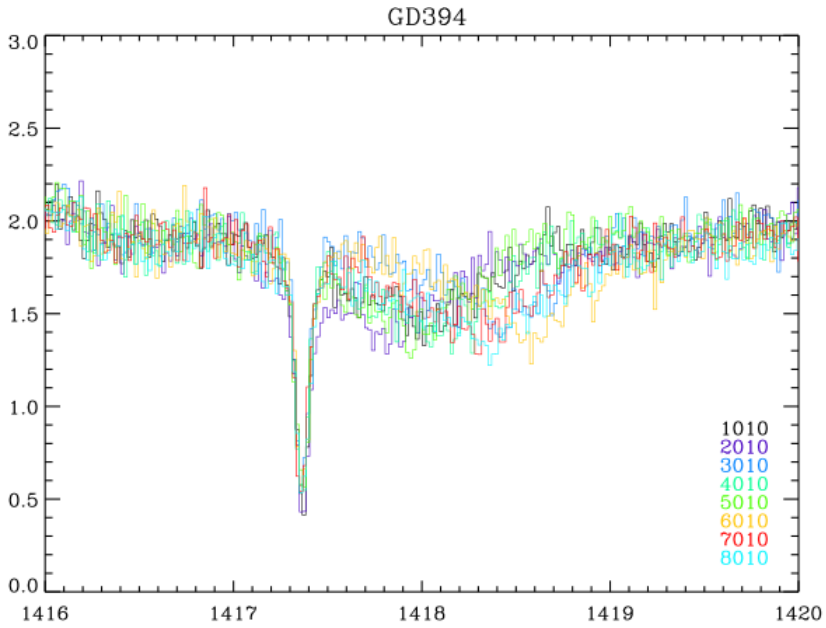


Figure 4.1: First area of variability at around 1418 Å to 1419 Å

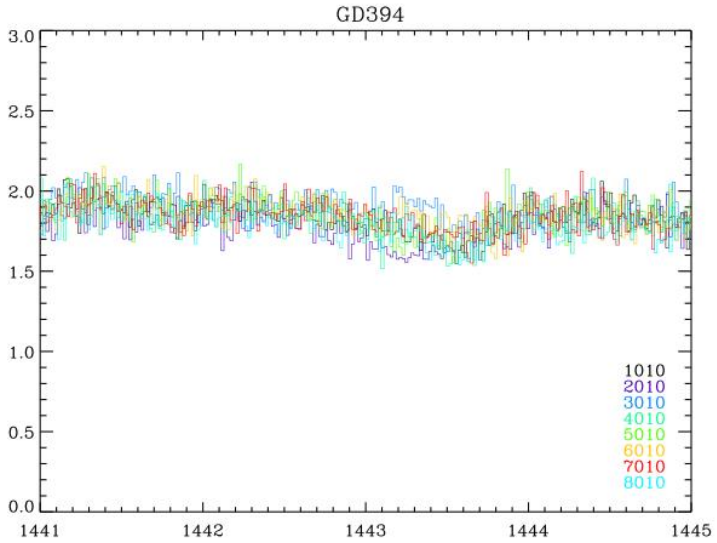


Figure 4.2: Second area of variability at around 1443 Å to 1444 Å

Finally, it was also possible to compare measured abundances for some species measured with previously published results, namely from Lehner et al (2003) [22], as seen in the table below:

| Species | Thesis abundances | Uncertainties | Lehner et al. (2003) | Uncertainties |
|---|---|---|---|---|
| O I | 14,84 | ±0,03 | 15,06 | +0,05 / -0,06 |
| Fe II (1 comp only) | 11,97 | +0,11 / -0,13 | 13,29 +/- 0,06 | |
| Fe II (2 comp) | 13,29 | + / - 0,04 | | |
| Si II | 13,61 | + / - 0,04 | 13,35 | + / - 0,04 |
| N I | 14,12 | +0,04/-0,05 | 14,00 | +0,08 / -0,03 |

As an overview, our column density results agree within the errors for Fe II. We derive a higher N(Si II) and of N(N I) than Lehner et al. (2003) [22] because our measurements are based on a weaker Si II line and N I line, available in the STIS data obtained after 2012, that is not covered by the FUSE data used by the author. Finally, the values obtained for N(O I) also do not agree within errors with the one obtained from the author, since our is considerably smaller.

# Chapter 5: Conclusions and Future Work

In this work four DA white dwarfs were studied and their spectra analyzed, having been identified more than 200 non-stellar absorption lines in total and measured the most relevant of them, determining the abundances of different species such as Fe II, Si II, S II, C II, C II*, N I and others.

In the previous chapters all results obtained for each target were explained and analyzed along with all relevant measurements made. In fact, one of the reasons why lines were presented in velocity space was so that it could be easily shown that absorption of circumstellar or ISM material is occurring at different velocities from purely stellar lines. Furthermore, it could also be seen that component structure is only truly identified when the instrument has very high-resolution power, like STIS, and even so saturation effects may be present which lead to the obtained values being only a lower limit.

When it comes to the advantages and applicability of the Apparent Optical Depth technique, one can conclude that it is indeed a very useful and straightforward technique to determine column densities of the different species, without prior knowledge of the component structure and that allows for saturation effects to be evaluated by comparing column densities derived from transitions with differing strengths. However, in order to study the component structure of a certain line it is hard to achieve clear results mainly due to problems intrinsic to the instrument used, like saturation effects. This is where profile fitting would be an appropriate complimentary technique to further the understanding of the target's spectrum and have a more detailed view of the component structure of any desired line. Nevertheless, this method is very complex and time consuming and would be a good topic for future work.

When it comes to comparison of results with other well researched ones, this is particularly hard since this is a relatively developing area of investigation, with less than 20 years of research, where much of the published work either concerns older data obtained from instruments of lower resolution or is mainly focused on the high ionization absorption species, when here the purpose was also to study lower ionization species. Therefore, to draw definitive conclusions, without more research into the observed lines through profile fitting and stellar modulation, would be premature and ill advised.

This area of work also has another difficulty, like any astronomical research, which is the fact that the experiment being studied cannot be repeated and the object of focus cannot easily be observed and studied. Thus, it is by nature, an area where one consistently has too improve on the science developed before and depends on work done by other researchers, sometimes unrelated and decades before one even starts their own project. This is why it is particularly exciting that one of the targets, WD 0455-282 was observed by STIS on the 15$^{th}$ of August of this year. Since STIS has a much higher resolution compared to FUSE it will be very interesting to get a better insight on the component structure of many already observed lines and potentially identify new ones, such as stronger O I lines and C IV, Fe II and N V lines, when the data becomes available to the community in 1 year.

In addition, future work would also entail using profile fitting to try to obtain a deeper understanding of the component structure of the lines observed, in order to determine more accurate abundancies measurements, and stellar modulation to better understand if all stellar lines were indeed stellar, if

the absorption lines seen were of truly of ISM origin or were perhaps circumstellar features and also to study the particular case of the accretion spot on star WD 2111+498, whose oscillations in the spectrum were disregarded and considered erroneously nonexistent, as we realized, and so far remains unexplained.

# Annex 1.1

This in an example for the WD1611-084.

```
pro save_lines_WD1611_084

  readcol,'C:\Users\Aalis\FUSE_DATA\analysed lines\4\WD1611_084_l1.dat',w1,f1
  readcol,'C:\Users\Aalis\FUSE_DATA\analysed lines\4\WD1611_084_l2.dat',w2,f2
  readcol,'C:\Users\Aalis\FUSE_DATA\analysed lines\4\WD1611_084_s2.dat',w3,f3
  readcol,'C:\Users\Aalis\FUSE_DATA\analysed lines\4\wd1611_ghrs.dat',w4,f4



  ;C_II
  i=where(w1 ge 1020 and w1 le 1060)
  writekrs, w1(i), f1(i), 'WD1611_084_1036_CII', 'WD1611_084', 'FUSE', 'AliceC', 0,
1036.3367, 'C_II'
  writekrs, w1(i), f1(i), 'WD1611_084_1037_CII#', 'WD1611_084', 'FUSE', 'AliceC', 0,
1037.0182, 'C_II#'
  writekrs, w1(i), f1(i), 'WD1611_084_1048_ArI', 'WD1611_084', 'FUSE', 'AliceC', 0,
1048.2198, 'Ar_I'


  ;O_I
  i=where(w3 ge 950 and w3 le 1000)
  writekrs, w3(i), f3(i), 'WD1611_084_976_OI', 'WD1611_084', 'FUSE', 'AliceC', 0,
976.4481, 'O_I'


  i=where(w1 ge 1010 and w1 le 1050)
  writekrs, w1(i), f1(i), 'WD1611_084_1039_OI', 'WD1611_084', 'FUSE', 'AliceC', 0,
1039.2304, 'O_I'


  i=where(w4 ge 1280 and w4 le 1330)
  writekrs, w4(i), f4(i), 'WD1611_084_1302_OI', 'WD1611_084', 'GHRS', 'AliceC', 0,
1302.1685, 'O_I'


  ;Si II
  i=where(w1 ge 1000 and w1 le 1050)
  writekrs, w1(i), f1(i), 'WD1611_084_1020_SiII', 'WD1611_084', 'FUSE', 'AliceC', 0,
1020.6989, 'Si_II'
  i=where(w4 ge 1280 and w4 le 1350)
  writekrs, w4(i), f4(i), 'WD1611_084_1304_SiII', 'WD1611_084', 'GHRS', 'AliceC', 0,
1304.3702, 'Si_II'


  ;S_II
  i=where(w4 ge 1220 and w4 le 1290)
```

```
  writekrs, w4(i), f4(i), 'WD1611_084_1250_SII', 'WD1611_084', 'GHRS', 'AliceC', 0,
1250.584, 'S_II'

  writekrs, w4(i), f4(i), 'WD1611_084_1253_SII', 'WD1611_084', 'GHRS', 'AliceC', 0,
1253.811, 'S_II'


  ;N_I+Fe_II+P_II

  i=where(w2 ge 1120 and w2 le 1160)

  writekrs, w2(i), f2(i), 'WD1611_084_1134,16_NI', 'WD1611_084', 'FUSE', 'AliceC', 0,
1134.1653, 'N_I'

  writekrs, w2(i), f2(i), 'WD1611_084_1134,41_NI', 'WD1611_084', 'FUSE', 'AliceC', 0,
1134.4149, 'N_I'

  writekrs, w2(i), f2(i), 'WD1611_084_1134,98_NI', 'WD1611_084', 'FUSE', 'AliceC', 0,
1134.9803, 'N_I'

  writekrs, w2(i), f2(i), 'WD1611_084_1144,94_FeII', 'WD1611_084', 'FUSE', 'AliceC', 0,
1134.9803, 'Fe_II'

  writekrs, w2(i), f2(i), 'WD1611_084_1152,82_PII', 'WD1611_084', 'FUSE', 'AliceC', 0,
1152.8180, 'P_II'


end
```

# Annex 1.2

This is an example for the WD1611-084.

```
pro plot_lines_WD1611_084

readcol,'C:\Users\Aalis\FUSE_DATA\analysed lines\4\WD1611_084_l1.dat',w1,f1
readcol,'C:\Users\Aalis\FUSE_DATA\analysed lines\4\WD1611_084_l2.dat',w2,f2
readcol,'C:\Users\Aalis\FUSE_DATA\analysed lines\4\WD1611_084_s2_shifted by -
0,04.dat',w3,f3
readcol,'C:\Users\Aalis\FUSE_DATA\analysed lines\4\wd1611_ghrs.dat',w4,f4



c=3.e5
f1=f1*1e11
f2=f2*1e11
f3=f3*1e11
f4=f4*1e11



set_plot,'ps'
device,filename='WD1611_084_lines_100_landscape.ps',/landscape
!p.multi=[0,2,4,1,1]

; C species

l1=1036.3367 ;C II F1
l3=1037.0182 ;C II* F1
l45=1176.37; C III* F2

l6=1548.203 ;C IV F4
l7=1550.777 ;C IV F4

v1=c*(w1-l1)/l1
v3=c*(w1-l3)/l3
v45=c*(w2-l45)/l45

v6=c*(w4-l6)/l6
v7=c*(w4-l7)/l7
```

```
plot,v1,f1,psym=10,xr=[-100,100],yr=[0,0.2],xtitle='!6 Velocity (km/s)',ytitle='!6
Normalized Flux',xstyle=1,ystyle=1,charsize=1.4,charthick=3, $
  thick=4,xthick=4,ythick=4,title='!6 WD1611_084 - C II 1036.33'
oplot,[-25,-25],[0,4],thick=4,linestyle=2
oplot,[-40,-40],[0,4],thick=4,linestyle=4


plot,v3,f1,psym=10,xr=[-100,100],yr=[0,0.20],xtitle='!6 Velocity (km/s)',ytitle='!6
Normalized Flux',xstyle=1,ystyle=1,charsize=1.4,charthick=3, $
  thick=4,xthick=4,ythick=4,title='!6 WD1611_084 - C II* 1037.02'
oplot,[-25,-25],[0,4],thick=4,linestyle=2
oplot,[-40,-40],[0,4],thick=4,linestyle=4


plot,v45,f2,psym=10,xr=[-100,100],yr=[0,0.2],xtitle='!6 Velocity (km/s)',ytitle='!6
Normalized Flux',xstyle=1,ystyle=1,charsize=1.4,charthick=3, $
  thick=4,xthick=4,ythick=4,title='!6 WD1611_084 - **C III* 1176.37'
oplot,[-25,-25],[0,4],thick=4,linestyle=2
oplot,[-40,-40],[0,4],thick=4,linestyle=4


plot,v6,f4,psym=10,xr=[-100,100],yr=[0,5],xtitle='!6 Velocity (km/s)',ytitle='!6
Normalized Flux',xstyle=1,ystyle=1,charsize=1.4,charthick=3, $
  thick=4,xthick=4,ythick=4,title='!6 WD1611_084 - **C IV 1548.20'
oplot,[-25,-25],[0,5],thick=4,linestyle=2
oplot,[-40,-40],[0,5],thick=4,linestyle=4



plot,v7,f4,psym=10,xr=[-100,100],yr=[0,5],xtitle='!6 Velocity (km/s)',ytitle='!6
Normalized Flux',xstyle=1,ystyle=1,charsize=1.4,charthick=3, $
  thick=4,xthick=4,ythick=4,title='!6 WD1611_084 - **C IV 1550.78'
oplot,[-25,-25],[0,5],thick=4,linestyle=2
oplot,[-40,-40],[0,5],thick=4,linestyle=4


;OI and N species


l9=976.4481 ;O I s2
l10=1039.2304 ;O I F1
l11=1302.1685 ;O I F4
l40=1031.9261; O VI F1
l12=989.799 ;N III F1
l38=991.577; N III* F1


l41=1134.1653 ;N I F2
l42=1134.4149 ;N I F2
l14=1134.9803 ;N I F2
```

```
v9=c*(w3-l9)/l9

v10=c*(w1-l10)/l10

v11=c*(w4-l11)/l11

v12=c*(w1-l12)/l12

v38=c*(w1-l38)/l38

v14=c*(w2-l14)/l14

v40=c*(w1-l40)/l40

v41=c*(w2-l41)/l41

v42=c*(w2-l42)/l42



plot,v9,f3,psym=10,xr=[-100,100],yr=[0,0.4],xtitle='!6 Velocity (km/s)',ytitle='!6
Normalized Flux',xstyle=1,ystyle=1,charsize=1.4,charthick=3, $

  thick=4,xthick=4,ythick=4,title='!6 WD1611_084 - O I 976.45'

oplot,[-25,-25],[0,4],thick=4,linestyle=2

oplot,[-40,-40],[0,4],thick=4,linestyle=4


plot,v10,f1,psym=10,xr=[-100,100],yr=[0,0.4],xtitle='!6 Velocity (km/s)',ytitle='!6
Normalized Flux',xstyle=1,ystyle=1,charsize=1.4,charthick=3, $

  thick=4,xthick=4,ythick=4,title='!6 WD1611_084 - O I 1039.23'

oplot,[-25,-25],[0,4],thick=4,linestyle=2

oplot,[-40,-40],[0,4],thick=4,linestyle=4


plot,v11,f4,psym=10,xr=[-100,100],yr=[0,0.6],xtitle='!6 Velocity (km/s)',ytitle='!6
Normalized Flux',xstyle=1,ystyle=1,charsize=1.4,charthick=3, $

  thick=4,xthick=4,ythick=4,title='!6 WD1611-082 - O I 1302.17'

;;xyouts,40,0.03,'!6O I 1302.17',charsize=1.2

oplot,[-25,-25],[0,4],thick=4,linestyle=2

oplot,[-40,-40],[0,4],thick=4,linestyle=4


plot,v40,f1,psym=10,xr=[-100,100],yr=[0,0.15],xtitle='!6 Velocity (km/s)',ytitle='!6
Normalized Flux',xstyle=1,ystyle=1,charsize=1.4,charthick=3, $

  thick=4,xthick=4,ythick=4,title='!6 WD1611_084 - **O VI 1031.93'

oplot,[-25,-25],[0,4],thick=4,linestyle=2

oplot,[-40,-40],[0,4],thick=4,linestyle=4


plot,v41,f2,psym=10,xr=[-100,100],yr=[0,0.25],xtitle='!6 Velocity (km/s)',ytitle='!6
Normalized Flux',xstyle=1,ystyle=1,charsize=1.4,charthick=3, $

  thick=4,xthick=4,ythick=4,title='!6 WD1611_084 - N I 1134.17'

oplot,[-25,-25],[0,4],thick=4,linestyle=2

oplot,[-40,-40],[0,4],thick=4,linestyle=4


plot,v42,f2,psym=10,xr=[-100,100],yr=[0,0.25],xtitle='!6 Velocity (km/s)',ytitle='!6
Normalized Flux',xstyle=1,ystyle=1,charsize=1.4,charthick=3, $
```

```
  thick=4,xthick=4,ythick=4,title='!6 WD1611_084 - N I 1134.41'
oplot,[-25,-25],[0,4],thick=4,linestyle=2
oplot,[-40,-40],[0,4],thick=4,linestyle=4

plot,v14,f2,psym=10,xr=[-100,100],yr=[0,0.25],xtitle='!6 Velocity (km/s)',ytitle='!6
Normalized Flux',xstyle=1,ystyle=1,charsize=1.4,charthick=3, $
  thick=4,xthick=4,ythick=4,title='!6 WD1611_084 - N I 1134.98'
oplot,[-25,-25],[0,4],thick=4,linestyle=2
oplot,[-40,-40],[0,4],thick=4,linestyle=4

; Si and S species

l39=1020.6989; Si II F1
l20=1304.3702 ;Si II F4

l24=1250.584 ;S II
l25=1253.811 ;S II

v39=c*(w1-l39)/l39
v24=c*(w4-l24)/l24
v25=c*(w4-l25)/l25
v20=c*(w4-l20)/l20



plot,v39,f1,psym=10,xr=[-100,100],yr=[0,0.3],xtitle='!6 Velocity (km/s)',ytitle='!6
Normalized Flux',xstyle=1,ystyle=1,charsize=1.4,charthick=3, $
  thick=4,xthick=4,ythick=4,title='!6 WD1611_084 - Si II 1020.70'
oplot,[-25,-25],[0,4],thick=4,linestyle=2
oplot,[-40,-40],[0,4],thick=4,linestyle=4

plot,v20,f4,psym=10,xr=[-100,100],yr=[0,0.6],xtitle='!6 Velocity (km/s)',ytitle='!6
Normalized Flux',xstyle=1,ystyle=1,charsize=1.4,charthick=3, $
  thick=4,xthick=4,ythick=4,title='!6 WD1611_084 - Si II 1304.37'
oplot,[-25,-25],[0,4],thick=4,linestyle=2
oplot,[-40,-40],[0,4],thick=4,linestyle=4

plot,v24,f4,psym=10,xr=[-100,100],yr=[0,0.4],xtitle='!6 Velocity (km/s)',ytitle='!6
Normalized Flux',xstyle=1,ystyle=1,charsize=1.4,charthick=3, $
  thick=4,xthick=4,ythick=4,title='!6 WD1611_084 - S II 1250.58'
oplot,[-25,-25],[0,4],thick=4,linestyle=2
oplot,[-40,-40],[0,4],thick=4,linestyle=4
```

```
plot,v25,f4,psym=10,xr=[-100,100],yr=[0,0.4],xtitle='!6S Velocity (km/s)',ytitle='!6
Normalized Flux',xstyle=1,ystyle=1,charsize=1.4,charthick=3, $
  thick=4,xthick=4,ythick=4,title='!6 WD1611_084 - S II 1253.81'
oplot,[-25,-25],[0,4],thick=4,linestyle=2
oplot,[-40,-40],[0,4],thick=4,linestyle=4




; Ar, Fe II, P II, Al II

l29=1048.2198 ;Ar I F2
l30=1144.9379 ;Fe II F2

l44=1152.818; P II F2
l32=1670.7874 ;Al II

l46=991.3812; H20 F1
l47=1024.379; H20 F1

l48=966.0976; H21 F3
l49=986.8018; H21 F3
l50=1081.2679; H22 F1




v29=c*(w1-l29)/l29
v30=c*(w2-l30)/l30

v44=c*(w2-l44)/l44

v46=c*(w1-l46)/l46
v47=c*(w1-l47)/l47

v48=c*(w3-l48)/l48
v49=c*(w3-l49)/l49
v50=c*(w1-l50)/l50

plot,v29,f1,psym=10,xr=[-100,100],yr=[0,0.25],xtitle='!6 Velocity (km/s)',ytitle='!6
Normalized Flux',xstyle=1,ystyle=1,charsize=1.4,charthick=3, $
  thick=4,xthick=4,ythick=4,title='!6 WD1611_084 - Ar I 1048.22'
oplot,[-25,-25],[0,4],thick=4,linestyle=2
oplot,[-40,-40],[0,4],thick=4,linestyle=4
```

```
plot,v30,f2,psym=10,xr=[-100,100],yr=[0,0.2],xtitle='!6 Velocity (km/s)',ytitle='!6
Normalized Flux',xstyle=1,ystyle=1,charsize=1.4,charthick=3, $
  thick=4,xthick=4,ythick=4,title='!6 WD1611_084 - Fe II  1144.94'
oplot,[-25,-25],[0,4],thick=4,linestyle=2
oplot,[-40,-40],[0,4],thick=4,linestyle=4


plot,v44,f2,psym=10,xr=[-100,100],yr=[0,0.2],xtitle='!6 Velocity (km/s)',ytitle='!6
Normalized Flux',xstyle=1,ystyle=1,charsize=1.4,charthick=3, $
  thick=4,xthick=4,ythick=4,title='!6 WD1611_084 - P II 1152.82'
oplot,[-25,-25],[0,4],thick=4,linestyle=2
oplot,[-40,-40],[0,4],thick=4,linestyle=4


plot,v47,f1,psym=10,xr=[-100,100],yr=[0,0.07],xtitle='!6 Velocity (km/s)',ytitle='!6
Normalized Flux',xstyle=1,ystyle=1,charsize=1.4,charthick=3, $
  thick=4,xthick=4,ythick=4,title='!6 WD1611_084 - H20 1024.38'
oplot,[-25,-25],[0,4],thick=4,linestyle=2
oplot,[-40,-40],[0,4],thick=4,linestyle=4


plot,v48,f3,psym=10,xr=[-100,100],yr=[0,0.2],xtitle='!6 Velocity (km/s)',ytitle='!6
Normalized Flux',xstyle=1,ystyle=1,charsize=1.4,charthick=3, $
  thick=4,xthick=4,ythick=4,title='!6 WD1611_084 - H21 966.10'
oplot,[-25,-25],[0,4],thick=4,linestyle=2
oplot,[-40,-40],[0,4],thick=4,linestyle=4


plot,v49,f3,psym=10,xr=[-100,100],yr=[0,0.3],xtitle='!6 Velocity (km/s)',ytitle='!6
Normalized Flux',xstyle=1,ystyle=1,charsize=1.4,charthick=3, $
  thick=4,xthick=4,ythick=4,title='!6 WD1611_084 - H21 986.80'
oplot,[-25,-25],[0,4],thick=4,linestyle=2
oplot,[-40,-40],[0,4],thick=4,linestyle=4


plot,v50,f1,psym=10,xr=[-100,100],yr=[0,0.3],xtitle='!6 Velocity (km/s)',ytitle='!6
Normalized Flux',xstyle=1,ystyle=1,charsize=1.4,charthick=3, $
  thick=4,xthick=4,ythick=4,title='!6 WD1611_084 - H22 1081.27'
oplot,[-25,-25],[0,4],thick=4,linestyle=2
oplot,[-40,-40],[0,4],thick=4,linestyle=4


!p.multi=0 ;to reset p.multi


device,/close
set_plot,'win' ; win


end
```

# Bibliography


[1] J. Farihi, *Circumstellar debris and pollution at white dwarf stars*, New Astronomy Reviews 72 (Elsevir), 2016, p. 10-13, p. 31-32.

[2] D. Koester, J. Provencal, and B. T. Gänsicke, *Atmospheric parameters and carbon abundance for hot DB white dwarfs*, Astronomy & Astrophysics 568, 2014, p. 1-2, 5.

[3] GHRSS facts: *https://www.spacetelescope.org/about/general/instruments/ghrs/*

[4] GHRS description: *http://www.ball.com/aerospace/Aerospace/media/Aerospace/Downloads/D0508_Hubble_6_15.pdf?ext=.pdf*

[5] M. Jura and E.D. Young, *Extrasolar Cosmochemistry*, Annu. Rev. Earth Planet Sci., 2014.

[6] M Jura, *Pollution of single white dwarfs by accretion of many small asteroids*, The Astronomical Journal 135, 2008.

[7] B. T. Gänsicke, D. Koester, J. Farihi, J. Girven, S. G. Parsons, and E. Breedt, *The chemical diversity of exo-planetary debris around white dwarfs*, Monthly Notices of the Royal Academy Society 424, 2012.

[8] M. A. Barstow, J. K. Barstow, S. L. Casewell, J. B. Holberg, and I. Hubeny, *Evidence for external origin of heavy elements in hot DA white dwarfs*, Monthly Notices of the Royal Astronomical Society 440, 2014.

[9] N. J. Dickinson, M. A. Barstow, B. Y. Welsh, M. Burleigh, J. Farihi, S. Redfield, and K. Unglaub, *The origin of white dwarf circumstellar features*, Monthly Notices of the Royal Astronomical Society 423, 2012.

[10] N. J. Dickinson, M. A. Barstow, and B. Y. Welsh, *A photospheric metal line profile analysis of hot white dwarfs with circumstellar material*, Monthly Notices of the Royal Astronomical Society 428, 2013.

[11] C. Oliveira, *A study of medium Deuterium in the local interstellar medium - Dissertation*, John Hopkins University, 2004.

[12] C. Oliveira, J. Dupuis, P. Chayer, H. W. Moos, *O/H on the Local Bubble*, The Astrophysical Journal 625, The American Astronomical Society, 2005.

[13] D. J. Wilson, B. T. Gänsicke, D. Koester, J. Holberg, M. R. Burleigh, and C. Belardi, *New Observations of the Mysterious Metal-Polluted White Dwarf GD 394*, 20th European White Dwarf Workshop – ASP Conference Series, vol. 509, 2017.

[14] H. W. Moos, T. B. Ake et al, *Overview of the Far Ultraviolet Spectroscopic Explorer Mission*, The Astrophysical Journal, 538, 2000.

[15] D. Prialnik, *Theory of Steller Structure and Evolution*, Cambridge, 2009 (2nd edition).

[16] G. Fontaine, *The Potential of White Dwarf Cosmochronology, Publications of the Astronomical Society of the Pacific 113 (782), 2001.*

[17] W.W. Morgan and P. C. Keenan, *Spectral Classification,* Annual Review of Astronomy and Astrophysics, vol. 11, 1973

[18] M. Pettini, *Structure and Evolution of Stars – Lectures*, University of Cambridge – Institute of Astronomy, 2014

[19] R. Kippenhahn and A. Weigert, *Stellar Structure and Evolution*, Springer-Verlag, 1994 (3rd edition)

[20] R. Pogge, *Astronomy 162: Introduction to Stars, Galaxies, & the Universe – Lectures*, The Ohio State University – Department of Astronomy, 2006.

[21] J. Dupuis et al., *Adding More Mysteries to the DA White Dwarf GD 394*, The Astrophysical Journal 537, The American Astronomical Society, 2000.

[22] N. Lehner et al., *Far Ultraviolet Spectroscopic Explorer Survey Of The Local Interstellar Medium Within 200 Parsecs*, The Astrophysical Journal 595, The American Astronomical Society, 2003.

[23] D. L. Kaplan, J. Boyles et al, *A 1.05 $M_\odot$ Companion to PSR J2222–0137: the coolest know white dwarf?*, The Astrophysical Journal 789, number 2, 2014.

[24] P. Kowalski, *The Physics of the atmosphere of cool white dwarfs (Doctoral Dissertation)*, Vanderbilt University, 2006.

[25] B. T. Draine, *Physics of the Interstellar and Intergalactic Medium*, Princeton Series in Astrophysics, Princeton University Press, 2011.

[26] W. B. Burton, B. G. Elmegreen, R. Genzel, *The Galactic Interstellar Medium*, Saas-Fee Advanced Course 21, Springer-Verlag, 1992

[27] W. J. Maciel, *Astrophysics of the Interstellar Medium*, Springer, 2013

[28] B. Ryden and R. Pogge, *Interstellar and Intergalactic Medium*, Ohio State Graduate Astrophysics Series, The Ohio State University, 2016

[29] D. A. Gurnett, W. S Kurth,L. F. Burlaga, N. F. Ness, *In Situ Observations of Interstellar Plasma with Voyager 1*, *Science* Vol. 341, Issue 6153, 2013.

[30] *FUSE Mission Overview: http://archive.stsci.edu/fuse/overview.html*

[31] T. Ake, B. G. Anderson et al, *The FUSE Archival Data Handbook*, MAST website: https://archive.stsci.edu/fuse/fuse_ihb_090616_final.pdf, 2009.

[32] A. Riley at al., *Space Telescope Imaging Spectrograph Instrument Handbook for Cycle 25, version 16.0*, Space Telescope Science Institute, 2017.

[33] R. A. Kimble et al., *The on-orbit performance of the Space Telescope Imaging Spectrograph*, The Astrophysical Journal 492, The American Astronomical Society, 1998.

[34] B. E. Woodgate et al., *The Space Telescope Imaging Spectrograph Design*, Publications of the Astronomical Society of the Pacific 110, The Astronomical Society of the Pacific, 1998.

[35] B. Savage and K. Sembach, *The analysis of Apparent Optical Depth Profiles for Interstellar Absorption Lines*, The Astrophysical Journal 379, The American Astronomical Society, 1991.

[36] A. J. Fox B. Savage, B. P. Walker, *Measurement of noisy absorption lines using the apparent optical Depth Technique*, The Astronomical Journal 130, The American Astronomical Society, 2005.

[37] J. B. Holberg, *Hubble Space Telescope Ultraviolet Spectroscopy of Two Hot White Dwarfs*, The Astrophysical Journal 486, The American Astronomical Society, 1997.

[38] J. L. Linsky et al., *What Is The Total Deuterium Abundance In The Local Galactic Disk?*, The Astrophysical Journal 647, The American Astronomical Society, 2006.

[39] D. Koester and G. Chanmugam, *Physics of white dwarf stars*, Reports on Progress in Physics 53, 1990.